



NBS SPECIAL PUBLICATION 400-36

U.S. DEPARTMENT OF COMMERCE / National Bureau of Standards

Semiconductor Measurement Technology

Progress Report
July 1 to September 30, 1976

NATIONAL BUREAU OF STANDARDS

The National Bureau of Standards¹ was established by an act of Congress March 3, 1901. The Bureau's overall goal is to strengthen and advance the Nation's science and technology and facilitate their effective application for public benefit. To this end, the Bureau conducts research and provides: (1) a basis for the Nation's physical measurement system, (2) scientific and technological services for industry and government, (3) a technical basis for equity in trade, and (4) technical services to promote public safety. The Bureau's technical work is performed by the National Measurement Laboratory, the National Engineering Laboratory, and the Institute for Computer Sciences and Technology.

THE NATIONAL MEASUREMENT LABORATORY provides the national system of physical and chemical and materials measurement; coordinates the system with measurement systems of other nations and furnishes essential services leading to accurate and uniform physical and chemical measurement throughout the Nation's scientific community, industry, and commerce; conducts materials research leading to improved methods of measurement, standards, and data on the properties of materials needed by industry, commerce, educational institutions, and Government; provides advisory and research services to other Government Agencies; develops, produces, and distributes Standard Reference Materials; and provides calibration services. The Laboratory consists of the following centers:

Absolute Physical Quantities² — Radiation Research — Thermodynamics and Molecular Science — Analytical Chemistry — Materials Science.

THE NATIONAL ENGINEERING LABORATORY provides technology and technical services to users in the public and private sectors to address national needs and to solve national problems in the public interest; conducts research in engineering and applied science in support of objectives in these efforts; builds and maintains competence in the necessary disciplines required to carry out this research and technical service; develops engineering data and measurement capabilities; provides engineering measurement traceability services; develops test methods and proposes engineering standards and code changes; develops and proposes new engineering practices; and develops and improves mechanisms to transfer results of its research to the ultimate user. The Laboratory consists of the following centers:

Applied Mathematics — Electronics and Electrical Engineering² — Mechanical Engineering and Process Technology² — Building Technology — Fire Research — Consumer Product Technology — Field Methods.

THE INSTITUTE FOR COMPUTER SCIENCES AND TECHNOLOGY conducts research and provides scientific and technical services to aid Federal Agencies in the selection, acquisition, application, and use of computer technology to improve effectiveness and economy in Government operations in accordance with Public Law 89-306 (40 U.S.C. 759), relevant Executive Orders, and other directives; carries out this mission by managing the Federal Information Processing Standards Program, developing Federal ADP standards guidelines, and managing Federal participation in ADP voluntary standardization activities; provides scientific and technological advisory services and assistance to Federal Agencies; and provides the technical foundation for computer-related policies of the Federal Government. The Institute consists of the following divisions:

Systems and Software — Computer Systems Engineering — Information Technology.

¹Headquarters and Laboratories at Gaithersburg, Maryland, unless otherwise noted; mailing address Washington, D.C. 20234.

²Some divisions within the center are located at Boulder, Colorado, 80303.

JUL 19 1978

Semiconductor Measurement Technology

Progress Report, July 1 to September 30, 1976

W. Murray Bullis and J. Franklin Mayo-Wells, Editors

Electron Devices Division
Center for Electronics and Electrical Engineering
National Engineering Laboratory
National Bureau of Standards
Washington, D.C. 20234

Jointly supported by:

The National Bureau of Standards
The Navy Strategic Systems Projects Office
The Defense Nuclear Agency
The Defense Advanced Research Projects Agency
The Space and Missile Systems Organization, and
The Energy Research and Development Administration



U.S. DEPARTMENT OF COMMERCE, Juanita M. Kreps, Secretary

Dr. Sidney Harman, Under Secretary

Jordan J. Baruch, Assistant Secretary for Science and Technology

NATIONAL BUREAU OF STANDARDS, Ernest Ambler, Director

Issued July 1978

National Bureau of Standards Special Publication 400-36

Nat. Bur. Stand. (U.S.), Spec. Publ. 400-36, 78 pages (July 1978)

CODEN: XNBSAV

U.S. GOVERNMENT PRINTING OFFICE
WASHINGTON: 1978

For sale by the Superintendent of Documents, U.S. Government Printing Office, Washington, D.C. 20402

Stock No. 003-003-01955-1 Price \$2.75

(Add 25 percent additional for other than U.S. mailing).

TABLE OF CONTENTS

SEMICONDUCTOR MEASUREMENT TECHNOLOGY

	PAGE
List of Figures	iv
List of Tables	v
Preface	vi
Abstract and Key Words	1
1. Introduction	1
2. Highlights	2
3. Materials Characterization by Electrical Methods	7
3.1. Four-Probe Method	7
3.2. Spreading Resistance Methods	7
3.3. Capacitance-Voltage Methods	18
3.4. Hole Mobility in <i>p</i> -Type Silicon	18
3.5. Indium-Doped Silicon	19
3.6. Thermally Stimulated Current and Capacitance	20
3.7. Extended-Range MIS C(V) Method	24
4. Materials Characterization by Physical Analysis Methods	26
4.1. Calibration Standards for Ion Microprobe Mass Analysis	26
4.2. Electron Spectroscopy Techniques	30
4.3. Techniques for Chemical Diagnostics in Semiconductor Processing	33
4.4. Nuclear-Track Technique	36
4.5. Optical Test for Surface Quality of Sapphire Substrates	37
5. Materials and Procedures for Wafer Processing	40
5.1. Ion Implantation Parameters	40
6. Photolithography	42
6.1. Optical Imaging for Photomask Metrology	42
7. Test Patterns	45
7.1. Cross-Bridge Sheet Resistor	45
7.2. Advanced Planar Silicon Test Structures	46
7.3. Test Pattern Design and Analysis for SOS/LSI	48
8. Assembly and Packaging	49
8.1. Correlation of Moisture Infusion, Leak Size, and Device Reliability	49
8.2. Loose-Particle Detection	52
9. Device Inspection and Test	54
9.1. Scanning Acoustic Microscopy	54
9.2. Thermal Properties of Transistors	57
9.3. Integrated Circuit Die-Attachment Evaluation	59
10. References	60
Appendix A Semiconductor Technology Program Staff	64
Appendix B Semiconductor Technology Program Publications	65
Appendix C Solid-State Technology & Fabrication Services	70
Index	71

LIST OF FIGURES

	PAGE
1. Typical calibration relations between measured spreading resistance and resistivity of silicon for selected cases	9
2. Spreading resistance, R_{sp} , measured as a function of probe spacing, s , for three boron-diffused wafers with different sheet resistances	10
3. Profiles constructed by superposition of multiple uniform layers	12
4. Conductivity profiles for selected diffused layers	15
5. Comparison of traces from high-speed dragging-stylus and conventional stepping-type spreading resistance measurements in two orthogonal directions on an n -type silicon slice with an average resistivity of $2.5 \Omega \cdot \text{cm}$ and a (111) surface orientation	16
6. Preliminary results of hole mobility calculations in boron-doped silicon at 300 K	19
7. Thermally stimulated current and capacitance response of the gold donor in p -type silicon at various heating rates	20
8. Scaled Arrhenius plot of hole emission probability, e^p/T^2 , as a function of inverse temperature for the gold donor in p -type silicon	22
9. Typical thyristor structure	24
10. Cross section of mesa diode test structure	24
11. Composition profiles of metal-silicon dioxide interfaces by Auger-sputter techniques	31
12. Broadening of a step interface resulting from the effects of electron escape depth	32
13. Interface state density, N_{ss} , as a function of carbon concentration at the interface	35
14. Resistivity of p -type silicon as a function of boron density as determined by the nuclear-track technique	37
15. Correlations between optical and x-ray determinations of the quality of a sapphire surface and the corresponding deposited silicon film	38
16. Illustration of implanted random-equivalent and channeled depth distributions and comparisons with ideal amorphous and perfectly channelled distributions, respectively	41
17. Fraction of implanted ions outside ideal distributions as a function of the critical angle for channeling, ψ'_c	41
18. Calculated image profiles of a 10- μm wide clear line for an optical microscope with a constant 2λ of spherical aberration and defocus varying in steps of $\lambda/4$ from 0 to -2λ , 0.22 NA condenser and 0.65 NA objective, illumination wavelength of 560 nm, and a 0.13- μm wide scanning slit	43
19. Experimental image profiles of one edge of a nominally 10- μm wide clear line for an optical microscope with white light and filtered light at 560 nm, 0.60 NA condenser and 0.90 NA objective, and 0.13- μm wide scanning slit	43
20. Comparison of theoretical and experimental image profiles of clear lines for an optical microscope with 0.60 NA condenser and 0.90 NA objective, illumination wavelength of 560 nm, and 0.13- μm wide scanning slit	43
21. Schematic diagram of the cross-bridge sheet resistor	45
22. Cross-sectional view of a diffused region showing various dimensions	46
23. A simple equivalent circuit model for the bridge sheet resistor	46
24. Normalized width error, E , anticipated from measurements on a bridge test structure	46

LIST OF FIGURES

	PAGE
25. Schematic diagrams of advanced test structures	47
26. Hybrid test packages for use in the moisture infusion study	50
27. Typical calibration data for oxide moisture sensor	50
28. Typical dew-point sensor response curve of leakage current as a function of substrate temperature	51
29. Average response of three driven acoustic emission transducers A, B, and C attached to driving acoustic emission transducer by couplant K, L, or M, as a function of driving frequency	52
30. Response of three acoustic emission transducers A, B, and C attached to driving acoustic emission transducer by couplant K, L, or M and driven at 150 kHz, as a function of number of removal and remounting cycles	53
31. Scanning acoustic and optical photomicrographs of a portion of a C-MOS-on-sapphire integrated circuit	54
32. Variations in intensity of reflected pulsed acoustic signal as the lens-to-specimen spacing is changed	56
33. Scanning acoustic micrographs of a 300-nm thick gold film grid pattern on silicon at various lens-to-specimen distances	56
34. Effect of sub-surface void on intensity of acoustic signal reflected from an aluminum film on silicon dioxide	57
35. A schematic representation of the thermal instability and second breakdown limits of safe power transistor operation in the forward-biased region	58
36. Curves of emitter-base voltage and its time derivative as a function of time following removal of power	58
37. Simplified schematic of circuit for measuring time derivative of emitter-base voltage	59

LIST OF TABLES

	PAGE
1. Sheet Resistance of Three Boron-Diffused Wafers	11
2. Characteristics of Diffused Layered Structures Used for Spreading Resistance Measurements	14
3. Performance Characteristics of New Thermally Controlled Chuck	22
4. Capacitance Measurements on SOS Specimens Obtained with Guarded and Unguarded Electrodes	25
5. Normalized Sputtering Rate of an Ion Microprobe Mass Analyzer Operated with a 19.4-keV O ₂ ⁺ Beam and a Nominal Raster Size of 125 μm by 100 μm	28
6. Calibration Data for Ion Microprobe Mass Analysis of Phosphorus-Doped Silicon Based on Integral Ratio Method	29
7. Preliminary Results of Auger-Sputter Profiling Measurements on CVD and Dry Thermal Oxides	33
8. Oxide Sensor and Dew-Point Determination of Moisture Content of Sealed-Off Test Packages	51
9. Response of Test Transducers at 150 kHz Obtained Using Viscous Liquid Couplant M	53

P R E F A C E

The Semiconductor Technology Program serves to focus NBS research to enhance the performance, interchangeability, and reliability of discrete semiconductor devices and integrated circuits through improvements in measurement technology for use in specifying materials and devices in national and international commerce and for use by industry in controlling device fabrication processes. This research leads to carefully evaluated and well-documented test procedures and associated technology. Special emphasis is placed on the dissemination of the results of the research to the electronics community. Application of these results by industry will contribute to higher yields, lower cost, and higher reliability of semiconductor devices. Improved measurement technology also leads to greater economy in government procurement by providing a common basis for the purchase specifications of government agencies, and, in addition, provides a basis for controlled improvements in fabrication processes and in essential device characteristics.

The Program receives direct financial support principally from two major sponsors: the Defense Advanced Research Projects Agency (ARPA)* and the National Bureau of Standards (NBS).† In addition, the Program receives support from the Defense Nuclear Agency (DNA),‡ the Air Force Space and Missiles Systems Organization,¶ the Navy Strategic Systems Project Office,§ and the Energy Research and Development Administration.¶ The ARPA-supported portion of the Program, Advancement of Reliability, Processing, and Automation for Integrated Circuits with the National Bureau of Standards (ARPA/IC/NBS), addresses critical Defense Department problems in the yield, reliability, and availability of digital monolithic integrated circuits. Other portions of the Program emphasize aspects of the work which relate to the specific needs of the supporting agency. Measurement-oriented activity appropriate to the mission of NBS is an essential aspect in all parts of the Program.

Essential assistance to the Program is also received from the semiconductor industry through cooperative experiments and technical exchanges. NBS interacts with industrial users and suppliers of semiconductor devices through participation in standardizing organizations; through direct consultations with device and material suppliers, government agencies, and other users; and through periodical-

ly scheduled symposia and workshops. In addition, progress reports, such as this one, are regularly prepared for issuance in the NBS Special Publication 400- sub-series. More detailed reports such as state-of-the-art reviews, literature compilations, and summaries of technical efforts conducted within the Program are issued as these activities are completed. Reports of this type which are published by NBS also appear in the Special Publication 400- sub-series.

Another means of interaction with the electronics community is by direct contact. In particular, comments from readers regarding the usefulness of the results reported herein or relating to directions of future activity in the Program are always welcome.

Disclaimer

Certain commercially available materials or instruments are identified in this publication for the purpose of providing a complete description of the work performed. The experiments reported do not constitute a complete evaluation of the performance characteristics of the products so identified. In no case does such identification imply recommendation or endorsement by the National Bureau of Standards nor does it imply that the items identified are necessarily the best available for the purpose.

* Through ARPA Order 2397, Program Code TD10 (NBS Cost Center 4257555). Unless otherwise noted, work was funded from this source.

† Principally through the Electronic Technology Program (Cost Center 4257100). Additional funding through the Dimensional Metrology Program (Cost Center 2131119) and the Nondestructive Evaluation Program (Cost Center 4253130).

§ Through Inter-Agency Cost Reimbursement Order 7T-812 (NBS Cost Center 4259522).

¶ Through MIPR FY76 167600366 (NBS Cost Center 4259560).

Code SP-23, through project order N00164-76-MP-04511 administered by Naval Weapons Support Center, Crane, Indiana (NBS Cost Center 4251533).

¶ Through ERDA Contract No. E(49-1)-3800, Modification 3 (NBS Cost Center 4259561).

SEMICONDUCTOR MEASUREMENT TECHNOLOGY

PROGRESS REPORT July 1 to September 30, 1976

Abstract: This progress report describes NBS activities directed toward the development of methods of measurement for semiconductor materials, process control, and devices. Both in-house and contract efforts are included. The emphasis is on silicon device technologies. Principal accomplishments during this reporting period included (1) completion of the systematic study of the effects of surface preparation and probe material on the empirical calibration between specimen resistivity and spreading resistance of *n*- and *p*-type silicon; (2) initial evaluation of the nuclear-track technique for quantitative determination of trace amounts of boron in silicon; (3) development of procedures for using an optical research microscope to make accurate measurements of the width of a clear line as narrow as 0.5 μm in a completely or nearly opaque background; (4) design of a compact cross-bridge test structure for electrical measurement of line width and sheet resistance in minimum line-width geometries; (5) completion of the initial phase of the study of the particle-impact noise detection test for screening devices for the presence of loose particles in the package; (6) demonstration of a greater-than-expected line resolution capability for the scanning acoustic microscope; and (7) development of a non-destructive technique to measure the onset of second breakdown in forward-biased, medium-power transistors. Also reported is other ongoing work on materials characterization by electrical and physical analysis methods, materials and procedures for wafer processing, photolithography, test patterns, and device inspection and test procedures. Supplementary data concerning staff, publications, and technical services are included as appendices.

Key Words: Auger electron spectroscopy; capacitance-voltage methods; dew-point sensing; dragging-stylus probe; electrical properties; electronics; four-probe method; hermeticity; hole mobility; infrared reflectance; ion implantation; ion microprobe mass analysis; line-width measurements; nuclear-track technique; particle-impact noise detection; photolithography; photovoltaic method; *p-n* junction; power-device grade silicon; resistivity; resistivity variations; resistors, sheet; safe operating area, transistor; scanning acoustic microscope; second breakdown; semiconductor materials; semiconductor process control; silicon; silicon dioxide; silicon-on-sapphire; spreading resistance; test patterns; test structures; thermally stimulated current and capacitance; thermal properties, transistor; thermal response; thyristors; transistors, power; ultraviolet reflectance; x-ray photoelectron spectroscopy.

1. INTRODUCTION

This is a report to the sponsors of the Semiconductor Technology Program on work carried out during the thirty-third quarter of the Program. The report summarizes research on a wide variety of measurement methods for semiconductor materials, process control, and devices that are being studied at the National Bureau of Standards. The Program, which emphasizes silicon-based device technologies, is a continuing one, and the results and conclusions reported here are subject to modification and refinement.

The work of the Program is divided into a number of tasks, each directed toward the study of a particular material or device property or measurement technique. This report is subdivided according to these tasks. Highlights of activity during the reporting period are given in section 2. This section provides a management-level overview of the entire effort. Subsequent sections deal with each specific task area. References cited are listed in the final section of the report.

The report of each task includes a narrative description of progress made during this reporting period. Additional information concerning the material reported may be obtained directly from individual staff mem-

bers identified with the task in the report. Organizational locations and telephone numbers for Program staff members are given in Appendix A.

Background material on the Program and individual tasks may be found in earlier progress reports as listed in Appendix B. From time to time, publications are prepared that describe some aspect of the program in greater detail. Current publications of this type are also listed in Appendix B. Reprints or copies of such publications are usually available from the author on request. In addition, tutorial videotapes are being prepared on selected measurement topics for dissemination to the electronics community. Currently available videotapes and procedures for obtaining them on loan are also listed in Appendix B.

Technical services in areas of competence are provided to other NBS activities and other government agencies as they are requested. Usually these are short-term, specialized services that cannot be obtained through normal commercial channels. To indicate the kinds of technology available to the Program, such services provided during the current reporting period are listed in Appendix C.

2. HIGHLIGHTS

Highlights of progress in the various technical task areas of the Program are listed in this section. Particularly significant accomplishments during this reporting period included:

(1) completion of the systematic study of the effects of surface preparation and probe material on the empirical calibration between specimen resistivity and spreading resistance of *n*- and *p*-type silicon;

(2) initial evaluation of the nuclear-track technique for quantitative determination of trace amounts of boron in silicon;

(3) development of procedures for using an optical research microscope to make accurate measurements of the width of a clear line in a completely or nearly opaque background or of an opaque line in a clear background down to 0.5 μm ;

(4) design of a compact cross-bridge test structure for electrical measurement of line width and sheet resistance in minimum line-width geometries;

(5) completion of the initial phase of the study of the particle-impact noise detection test for screening devices for the presence of loose particles in the package;

(6) demonstration of a greater-than-expected line resolution capability for the scanning acoustic microscope; and

(7) development of a nondestructive technique to measure the onset of second breakdown in forward-biased, medium-power transistors.

New tasks were undertaken to investigate techniques for characterizing extrinsic silicon for use in infrared detector arrays, to evaluate the application of x-ray photoelectron spectroscopy to diagnostic measurements in semiconductor device processing, and to develop test structures with integral signal-processing circuitry to allow high-speed measurement of small currents. The work on the high-speed, dragging-stylus spreading resistance instrument and instrumentation for measurement of capacitance and conductance at applied voltages of up to 25 kV was completed. Work on development of techniques for measuring trace impurities in process chemicals (such as diffusion sources and carrier gases) was terminated because available measurement techniques proved to be too insensitive for conclusive experiments.

Unless another organization is identified, the work described in the following paragraphs was performed at the National Bureau of Standards.

Materials Characterization by Electrical Methods — Work continued on the study of correction factors for four-probe resistivity measurements on slices of small diameter and intermediate thickness. The results of measurements on a 5/8-in. (15.9-mm) diameter, 10- $\Omega\cdot\text{cm}$, *p*-type silicon slice suggest that conditions may exist for which it is not valid to use as an overall geometric correction factor the product of the individual thickness and diameter factors, as is assumed in the standard four-probe method.

The first phase was completed of the study of the effects of specimen surface preparation and probe material on the empirical calibration between specimen resistivity and spreading resistance. The calibration relation was found to depend on both surface preparation and probe type for *n*-type silicon; no probe dependence was found for *p*-type silicon. Nearly linear relationships between spreading resistance and resistivity could be obtained on *p*-type silicon with (111) surface orientation and, for certain probe materials, on *n*-type silicon with (100) surface orientation. For no combination of surface preparation and probe materials studied could a linear relationship be obtained for *n*-type silicon with (111) surface orientation.

Preliminary evaluations of simplified correction-factor algorithms for rapid calculation of resistivity or dopant density profiles from spreading resistance measurements on beveled sections of semiconductor structures have been completed at Solecon Laboratories. Algorithms based on the local slope of the measured spreading resistance profile were found to give satisfactory results under certain conditions.

In work at RCA Laboratories, conditions were found which permit reasonable probe life in the high-speed, dragging-stylus apparatus for measuring spreading resistance. Results of measurements along the diameter of a heavily striated silicon slice demonstrated that resolution comparable with that of a conventional stepping-type instrument could be obtained with the high-speed instrument in 1/20th of the time.

HIGHLIGHTS

A new method was developed to extract background dopant densities in the range from 10^{16} cm^{-3} to about 10^{18} cm^{-3} from junction capacitance-voltage data. This method is intended for use in cases in which the junction is prepared by diffusion into a uniformly doped substrate. In the method, it is assumed that the diffused layer profile in the region of the junction is approximately Gaussian. In addition, work is continuing on the examination of the range of validity of the Schottky equations, which are commonly used to extract dopant density from capacitance-voltage data.

The methods for developing theoretical expressions for carrier mobility in silicon as a function of temperature and dopant density are being extended to cover the case of hole mobility in *p*-type silicon. In this case, there is an additional complication because of the complexity of the valence band structure. Initial work is being concentrated on boron-doped silicon; silicon doped with other acceptor impurities will have slightly different mobility-versus-dopant density characteristics because of differences in fractional ionization occurring in the dopant density range from 10^{16} to 10^{19} cm^{-3} even at room temperature.

A new task was initiated to study methods for characterizing extrinsic silicon for use in infrared imaging arrays. Initial efforts are being concentrated on evaluation of various techniques to detect extraneous levels in indium-doped silicon; particular emphasis is being placed on study of the so-called X-level, which appears to be an acceptor state located between the indium level and the valence band. The presence of this level at concentrations considerably lower than the indium concentration reduces the performance of indium-doped infrared detectors and makes it necessary to operate them at lower temperatures to obtain the best signal-to-noise ratio.

Measurements of thermally stimulated current and capacitance were made on a gold-doped *p*-type silicon MOS capacitor. As expected from theoretical considerations, the phase I thermally stimulated current and capacitance responses of the gold donor center in this structure were the same as responses of the center in an n^+p junction diode. In addition, measurement procedures were established to characterize defect centers by analyzing their transient capacitance response under isothermal conditions.

Progress was made toward all three of the objectives of the task to evaluate the use of thermally stimulated current and capacitance measurements as a means for characterizing defects in power device-grade silicon wafers. An improved thermally controlled chuck and automatic wafer prober was assembled and tested; the characteristics of this apparatus meet or exceed all design targets. A processing sequence, in which all temperatures are 400°C or less, was selected for fabricating MOS capacitors for making thermally stimulated current and capacitance measurements. Initial steps were taken toward defining procedures for fabricating test structures which provide access to both sides of the *p-n* junction in a partially or completely fabricated thyristor structure.

Development and initial evaluation of the 25-kV system for capacitance and conductance measurements as a function of voltage was completed at RCA Laboratories. This system permits application of the extended-range capacitance-voltage technique to metal-insulator-semiconductor structures with insulator thickness in excess of $150 \mu\text{m}$.

The automated data collection and analysis system for making photovoltaic measurements to determine resistivity variations along the diameter of circular slices was assembled and is being tested. This system is intended to be used to measure slices suitable for fabrication of high-power thyristors and rectifier diodes. The system allows a user to measure the resistivity profile along a slice diameter in about 2 min with some user-system interaction after the measurement run has begun. Although measurement of the average resistivity by the van der Pauw technique has not yet been automated, this measurement can routinely be made using the same probes as in the automated system to make contact to the slice.

Materials Characterization by Physical Analysis Methods — Development of calibration standards for ion microprobe mass analysis continued at Texas Instruments with the completion of the analysis of the silicon specimens implanted with phosphorus. The relative sample standard deviation of the calibration coefficient (ratio of average phosphorus density to instrument signal) for 18 profile measurements made on four slices over a period of several months was 25 percent; this is a measure of the long-term reproducibility of ion microprobe mass analysis to be expected when measuring phosphorus in silicon.

HIGHLIGHTS

The study of the effects of various experimental conditions on Auger-sputter profiling of oxide-silicon structures continued at Stanford University. In order to avoid effects of beam asymmetry, procedures were developed for aligning the ion beam employed to sputter etch the crater produced in carrying out depth-profiling measurements with Auger electron spectroscopy. Measurements of ion stimulated Auger emission were completed to the point of defining the possible interferences which this process might produce in profiling work; it was found that negligible interference from this mechanism occurs at a primary ion energy of 1 keV, which has been found on other grounds to produce the best depth resolution in the silicon dioxide-silicon system. Initial work in the study of limitations on the resolution of interface width in Auger-sputter profiling were concentrated on the effects of finite electron escape depth; an extension to include the effects of ion knock-on mixing is also under development. Preliminary Auger electron spectroscopy measurements were made on interfaces between pure and doped aluminum metal films sputtered onto thermally grown silicon dioxide. Work has also been undertaken to study the relationships between the microscopic properties (such as width and stoichiometry) of silicon-silicon dioxide interfaces, the electrical characteristics of the interfaces, and the methods of preparing the oxide films. Preliminary results indicate that the interfaces between silicon and oxides prepared by chemical vapor deposition are 2 to 2.5 nm wider than interfaces between silicon and "good" thermal oxides.

A new task was undertaken at the Jet Propulsion Laboratories to evaluate the application of x-ray photoelectron spectroscopy to diagnostic measurements in semiconductor device processing and to establish and document appropriate methods for specimen preparation and data collection, analysis, and interpretation. Instrumental modifications were made to improve the ability to determine binding energies referenced to a known potential for species being examined; spectral shifts which resulted from specimen surface charging and which could be misinterpreted as chemical shift variations had been observed. The effects of residual carbon on interface-state density were investigated; it was tentatively concluded that different chemical forms of carbon at the silicon interface show different retention ratios after oxidation and that both the final amount and chemical state of carbon at the interface significantly affect the interface state density. A significant effort has been devoted to exami-

nation of data-reduction algorithms. A number of algorithms have been developed which give varying degrees of recovery of original information in the presence of asymmetric Gaussian instrument functions. Similar algorithms have been developed to treat the problem of recovering signal from noise.

Boron cannot be detected by conventional neutron activation analysis, and most chemical techniques are not sufficiently sensitive to detect trace concentrations. Therefore, alternative techniques are necessary. Work was begun to evaluate the applicability of the nuclear-track technique to the determination of trace amounts of boron in silicon slices. Preliminary results suggest that a boron density of about 10^{15} cm^{-3} is the lower limit for routine measurements by the technique; good agreement with various electrical techniques was obtained in a variety of cases.

Work on a rapid, nondestructive reflectance method for determination of surface quality of sapphire substrates and the characteristics of silicon films epitaxially grown on sapphire continued at RCA Laboratories. Good correlation was obtained between the surface quality of the substrate as determined by infrared reflectance, the quality of the epitaxial film as determined by ultraviolet reflectance, and crystalline quality of the film as determined by x-ray diffractometry. The reflectance method has the potential of providing a quantitative measure of substrate surface quality which could be used to monitor the amount of polishing of substrates. Reduction of the amount of polishing required, with consequent substantial cost savings, could result.

Materials and Procedures for Wafer Processing
— Development of measurement technology for critical ion implantation parameters continued at Hughes Research Laboratories. A study was made of the effects of variations in the angle between ion beam and crystallographic axes of the wafer being implanted on both random-equivalent and channeled-implantation depth distributions in silicon. It was found that in implantation of low-velocity ions (ions with high atomic number, or low energy, or both), a significant channeling tail can exist when the implantation is conducted at the commonly employed randomization angle. On the other hand, accurately channeled distributions can only be achieved with a high degree of angular control when high velocity ions are being implanted; much less control is required if low velocity ions are being implanted.

HIGHLIGHTS

Photolithography — Additional investigations were completed of the effects of the operating conditions of an optical microscope on line-width measurements in transmitted illumination. In particular, the effects of a finite transmittance of the opaque background and of spherical aberration and defocus were studied. The optical and mechanical performance characteristics of equipment required for accurate measurement of the width of photomask lines as narrow as 0.5 μm have been defined. The NBS optical microscope system can presently measure line widths to within an uncertainty of $\pm 0.2 \mu\text{m}$; if the scan is repeated at the same position on the line, the uncertainty is less than $\pm 0.05 \mu\text{m}$. It appears that the edge quality of the line may be the limiting factor in the accuracy and repeatability of the measurement of the width of lines narrower than 10 μm .

Test Patterns — A new test structure which incorporates both a cross-type van der Pauw sheet resistor and a conventional bridge-type sheet resistor into a single unit was designed. Both the width of the bridge structure and the sheet resistance can be obtained from electrical measurements on this test structure, which requires only six contact pads. The results of a preliminary analysis suggest that the structure is suitable for making measurements on the widths of the smallest lines occurring in the pattern.

A new task was undertaken at the Westinghouse Defense and Electronics Systems Center to determine the operational limitations and potential applications of integral electrometer amplifiers in specialized circuits used for the measurement of small currents in times compatible with use in high-speed automatic testers.

Additional measurements have been made to study the characteristics of individual structures in the SOS/LSI test pattern being developed at RCA Laboratories. One result of general interest is that the cross-type van der Pauw sheet resistor test structure, which is present in a number of devices in this pattern, was shown experimentally to be appropriately treated as a simple van der Pauw resistor.

Assembly and Packaging — Additional studies were carried out in efforts to calibrate the dew-point moisture sensors being used in the investigation of the correlations between moisture infusion, leak size, and device reliability at Martin Marietta Aerospace. Although consistent results were not obtained,

adequate calibration may be possible by use of appropriate test conditions.

Additional studies were completed on selected aspects of the particle-impact noise detection test for screening devices for the presence of loose particles in the package. Principal emphasis was placed on the determination of the effectiveness of various couplants for transmitting the high-frequency vibrations generated by the impact of a particle against the package wall. At this stage of the investigation it appears that, of the three couplants recommended in the test procedure being proposed for inclusion in MIL-STD-883, the liquid couplant is most effective in transmitting acoustic emission signals and provides most repeatable results.

Device Inspection and Test — Investigations at Stanford University and Hughes Research Laboratories of the scanning acoustic microscope for examining semiconductor devices and integrated circuits were directed primarily toward examination of a variety of test specimens in order to establish an improved understanding of the information which can be obtained with this instrument. The microscope was found to be as easy to operate as an optical microscope; its simple controls and lack of a vacuum system render it more convenient to operate and maintain than a scanning electron microscope. Moreover, it is superior to the scanning electron microscope for the non-destructive examination of insulating surfaces because charge does not accumulate and degrade the image. Edges and material differences can be displayed with greater clarity than with either optical or scanning electron microscopes. Various levels in an integrated-circuit structure can be displayed in a series of micrographs readily by making small changes in the lens-to-specimen spacing. The microscope has a resolution capability greater than expected, about 1/3 of a wavelength at 10-percent contrast. The microscope has also been successfully utilized to view gallium arsenide field-effect and transferred-electron devices, aluminum fuse links, and clad and unclad optical fibers.

The predictions of a physical model which was proposed to explain the relationship between thermal instability and second breakdown in forward-biased medium-power transistors were confirmed experimentally. A method for non-destructive determination of safe-operating-area limits based on the exclusion of current constrictions and hot spots was developed. This method is also suitable as a nondestructive test for second breakdown under condi-

HIGHLIGHTS

tions in which the limits of thermal instability and second breakdown nearly coincide.

Work has resumed on the investigation of methods for using the temperature response of a substrate diode for determining the integrity of the die attachment of integrated cir-

cuits. Initial measurements on devices bonded to headers with intentionally introduced voids indicate that dc methods are not sufficiently sensitive. Pulse-heating and time-delay measurement methods are expected to provide the required sensitivity.

3. MATERIALS CHARACTERIZATION BY ELECTRICAL METHODS

3.1. Four-Probe Method

Work continued on the study of correction factors for four-probe resistivity measurements on slices of small diameter and intermediate thickness (NBS Spec. Publ. 400-25, pp. 7-8). The results of measurements on a 5/8-in. (15.9-mm) diameter, 10- $\Omega\cdot\text{cm}$, *p*-type silicon slice suggest that conditions may exist where it is not valid simply to combine the thickness and diameter correction factors multiplicatively as is assumed in the standard four-probe method [1].

For slices of finite thickness but infinite lateral extent, the resistivity is given by*

$$\rho = \frac{2\pi s}{G_7(w/s)} F_{sp} F_T \frac{V}{I}, \quad (1)$$

where V is the potential difference between the inner pair of probes, I is the current through the outer pair of probes, s is the average probe spacing, w is the thickness of the slice, $F_{sp} = 1 + 1.25[1 - (s_2/s)]$, s_2 is the spacing between the inner pair of probes, $F_T = 1 - C_T(T - 23)$, C_T is the temperature coefficient of resistivity [1,2], T is the temperature, in degrees Celsius, of the slice at the time of measurement, and $G_7(w/s)$ is a correction factor [3] (NBS Spec. Publ. 400-25, table 1).

For infinitesimally thin slices of finite diameter, the resistivity as measured at the center of the slice is given by

$$\rho = w F_2 F_{sp} F_T \frac{V}{I}, \quad (2)$$

where F_2 is a correction factor for diameter [1,4] and, now, $F_{sp} = 1 + 1.082[1 - (s_2/s)]$.

If Smits' correction factor $F(w/s)$ [5], is used to correct eq (2) for finite thickness [1], one obtains†

$$\rho = w F_2 F(w/s) F_{sp} F_T \frac{V}{I}. \quad (3)$$

Since $F(w/s) = 2 \ln 2 s/[w G_7(w/s)]$, the resistivity which is calculated from eq (1) is $\pi/(F_2 \cdot \ln 2)$ times that calculated from eq (3), provided that the difference in probe spacing correction factors, F_{sp} , is ignored.

For $w \gg s$, the value of $G_7(w/s)$ approaches 1, so that the resistivity calculated by eq (1), which is applicable for large diameter slices, should be independent of thickness; for $w/s > 8$, $G_7(w/s)$ differs from unity by less than 0.2 percent. At the other extreme, where $w \ll s$, the resistivity calculated by eq (3) should be independent of thickness. If the voltage-current ratio is measured on a uniform slice as a function of slice thickness, the resistivity calculated from either eq (1) or eq (3) should approach constant values at both large and small values of w/s ; these values should differ by $|1 - [\pi/(F_2 \cdot \ln 2)]|$ which ranges from 1.4 percent for slice diameter $D = 25s$ to 8 percent for $D = 10s$. Measurements on 1-in. (25-mm) diameter slices (NBS Spec. Publ. 400-25, fig. 1) followed this expected behavior. However, the more recent measurements on 5/8-in. (15.9-mm) diameter slices failed to approach a constant value for w/s as small as 0.24.

This result could arise from the presence of longitudinal resistivity variations in the crystal or from failure of the multiplicative approximation for combining the thickness and diameter correction factors in eq (3).

(J. R. Ehrstein and D. R. Ricks)

3.2. Spreading Resistance Methods

Surface Preparation Effects — The first phase was completed of the study of the effects of specimen surface preparation and probe material on the empirical calibration between specimen resistivity and spreading resistance. The principal intent of this phase of the study (NBS Spec. Publs. 400-25, pp. 8-12, and 400-29, pp. 9-11) was to determine the extent to which surface preparation and probe material affect the reproducibility and linearity of the calibration for se-

* This equation is the one which was actually used to calculate the solid data points in figure 1 of NBS Spec. Publ. 400-25; the factor $G_7(w/s)$ was erroneously omitted in the original discussion of that figure.

† This equation is identical with eq (2d) of NBS Spec. Publ. 400-25 which was used to obtain the open data points of figure 1 of that report. In eq (2d), F_2 is designated as C .

lected low-index planes of both *n*- and *p*-type silicon. Without reproducibility, a calibration curve has little meaning; if the calibration relation is nonlinear, the number of data points required to define the calibration curve is increased.

The present data were taken at probe loads of 440 mN (1 gf = 9.8 mN), which is higher than is generally used for depth profiling applications; such loads are typical of radial profiling applications. These data also provide an important background for work at lighter loads for which experience indicates a pronounced increase in measurement scatter will be seen.

For each surface preparation used, measurements were taken with five sets of probes made from four different alloys. While it is difficult to assure that the correct amount of material was removed for each preparation cycle so that the surface treatments used give results typical of the intended surface type, the following steps were taken to aid in obtaining the most representative data:

(1) specimens of like orientation and conductivity type were mounted in sets on a common block with the oriented face upward and arranged so that the resistivity was a somewhat random function of position;

(2) the order in which the probes were used for any surface preparation was randomized; and

(3) fresh surfaces were prepared each time a different set of probes was used to make the measurement.

The calibration relation was found to depend both on surface preparation and probe set used for *n*-type silicon; there was no probe dependence for *p*-type silicon. Strong nonlinearities were observed for all orientations of *n*-type silicon with lapped surfaces and for (111) *n*-type silicon with mechanically polished surfaces; smaller nonlinearities have also been observed for lapped surfaces of (111) *p*-type silicon. Such nonlinearities have been modeled in terms of barrier effects at the metal-semiconductor spreading resistance contact [6,7]. Results are presented below for the three major classes of silicon conductivity type and surface orientation [8].

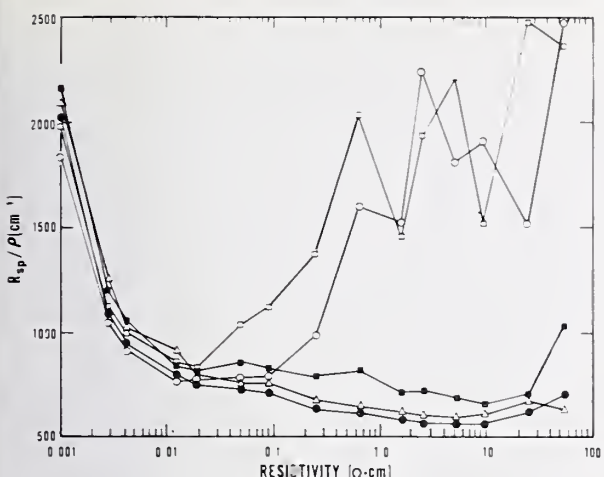
The simplest case is that of *p*-type silicon with (111) surface orientation. As shown in figure 1a, nearly linear relations between

spreading resistance and resistivity are obtainable on surfaces of specimens with resistivity above 0.01 $\Omega \cdot \text{cm}$ either by polishing in aqueous media followed by thermal treatment (bakeout) or by polishing in nonaqueous media. The nonlinearity observed for lower resistivity specimens is believed to be due to a combination of power-supply limitations and series resistance effects.

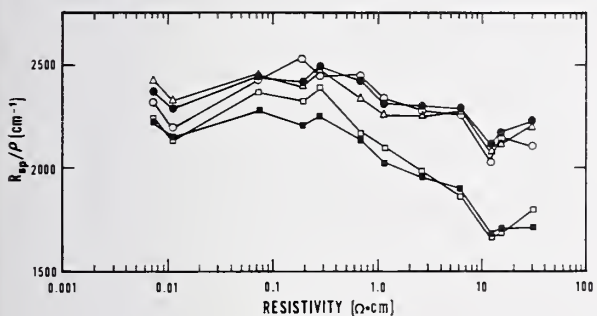
The effect of specimen preparation on (100) *n*-type silicon is nearly as well defined as that described above. Results from probes with relatively low average spreading resistance, osmium or tungsten-osmium, show nearly linear responses with resistivity for all surface conditions as illustrated for tungsten-osmium in figure 1b. Data from the other two probe sets, tungsten carbide and tungsten-ruthenium, tend to show slight deviations from this linear behavior. Since these alloys have higher average spreading resistance and smaller areas of contact than the osmium and tungsten-osmium probes, the anomalous results cannot be explained in terms of alloy composition alone. Results, illustrated in figure 1c, obtained with tungsten carbide probes are consistent with a residual barrier effect of a type which is more prominent on lapped surfaces of *n*-type specimens for all probe materials. The tungsten-ruthenium probe data exhibit some of the same apparent barrier effect and, on the whole, provide the most erratic results of all the probe sets in terms of local scatter about the general resistivity.

The situation for (111) *n*-type silicon is much more complex. For no combination of polishing preparation and probe material do the resultant data show an absence of the barrier-type nonlinearities so prominent on lapped specimens. The form of the resistivity dependence has a strong dependence on the probe set used. The higher the average spreading resistance for a given probe set, the larger are the deviations from linearity attributable to barrier effects, regardless of the polishing procedure used. Tungsten-ruthenium probes were in most frequent need of probe reconditioning, and the data obtained with these probe materials are the most erratic of any taken. The plots of figures 1d and 1e exhibit surface-preparation dependence for two sets of probe materials - tungsten-osmium and tungsten carbide; data from other probe materials (except for tungsten-ruthenium) generally fall within the bounds loosely defined by these plots. For chem-mechanically polished surfaces, the deviations from linear behavior are reduced

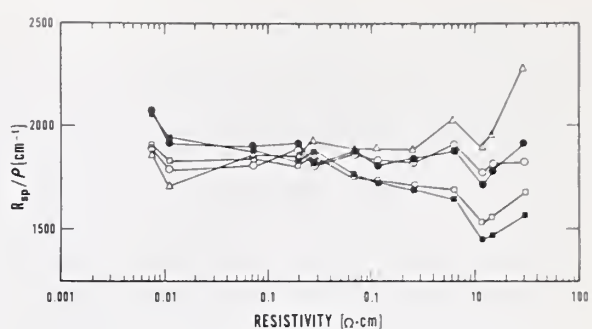
MATERIALS CHARACTERIZATION BY ELECTRICAL METHODS



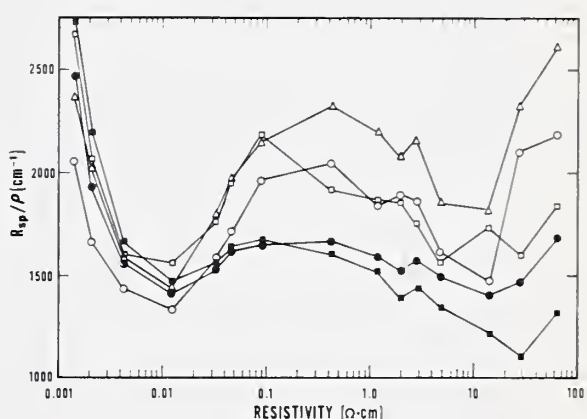
a. *p*-type silicon, (111) orientation,
tungsten-osmium probes.



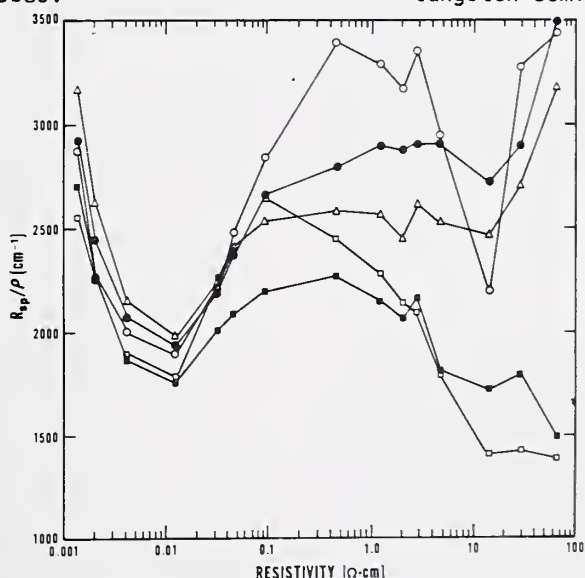
c. *n*-type silicon, (100) orientation,
tungsten carbide probes.



b. *n*-type silicon, (100) orientation,
tungsten-osmium probes.



d. *n*-type silicon, (111) orientation,
tungsten-osmium probes.



e. *n*-type silicon, (111) orientation,
tungsten carbide probes.

Figure 1. Typical calibration relations between measured spreading resistance and resistivity of silicon for selected cases.

for all probes by use of the bakeout cycle. For specimens mechanically polished in an aqueous medium, barrier nonlinearities were noticeably more in evidence than for chem-mechanically polished specimens and in general were centered at a somewhat higher resistivity; following a bakeout cycle, the nonlinearities attributable to barrier effects were reduced, and drastic differences in the responses of the several probe sets appeared. For specimens mechanically polished in the nonaqueous medium the results were in general agreement with those obtained on surfaces polished in an aqueous medium after bakeout, but additional changes in spreading resistance occurred when the surfaces polished in a nonaqueous medium were baked.

(J. R. Ehrstein and D. R. Ricks)

Computational Algorithms for Depth-Profile Measurements — This task was undertaken to develop simplified correction factors for rapid calculation of resistivity or dopant-density profiles from spreading resistance measurements on beveled sections of semiconductor structures (NBS. Spec. Publ. 400-19, p. 10). In this regard, certain simplifying assumptions concerning the nature of the spreading resistance measurement are made; the quality of the resultant abbreviated algorithm is being tested in several ways [9].

Initial efforts were directed at using the formalism of incremental sheet resistance measurements [10] to extend the concepts applied to the analysis of thin uniform slabs to the analysis of regions of nonuniform resistivity on nonconducting substrates. For a two-probe configuration, the measured spreading resistance, R_{sp} , of a thin uniform slab of resistivity, ρ , on an insulating substrate is [11]

$$R_{sp} = \frac{F\rho}{2a} = \frac{\rho}{\pi t} \ln \frac{s}{a} \quad (4)$$

where $F = (2a/\pi t)\ln(s/a)$ is the correction factor for finite slab thickness, s is the probe spacing, a is the effective contact radius of the probe tips, and t is the slab thickness. The factor ρ/t is the sheet resistance, R_s , of the slab. If the spreading resistance is measured as a function of probe spacing and R_{sp} is plotted as a function of $\log s$, a straight line results with a slope equal to $0.733 R_s$ and an (extrapolated) intercept (at $R_{sp} = 0$) where $s = a$.

To test the validity of eq (4) on thin, non-uniform layers, spreading resistance was measured as a function of probe spacing on three thin diffused layers formed by diffusing boron into phosphorus-doped silicon. Plots of the resulting data, with s on a logarithmic scale as shown in figure 2, are linear and have a common intercept at $s \approx 2 \mu\text{m}$. As indicated in table 1, reasonable agreement was obtained between the values of sheet resistance calculated from these plots and those measured directly with a four-probe array. These results are taken as confirmation of the validity of using this form of the correction factor in conjunction with measurements on thin, nonuniform isolated regions. The experiment also provides a useful procedure for determining the effective contact radius.

For profiling, one seeks the functional relationship between measured spreading resistance and resistivity or dopant density at all positions within the layer. The conductivity profile of a thin, nonuniform slab on an insulating substrate can be represented by that of N very thin layers each having a uniform conductivity incrementally different

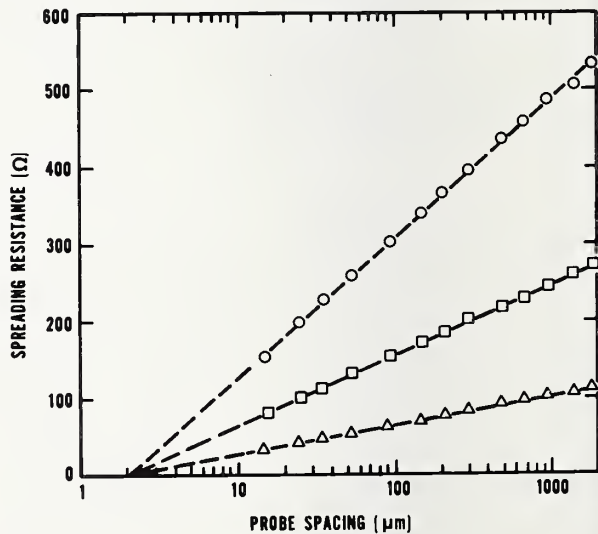


Figure 2. Spreading resistance, R_{sp} , measured as a function of probe spacing, s , for three boron-diffused wafers with different sheet resistances. (The slope of the curve, the ratio of ΔR_{sp} to $\Delta \log s$, is equal to $0.773 R_s$, where R_s is the sheet resistance of the layer; the extrapolated intercept, $R_{sp} = 0$, occurs for $s = a$, the effective contact radius.)

Table 1 - Sheet Resistance of Three Boron-Diffused Wafers

Specimen	Surface Density, cm ⁻³	Junction Depth, μm	Sheet Resistance, Ω (Four-Probe Method)	Sheet Resistance, Ω (Slope of R _{sp} vs. log s)
1	~10 ¹⁹	0.9	284	250
2	~10 ¹⁹	1.7	126	126
3	~10 ¹⁹	4.8	54.6	52

from that of the adjacent layers as shown in figure 3a. If the total thickness of the slab, t , is less than the contact radius, a , the contacts may be considered as cylinders extending throughout the entire slab. Since the conductive regions are in parallel, the conductances add. The conductance between the cylindrical contacts is given by

$$G_0 = \frac{\pi}{\ln(s/a)} \sum_{i=1}^n \sigma_i (z_i - z_{i-1}) . \quad (5)$$

If the top layer is removed, the conductance becomes

$$\begin{aligned} G_1 &= \frac{\pi}{\ln(s/a)} \sum_{i=2}^n \sigma_i (z_i - z_{i-1}) \\ &= G_0 - \frac{\pi}{\ln(s/a)} \sigma_1 (z_1 - z_0) . \end{aligned} \quad (6)$$

This equation may be rewritten in terms of an arbitrary j th layer to yield an expression for its conductivity

$$\sigma_j = - \frac{\ln(s/a)}{\pi} \frac{\Delta G_j}{\Delta z_j} , \quad (7)$$

where $\Delta G_j = G_j - G_{j-1}$ and $\Delta z_j = z_j - z_{j-1}$. In the limit as Δz tends to zero, eq (7) becomes

$$\sigma(z) = - \frac{\ln(s/a)}{\pi} \frac{dG}{dz} . \quad (8)$$

This analysis can be extended to the case of layers thicker than a contact radius [9]. In the extended analysis, additional terms are present containing the second derivative of the inverse correction factor, $H(t)$ (NBS Spec. Publ. 400-19, p. 10). As a first approximation, terms containing the second derivative of $H(t)$ are assumed to be negligible compared

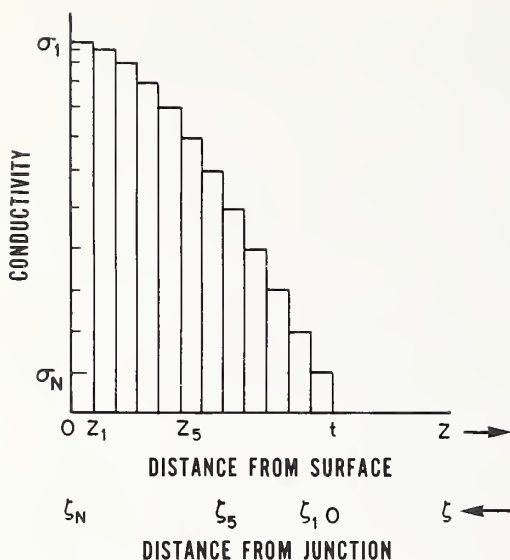
with the right-hand side of eq (8). Equation (8) is used by first applying it to the deepest point of the layer being profiled (because here the correction depends only on the boundary condition and not on the nature of the profile itself) and then working out toward the surface. It is therefore convenient to shift the coordinate system so that the origin is at the junction, that is, at the interface between layer and insulating substrate:

$$\sigma(\zeta) = \frac{\ln(s/a)}{\pi} \frac{dG}{d\zeta} \quad (9)$$

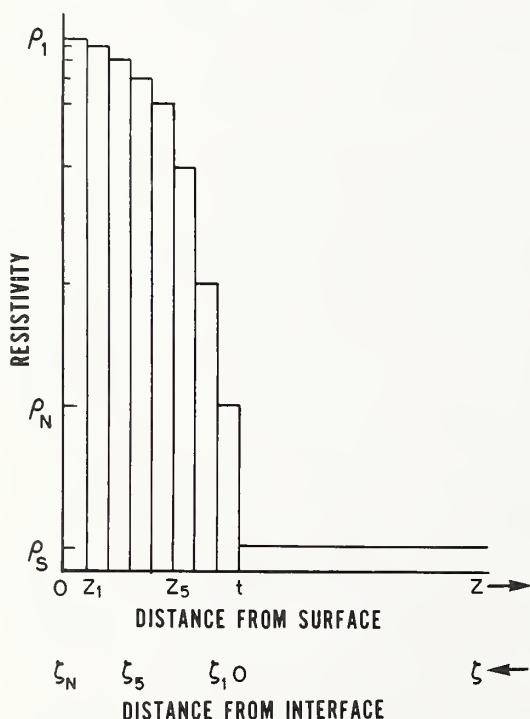
where $\zeta = t - z$, and t is the total layer thickness.

The concept of parallel superposition was tested by calculating the correction factors for a variety of three-layer structures and comparing the results with correction factors calculated from the Schumann-Gardner solution [12], which is assumed to be exact. It was concluded [9] that the parallel superposition approximation yields results which agree to within 10 percent only in a limited number of cases. It appears to be most satisfactory for cases in which the conductivity decreases as the insulating substrate is approached or in which the thickness of the layer is less than the effective contact radius.

At the other extreme, one can consider a relatively high-resistivity region on a low-resistivity substrate, again modeled in terms of N very thin layers, as shown in figure 3b. If the thickness, t , of the region is small, the current travels through the high-resistivity region to the substrate in a direction nearly perpendicular to the surface. The resistance measured at the surface can be approximated as the sum of the incremental resistances, ρ_i , in the cylinder below each contact disk and the spreading resistance between the virtual contacts on the substrate is given by



- a. Conductivity profile of thin, nonuniform slab on an insulating substrate.



- b. Resistivity profile of thin, high-resistivity region on low-resistivity substrate.

$$R_0 = 2 \sum_{i=1}^n \rho_i \frac{(z_i - z_{i-1})}{\pi a^2} + \frac{\rho_s}{2a} \quad (10)$$

where ρ_s is the resistivity of the substrate.

If the top layer is removed, the new resistance R_1 will be smaller by the first term in the sum:

$$R_0 - R_1 = 2 \rho_1 \frac{(z_1 - z_0)}{\pi a^2}. \quad (11)$$

As before, this equation may be rewritten in terms of an arbitrary j th layer to yield an expression for its resistivity:

$$\rho_j = - \frac{\pi a^2}{2} \frac{\Delta R_j}{\Delta z_j} \quad (12)$$

where $\Delta R_j = R_j - R_{j-1}$ and $\Delta z_j = z_j - z_{j-1}$. In the limit as Δz tends to zero, eq (12) becomes

$$\rho(z) = - \frac{\pi a^2}{2} \frac{dR}{dz}. \quad (13)$$

It is again convenient to shift the coordinate system so that the origin is at the interface between the layer and the substrate, at $z = t$, with the result that:

$$\rho(\zeta) = \frac{\pi a^2}{2} \frac{dR}{d\zeta}, \quad (14)$$

where $\zeta = t - z$.

In practice the data are obtained in terms of the common logarithm of the spreading resistance as a function of distance. Since

$$\frac{dy}{dx} = y \frac{d \ln y}{dx},$$

$$\ln y = \ln 10 \log y,$$

and

$$\frac{dG}{d\zeta} = - \frac{1}{R^2} \frac{dR}{d\zeta},$$

it is possible to rewrite eqs (9) and (14) in terms of the spreading resistance, R_{sp} , and the local slope, m , of the raw spreading resistance data:

$$\sigma(\zeta) = - \ln 10 \frac{\ln(s/a)}{\pi} \frac{m}{R_{sp}}, \quad (9a)$$

Figure 3. Profiles constructed by superposition of multiple uniform layers.

and

$$\rho(\zeta) = \ln 10 \frac{\pi a^2}{2} R_{sp} m , \quad (14a)$$

where

$$m \equiv \frac{d \log R_{sp}}{d\zeta} .$$

For thin layers on an insulating substrate, eq (9a), m is large and negative; for thin layers on a conducting substrate, eq (14a), m is large and positive.

In general, the basic equations which relate conductivity or resistivity to spreading resistance are written

$$\sigma = F/2aR_{sp} , \quad (9b)$$

and

$$\rho = 2aR_{sp}/F . \quad (14b)$$

Comparing eqs (9a) and (14a) with (9b) and (14b) one finds that for the limiting case of the insulating substrate

$$F = - \frac{2a \ln(s/a)}{\pi} m \equiv - K_1 m , \quad (9c)$$

and for the limiting case of the conducting substrate

$$F = \frac{4}{\pi a} \frac{1}{m} \equiv \frac{K_2}{m} . \quad (14c)$$

Each of these correction factors, if used separately, would be applied to the raw data as follows to obtain the true spreading resistance:

$$R_{sp}(\text{corr}) = R_{sp}(\text{raw})/F . \quad (15)$$

Since the forms given are limiting forms, the proper method for combining them to describe more general device structures is not intuitively clear. The trial combination

$$F = \frac{K_1 m}{2} + \sqrt{\left(\frac{K_1 m^2}{2} \right) + K_1 K_2} \quad (16)$$

reduces to the limiting forms above for $m \gg 0$ and $m \ll 0$. It can be seen, however, that for the trivial case of profiling a uniform bulk specimen, for which $m = 0$, the cor-

rection factor reduces to $(K_1 K_2)^{1/2}$, or $(8 \ln(s/a)/\pi^2)^{1/2}$, rather than to unity, as it should for such a specimen. This form of the correction factor was tested against the Schumann and Gardner solution [12] in a manner similar to that described above for parallel superposition. For this purpose, the term $K_1 K_2$, which makes a negligible contribution to F when $m \gg 0$, but contributes more and more to F as m approaches zero, was arbitrarily set to unity.

The first step in the computer evaluation of correction factors from the local slope for selected three-layer configurations was the determination of local-slope values for each configuration. This evaluation was accomplished by numerical integration of the correction factors due to Schumann and Gardner [12] for top layer thicknesses slightly smaller and slightly larger than the arbitrary thickness value selected in the evaluation, for each configuration considered, and using the differences to compute the local slope [9]. It was found that for the case of two thin layers on a third thick layer, the local-slope method with $K_1 K_2 = 1$ provides results that are nearly as accurate as those obtained by parallel superposition for most conditions when the conductivity decreases with depth. For the same configuration, the local-slope method provides substantially more accurate results than parallel superposition when the conductivity increases with depth. For configurations in which all the layers are thicker than the existing contact probe radius, the agreement of this form of local-slope evaluation with the results from Schumann and Gardner is very satisfactory.

For three layers of equal thickness, the local-slope method provides results that are marginally inferior to those from parallel superposition for cases where the conductivity decreases with depth. However, the local-slope evaluation agrees better with the Schumann-Gardner results for a much wider range of layer configurations than the parallel-superposition method.

Following the computer evaluation, an experimental test of the local-slope algorithm was conducted. Profiles on six diffused specimens as determined from spreading resistance measurements corrected by the local-slope method were compared with the profile as measured by the incremental sheet resistance method as described previously (NBS Spec. Publ. 400-29, pp. 11-13).

Table 2 - Characteristics of Diffused Layered Structures Used for Spreading Resistance Measurements

Specimen ^a	Substrate Sheet Resistance, Ω			Junction Depth, μm		
	Resistivity, $\Omega \cdot \text{cm}$	Four-Probe	Spreading Resistance (Integrated Profile)	Incremental Sheet Resistance (Extrapolated)	Spreading Resistance	Angle Lap and Stain
PB03	0.03	77	81	1.5	1.6	2.0
PB1	1	59	63	1.9	2.0	2.6
PB100	100	54	57	2.0	2.5	2.8
BP03	0.03	132	195	1.6	1.5	2.0
BP1	1	88	125	1.9	2.0	2.5
BP150	150	88	112	2.8	2.7	2.8

^aThe first letter represents the dopant in the diffused layers and the second letter represents the dopant in the substrate; B = boron; P = phosphorus.

The test specimens were fabricated with two-step diffusions to give approximately Gaussian profiles of dopant density with depth, with dopant density at the surface of about 10^{19} cm^{-3} and junction depths between 2 and 3 μm . The characteristics of the test specimens are listed in table 2. The incremental sheet resistance measurements were made on 1-in. (25-mm) diameter disks which were cut ultrasonically from 2-in. (51-mm) diameter starting wafers; the spreading resistance measurements were made on beveled chips taken from adjacent sections of the same wafers. Results were compared in terms of conductivity profiles to minimize differences resulting from conversions between conductivity and net dopant density.

The spreading resistance analysis was carried out as follows: raw spreading resistance data were taken for a shallow bevel section of each specimen chip and were then stored in the calculator memory. The bevel angle for each chip was measured by an optical small-angle measurement technique [13]. The spreading resistance data were corrected using eq (15) beginning with data at the junction and proceeding outwards toward the top surface of the structure. For this test, the form of the correction factor was modified slightly from that used for the initial testing of the local-slope model; the term $K_1 K_2$ in eq (16) was replaced by

$$K_3 = 1 + \left[\frac{81n(s/a)}{\pi^2} - 1 \right] \tan^{-1} \left[\log \frac{R_o}{R_s} \right], \quad (17)$$

where R_o and R_s are the measured spreading resistances at the site being corrected and at a site one contact radius deeper, respectively; if the site one contact radius from the site being corrected is on the opposite side of an isolating junction from that site, then the value used for R_s is the value of spreading resistance as measured at the junction. The arctan function is expressed in radians, and the value of a is determined from a measurement of spreading resistance as a function of probe separation on the top surface of the structure to be profiled; for the diffused specimens being analyzed, a was found to be 1.1 and 2.1 μm for the n - and p -type layers, respectively. The form used here for K_3 allows F to approach the same limiting values as previously for the cases of insulating and conducting substrates, $m \gg 0$ and $m \ll 0$, and in addition gives a value of $F = 1$ when the layers are uniform, $m = 0$.

Conductivity values were then calculated using eq (9b). The results are shown in figure 4. Table 2 lists the sheet resistance values determined by four-probe measurements [14] at the beginning of the incremental sheet resistance measurement procedure and those obtained by integrating the conductivity pro-

MATERIALS CHARACTERIZATION BY ELECTRICAL METHODS

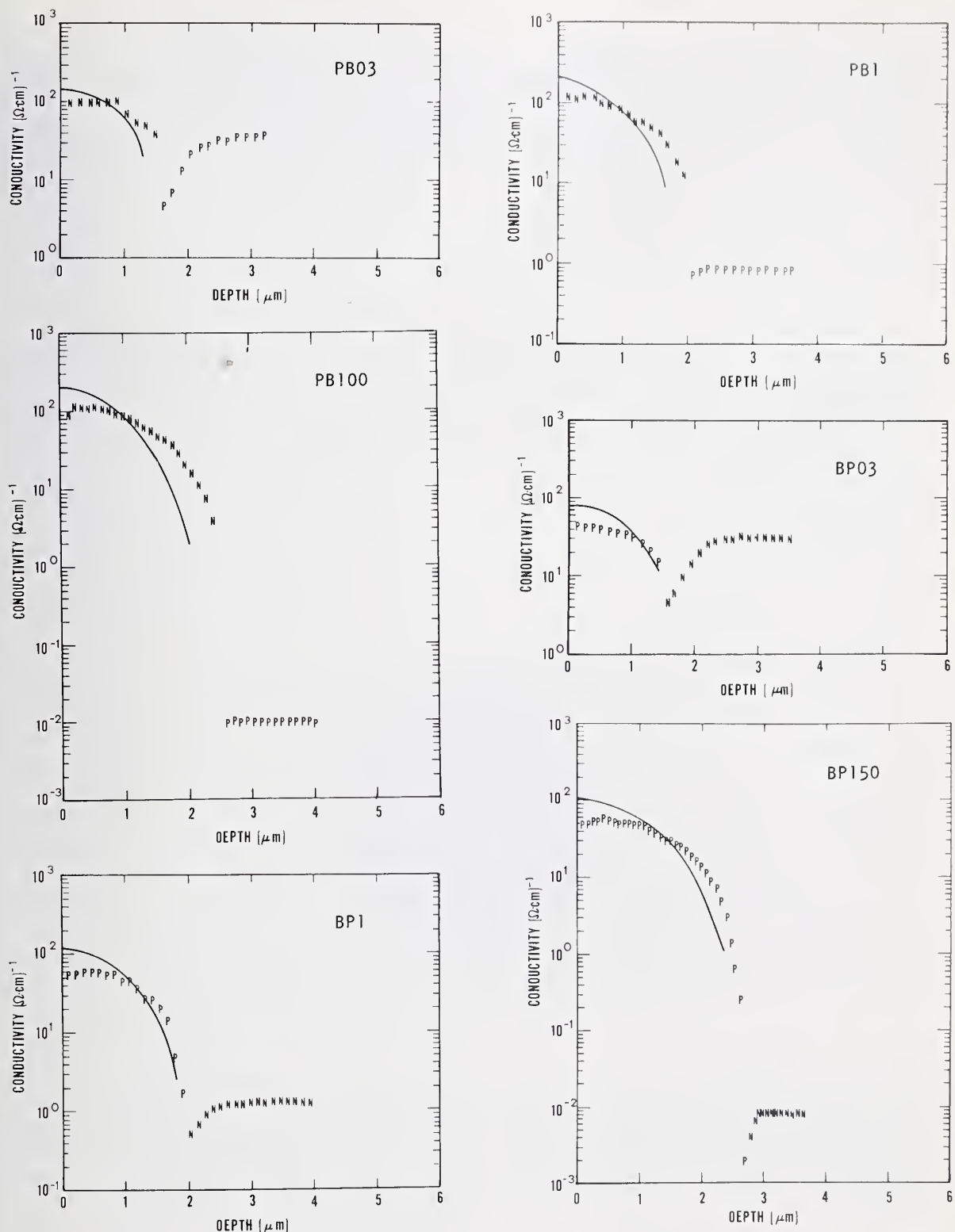


Figure 4. Conductivity profiles for selected diffused layers. (N,P: from spreading resistance data, corrected by the local-slope method. Solid curves: from incremental sheet resistance measurements. See table 2 for specimen identification.)

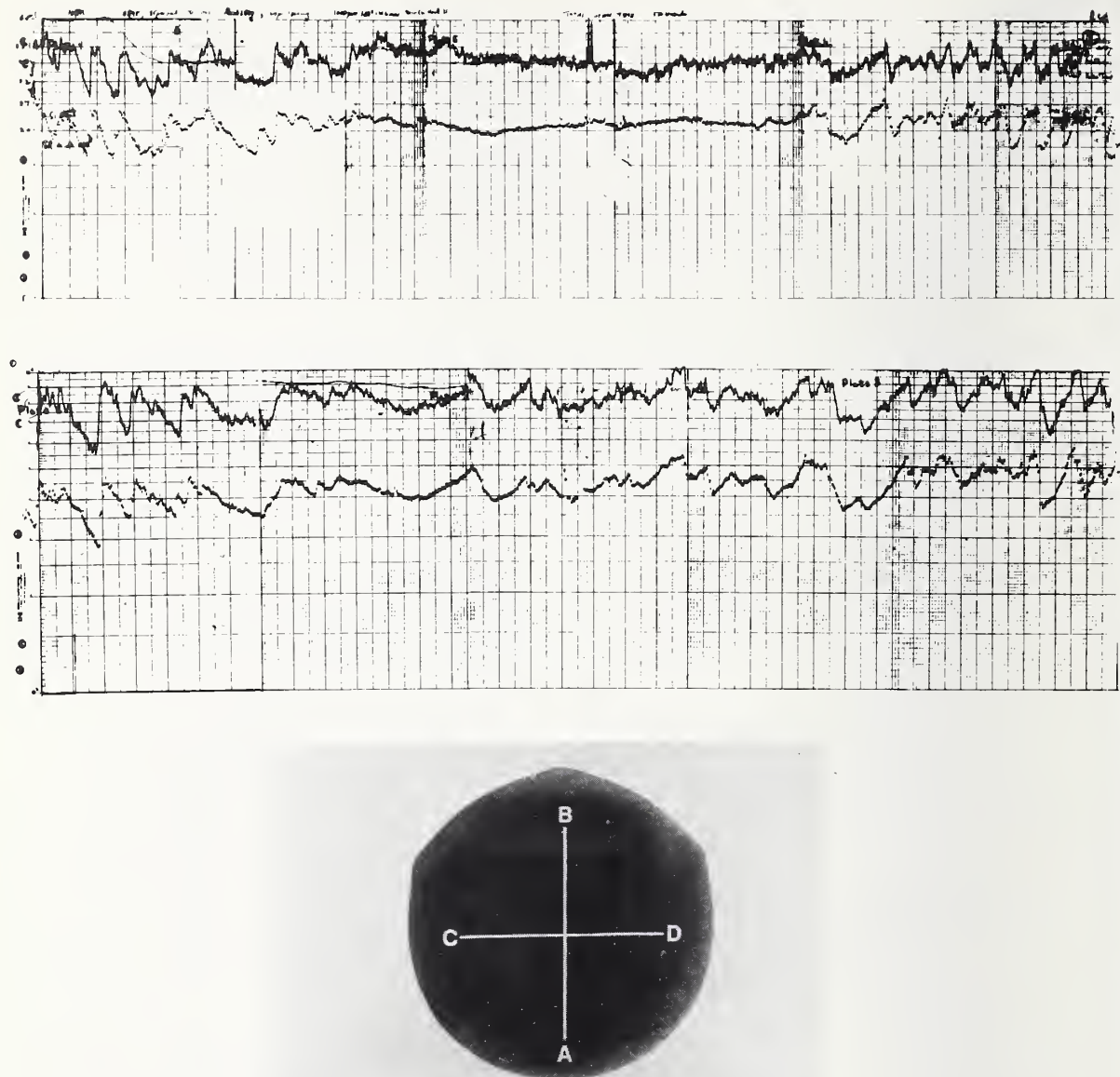


Figure 5. Comparison of traces from high-speed dragging-stylus and conventional stepping-type spreading resistance measurements in two orthogonal directions on an *n*-type silicon slice with an average resistivity of $2.5 \Omega\text{-cm}$ and a (111) surface orientation. (The upper pair of traces was taken along the line A to B, as shown in the plan view, and the lower pair along C to D. In each pair, the upper trace is from the high-speed dragging-stylus instrument and the lower trace is from the conventional instrument stepping at intervals of $25 \mu\text{m}$.)

file obtained from corrected spreading resistance profiles. It also lists junction depths obtained from (1) extrapolation of the incremental sheet resistance data to the resistivity of the substrate, (2) the corrected spreading resistance data, and (3) direct measurement by the angle lap and stain method [15]. Sources of error which would account for the observed discrepancies are being investigated.

(D. H. Dickey[§] and J. R. Ehrstein)

High-Speed Dragging-Stylus Probe — This task was undertaken to develop an instrument which could collect spreading resistance data at least 10 times faster than the commercially available stepping-type instrument with little or no degradation of that instrument's electrical performance and probe life characteristics (NBS Spec. Publ. 400-19, pp. 10-13). A variety of probe tip materials and tip sizes was selected and tested. All probe tip materials listed previously (NBS Spec. Publ. 400-25, pp. 12-13) were tested with the exception of tungsten. Both 10-μm and 25-μm radius tips were fabricated in many of these alloys; for some, only 25-μm radius tips were available. The tip radius of the tungsten-ruthenium alloy probes was 19 μm. Based on judgments of overall quality of the data obtained with the various probe materials together with lifetimes over which the probes could be effectively reconditioned, Carballoy 895[¶] tungsten carbide alloy [16] with a tip radius of 25 μm and tungsten-ruthenium alloy[¶] [17] with a tip radius of 19 μm appear to be the preferred probe materials. Both alloys have very fine grain size, and of the tungsten carbide alloys, 895 has the highest abrasion resistance and highest rated compressive strength. These judgments were made on the basis of a probe loading of 530 mN for the blunter probes and probe loading of 150 to 210 mN for the sharper probes. The loading for the sharper probes was selected with the intent of maintaining approximately constant force per unit area at the contact and was modified in part by the observed width of the track pattern left on specimens by the probes.

The two preferred alloys exhibit point life in excess of 9 m of cumulative specimen probing with reconditioning every 2 to 3 m. A different reconditioning procedure appears to be preferable to the previously used procedure of dragging the probes over an abraded silicon surface or over a plate covered with diamond polishing paste. The new procedure, not yet automated and hence subject to operator variability, consists of removing the

probe holders from the measurement instrument and touching each probe tip for a few seconds to a rotating hard (steel or sapphire) disk covered with 3-μm diamond paste. A rocking motion is imparted to the tip so as to abrade and recondition the entire radius of the tip. The probe tip is subsequently swabbed with fluorocarbon-methylene chloride, reattached to the probe station, and drawn across the surface of a polished silicon wafer for 50 to 100 mm while under normal operating load. The whole operation takes just a few minutes and the calibration graphs were found not to be changed by the reconditioning.

The previously used lubricant, butoxy ethoxy ethanol, was replaced because it had an unpleasant odor. Evaluation of a number of other lubricants (methanol, propylene glycol, synthetic engine oil, and several fluorocarbons) showed No. 43 fluorocarbon[¶] [18] to be the only one of these which met the desired conditions of low volatility, lack of toxicity, low conductivity, and low viscosity; it can be readily removed with methanol. It was used for all recent wear tests and calibration evaluations.

To illustrate the resolution and signal-to-noise ratio obtainable with the high-speed dragging-stylus instrument when using Carballoy 895[¶] probes, spreading resistance measurements were made on a freshly polished 2-in. (51-mm) diameter *n*-type silicon slice with an average resistivity of about 2.5 Ω·cm and a (111) surface orientation. The results are presented in figure 5 together with the results obtained at NBS with a conventional instrument which was stepped at intervals of 25 μm. The profile was obtained in about 4 min using the high-speed instrument, as compared to 80 min for the profile with the conventional stepping-type instrument. It can be seen that the striation patterns measured by the two instruments are essentially the same.

(A. Mayer[#] and N. Goldsmith[#])

[§] Work performed at Solecon Laboratories under NBS Contract No. 5-35881.

[¶] See disclaimer, p. vi.

[#] Work performed at RCA Laboratories under NBS Contract No. 5-35914. NBS contact for additional information: J. R. Ehrstein.

3.3. Capacitance-Voltage Methods

A new method was developed to extract background dopant densities in the range from 10^{16} to about 10^{18} cm^{-3} from junction capacitance-voltage (C-V) data [19]. When the conventional method of calculation [20] is applied to specimens having large ($\gtrsim 5 \times 10^{16} \text{ cm}^{-3}$) background dopant density, the dopant density profile may not level off at the background dopant density because in such specimens the depletion region cannot be driven out of the compensated region which exists near the junction.

In the new method, the C-V data are corrected for peripheral effects, and a profile uncorrected for diffused layer effects is calculated [20]. Given the junction depth for a Gaussian diffusion, a succession of estimates of the ratio, R, of effective surface dopant density to background dopant density is made until the correct value is found. For each such estimate the dopant density profile of the uncompensated background is calculated. When the slope of a least-squares linear fit through the points of this profile is sufficiently small, the estimate of R is judged to be correct, and the average of the most recently calculated background dopant density values is taken as the average background dopant density.

The method has been evaluated using both real and theoretical C-V data [19]. Satisfactory results were achieved when the method was applied to specimens with background dopant density as large as 10^{18} cm^{-3} ; above this value, the depletion region lies only in the linearly graded region. Since an average value rather than a profile of discrete points is calculated, the method is not suitable for measuring regions of varying dopant density, such as epitaxial layer-substrate interfaces. The method is not appropriate for use on specimens with low ($\lesssim 10^{15} \text{ cm}^{-3}$) background densities in which an appreciable real gradient exists. In such instances, no diffused layer correction exists which can cause the uncompensated background dopant density profile to be flat.

(R. L. Mattis and M. G. Buehler)

3.4. Hole Mobility in *p*-Type Silicon

It was noted previously (NBS Tech. Note 806, pp. 20-24) that the calculated conductivity mobilities for holes in *p*-type silicon were considerably larger than the measured mobilities for dopant densities greater than

10^{16} cm^{-3} . This discrepancy may be attributed in part to the inadequacy of the theoretical model used in the mobility calculations and in part to the use of total dopant density to derive the mobility values from resistivity data, without properly taking into account the deionization of the acceptor impurities with increasing dopant density. Experimental data obtained by Wagner [21] on boron-implanted silicon showed significant differences from Irvin's classical curves [22] for acceptor densities greater than 10^{16} cm^{-3} (NBS Spec. Publ. 400-4, pp. 13-14). The present task was undertaken to derive theoretical expressions for mobility in *p*-type silicon that would yield satisfactory agreement with experimental data.

The total hole mobility can be obtained by weighting the mobilities of the holes in the heavy, light, and the spin-orbit splitting bands, μ_1 , μ_2 , and μ_3 , respectively, according to their relative populations in each band:

$$\mu_p = \left[\frac{\mu_1 + \mu_2 \left(\frac{m_2^*}{m_1^*} \right)^{3/2} + \mu_3 \left(\frac{m_3^*}{m_1^*} \right)^{3/2}}{1 + \left(\frac{m_2^*}{m_1^*} \right)^{3/2} + \left(\frac{m_3^*}{m_1^*} \right)^{3/2}} \right] \quad (18)$$

The density-of-states effective masses, m_1 , m_2 , and m_3 , for the three bands were obtained from the results given by Barber [23]. At 300 K, one finds that $m_1^* = 0.537m_0$, $m_2^* = 0.43m_0$, and $m_3^* = 0.134m_0$, where m_0 is the free electron mass, so that eq (18) reduces to

$$\mu_p = 0.543(\mu_1 + 0.7165\mu_2 + 0.1247\mu_3) \quad (19)$$

The hole mobility of each band is calculated separately by taking into account the contributions of lattice, ionized impurity, and neutral impurity scattering. In addition, the effect of hole-hole scattering is included for dopant density greater than 10^{16} cm^{-3} . The lattice mobility, μ_L , was

based on the results of Costato and Reggiani [24] which give a lattice mobility value of $475 \text{ cm}^2/\text{V}\cdot\text{s}$ at 300 K. For ionized impurity scattering, the Brooks-Herring [25] formula was used for the calculation of impurity mobility, μ_I , and the formula given by Sclar [26] was used for the calculation of neutral impurity mobility, μ_N . The detailed proce-

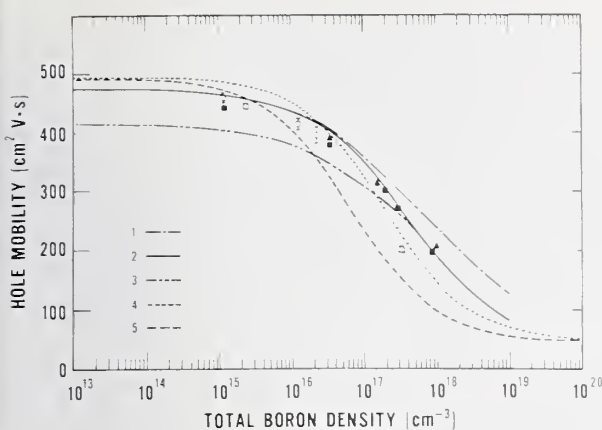


Figure 6. Preliminary results of hole mobility calculations in boron-doped silicon at 300 K. (Curve 1: calculated without hole-hole scattering; curve 2: calculated with hole-hole scattering at higher hole densities; curve 3: calculated with hole-hole scattering over entire range; curve 4: Wagner curve [21]; curve 5: Irvin curve [22]; ○, ▲, ■ experimental data; see text for discussion.)

dures for computing μ_1 , μ_2 , and μ_3 are similar to those used previously in calculating the electron mobility in n -type silicon [27] (NBS Spec. Publ. 400-29, pp. 17-19). The results of the calculation, which are shown in figure 6, are in reasonable agreement with preliminary data taken in cooperation with ASTM Committee F-1 (NBS Spec. Publ. 400-4, pp. 13-14). These data were obtained by combining four-probe resistivity measurements with measurements of Hall coefficient of ultrasonically machined bar-shaped specimens (solid squares) and of capacitance-voltage characteristics of ungated diodes (solid triangles). In the dopant density range from 10^{15} to $3 \times 10^{16} \text{ cm}^{-3}$ the results of the calculations also agree fairly well with more recent data (NBS Spec. Publ. 400-29, pp. 15-17). These data (open circles) were obtained with the planar square array four-probe and gated junction test structures of test pattern NBS-3 [28]. However, these data appear to fall closer to Wagner's curve in the dopant density range above 10^{17} cm^{-3} ; revisions to the calculated curve are being made to improve the fit to the more recent experimental results.

It should be noted that there are differences in the mobility relationships for silicon doped with different acceptor impurities [29] because of differences in fractional ionization in the dopant density range from

10^{16} to 10^{19} cm^{-3} even at room temperature. At the present time, additional experimental data are being collected on boron-doped silicon specimens, and these theoretical formulations for the mobility and resistivity calculations in boron-doped silicon are being extended to cover the temperature range from 77 to 400 K. (S. S. Li)

3.5. Indium-Doped Silicon

The intrinsic, across-the-band-gap photosensitivity of silicon is limited to wavelengths shorter than about 1 μm . However, the photoresponse of silicon can be extended to longer wavelengths by photoionizing dopant states which have been deionized by cooling to cryogenic temperatures. Silicon doped with antimony, arsenic, boron, gallium, indium, or phosphorus has been used for the detection of infrared radiation in various wavelength regimes out to almost 30 μm [30-31]. Extrinsic silicon detectors have a large potential application in infrared imaging systems in which a large number of detector elements are combined into a two-dimensional mosaic that can be fabricated monolithically along with the necessary read-out circuitry. Integrated image sensors of this kind are being developed for remote-sensing reconnaissance and surveillance applications [32-34].

Although silicon may be one of the most studied elements and the one for which the technology is the most advanced, it is a relatively new arrival on the infrared detector scene. Extrinsic infrared detection in silicon depends critically on properties that are often of only secondary importance to other silicon devices. Therefore, a need has arisen to develop suitable methods of measuring these properties to characterize silicon with respect to its ability to detect infrared radiation. For example, it is necessary to measure and control the impurity compensation, which plays a critical role through its effect on the lifetime of the photoexcited extrinsic carriers. The existence of any "extra" levels introduced by impurity pairing or impurity-defect complexes could complicate the compensation scheme, affect the lifetime, and thus become very important. The situation is further complicated by the stringent requirements for uniformity of the infrared photoresponse imposed on mosaic arrays of imaging elements intended for thermal imaging applications. A single point measurement is inadequate for characterization of silicon photoresponse for mosaic applications because of the requirement for uniformity of

response over the extended area of the mosaic. In addition, it would be highly desirable to be able to perform uniformity measurements nondestructively on wafers before they are processed into mosaics. Such a procedure would screen out the rejects at an early stage and, by eliminating unnecessary processing of bad wafers, result in reduced costs and increased ultimate yield.

The present task was undertaken to identify and develop appropriate measurement technology to address these problems. Initial efforts are being concentrated on evaluation of various techniques to detect extraneous levels in indium-doped silicon. One such level has been named the X-level and appears to be an acceptor state located about 0.11 eV above the valence band [35]. The presence of this level in amounts considerably smaller than indium density reduces the performance of indium-doped infrared detectors and makes it necessary to operate them at lower temperatures than otherwise in order to obtain the best signal-to-noise ratio. (R. D. Larrabee)

3.6. Thermally Stimulated Current and Capacitance

Gold Donor in p-Type Silicon MOS Capacitor — Measurements of thermally stimulated current and capacitance were made on a gold-doped p-type silicon MOS capacitor. Theoretical models [36] suggest that the phase I thermally stimulated current and capacitance response of the gold donor center in this structure should be the same (except for a geometric scale factor) as the response of the same center in an n^+p junction diode [37]; this expectation was confirmed in the measurements. The capacitor used was structure 3.8 of test pattern NBS-3 [28]. The peripheral gate was biased into accumulation (-25 V) and the main gate was deeply inverted (+12 V) during cooling and biased into deep depletion (+22 V) immediately before the heating cycle was begun. The current and capacitance are shown in figure 7 as a function of temperature for various heating rates. The measured peak emission temperatures occurred within 0.1 K of the peak temperature calculated from the theoretical model. For this device, the gold donor density and the dopant density were calculated to be $4.2 \times 10^{13} \text{ cm}^{-3}$ and $8.3 \times 10^{14} \text{ cm}^{-3}$, respectively.

Analysis of Isothermal Capacitance Transient Response — Measurement procedures have been established for the characterization of defect centers from analysis of the isothermal

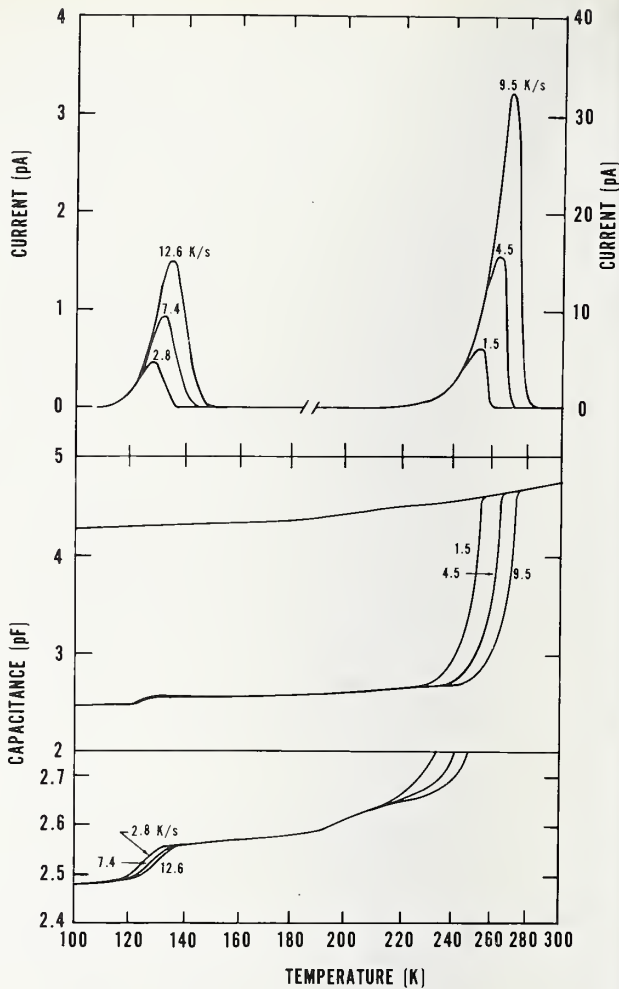


Figure 7. Thermally stimulated current and capacitance response of the gold donor in p-type silicon at various heating rates. (The indicated heating rates are evaluated at the temperature of the current peaks. The bottom curve is a 5x expansion of part of the center capacitance response curve. Device Au 13 P8.8.)

capacitance transient response. To illustrate the procedures, consider the case of the gold donor center in a gated n^+p silicon diode, structure 3.10 of test pattern NBS-3 [28]. Measurements were made on a diode from the same wafer which contained the above MOS capacitor and also one from a wafer with less gold.

The procedure used was as follows: With reverse bias, V_T , applied to the diode and the peripheral gate biased into accumulation, the diode is cooled to one of a series of temperatures in an appropriate range. When an iso-

thermal condition is achieved, the reverse bias is removed (changed to zero bias) momentarily, then reapplied while the capacitance of the diode is recorded as a function of time on an x-y recorder. The transient decay of the junction capacitance that occurs when the bias is changed from zero bias to the reverse bias is controlled in *p*-type silicon by the hole density on defect centers which lie below the mid-gap energy.^x Under one-sided step-junction conditions, the junction capacitance, *C*, is given by

$$C^{-2} = C_b^{-2} + \frac{2V_T}{q\epsilon A^2(N - p_t)} , \quad (20)$$

where C_b is the zero-bias capacitance, A is the junction area, ϵ is the dielectric constant (permittivity) of silicon, N is the total acceptor density, p_t is the hole density on the defect center, and q is the electronic charge. This equation can be solved for p_t to obtain

$$p_t = N - \frac{2V_T C_b^2 C^2}{q\epsilon A^2 (C_b^2 - C^2)} . \quad (20a)$$

The net rate of change of the hole density on the defect center is given by [37]

$$\frac{dp_t}{dt} = e_n n_t - e_p p_t , \quad (21)$$

where e_n is the electron emission rate, e_p is the hole emission rate, and n_t is the electron density on the defect center. By use of the totality condition, $n_t + p_t = N_t$, where N_t is the total defect density, one can eliminate n_t and solve eq (21) with the result that

$$p_t = p_{tf} + (p_{ti} - p_{tf}) \exp[-(e_n + e_p)t] , \quad (22)$$

where p_{ti} is the hole density on the defect center at the start of the transient ($t = 0$) and p_{tf} is the hole density on the defect center at the end of the transient ($t = \infty$).

Equation (22) can be rewritten

$$\frac{p_t - p_{tf}}{p_{ti} - p_{tf}} = \exp[-(e_n + e_p)t] . \quad (23)$$

The capacitance C is C_i at the beginning of the transient when $p_t = p_{ti}$. After an elapsed time equal to several time-constant intervals, t may be taken as infinite: p_t becomes p_{tf} , and C becomes C_f . If p_t , p_{ti} , and p_{tf} are each written in terms of eq (20a) and the resulting expressions are substituted into eq (23) and simplified, the left-hand side of eq (23) is seen to be a ratio of capacitances, denoted C_r :

$$C_r \equiv \frac{(C_b^2 - C_i^2)(C_f^2 - C^2)}{(C_b^2 - C^2)(C_f^2 - C_i^2)} \\ = \exp[-(e_n + e_p)t] , \quad (24)$$

or,

$$e_n + e_p = (\ln C_r)/t . \quad (25)$$

Eight to twenty points are read from the transient capacitance curve, scaled, and replotted as $\log C_r$ against time. A least-

squares fit of the calculated points to a straight line is made, and the time constant is calculated. For cases such as the gold donor center in silicon, for which $e_n \ll e_p$, the reciprocal of the time constant is the hole emission probability, e_p . This procedure is repeated at a number of temperatures in the appropriate range, 120 to 145 K in the case of the gold donor center. Since $e_p = B_p T^2 \exp[\Delta E_p / (kT)]$ (where B_p is the emission coefficient for holes, T is the absolute temperature, ΔE_p is the difference in energy level between trap and valence band, and k is the Boltzmann constant), an Arrhenius plot of $\ln(e_p/T^2)$ against T^{-1} has a slope of $\Delta E_p/k$ and an intercept of $\ln B_p$. The data obtained in the present experiment are plotted in figure 8. These data were fitted by least squares to obtain the values of $\Delta E_p = 0.343 \pm 0.0045$ eV and $B_p = 2.22 \times 10^{8 \pm 0.175}$, in good agreement with the results of diode measurements by Buehler [37], who obtained $0.33 \pm$

^xThe analysis can be extended to the case of defect centers in the upper half of the band gap in *n*-type silicon by a suitable exchange of variables: holes with electrons; acceptors with donors.

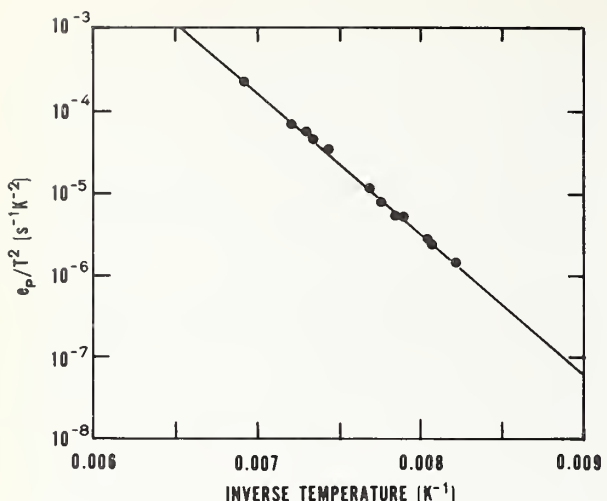


Figure 8. Scaled Arrhenius plot of hole emission probability, e_p/T^2 , as a function of inverse temperature for the gold donor in p -type silicon. (Devices Au 13 P10.11 and Au 10 P10.1.)

0.03 eV and $4.2 \times 10^{8 \pm 1.2}$; and by Sah *et al.* [38], who obtained 0.345 ± 0.0029 and $(2.7 \pm 0.66) \times 10^8$, respectively.

(W. E. Phillips and M. G. Buehler)

Application to Power-Grade Silicon⁺ — This task was undertaken to evaluate the use of measurements of thermally stimulated current and capacitance (TSM) as a means for characterizing defects in power-device-grade silicon wafers. The following were established as the objectives of the first phase of the task:

(1) To design and construct apparatus for performing TSM on large-diameter silicon wafers in the appropriate temperature range;

(2) In order to preserve the characteristics of the starting material, to develop and evaluate a low-temperature process for fabricating MOS capacitors suitable for use in performing TSM on high-resistivity n -type silicon; and

(3) To determine the feasibility of using and interpreting TSM on thyristors after each step in the device fabrication process.

Progress was made during this reporting period toward all three of these objectives.

Table 3 — Performance Characteristics of New Thermally Controlled Chuck

Characteristic	Value
Low temperature limit of top surface	-185°C (88 K)
Low temperature limit of chuck body	-190.9°C (82.9 K)
High temperature limit ^a	~350°C
Minimum elapsed time from room temperature to low temperature limit	<4 min
Minimum elapsed time from low temperature limit to room temperature	<45 s
Maximum heating rate from low temperature limit to room temperature	+5.5 K/s
Minimum elapsed time from room temperature to 300°C	<70 s
Minimum elapsed time from 300°C to room temperature	<110 s

^aestimated

A. Whole-Wafer Apparatus. The new thermally controlled chuck and automatic wafer prober (NBS Spec. Publ. 400-29, pp. 20-22) was assembled and functionally tested. The results of these tests are summarized in table 3. These characteristics meet or exceed the design targets which were selected to permit measurement of thermally stimulated current and capacitance of centers throughout most of the band gap with adequate signal-to-noise ratio and performance of bias-temperature stress tests (to determine mobile ion density in oxide films) with minimal ramp times. Rapid measurements of many devices on the same wafer can be made automatically with the automatic wafer prober, thus facilitating the mapping of characteristics across the wafer (NBS Spec. Publ. 400-25, pp. 43-44).

All systems within the dry-box enclosure are fully operational. The gold acceptor has been identified in both a p^n diode and an n -MOS capacitor on the same gold-doped wafer, using the thermally stimulated current technique. In this environment currents as small as 0.1 pA can be easily detected.

Although the apparatus has been successfully tested, two deficiencies have appeared. First, the stainless-steel bellows used to transport the liquid nitrogen to the chuck

⁺Principally funded by the Energy Research and Development Administration, Division of Electric Energy Systems.

has been found to be too flexible. Although the bellows assembly is mechanically restrained, violent expansion of the liquid-nitrogen vapors causes excess strain in the assembly. Second, the excessive lowering of the ambient temperature within the box causes an intermittent mechanical malfunction of the prober. The low temperature in the box is believed to result from the large cold surface exposed by the bellows system. Both deficiencies are being corrected by the addition of a telescoping tube arrangement to confine the bellows motion and to insulate the bellows assembly from the interior ambient. Other improvements to the apparatus are also being considered. These include the addition of instrumentation to control the temperature and a liquid-nitrogen handling system to minimize loss of coolant fluid. (R. Y. Koyama)

B. Low-Temperature Processing of MOS Capacitors. Further studies have confirmed that the most satisfactory low-temperature process for fabricating MOS capacitors for TSM involves the chemical vapor deposition of silicon dioxide, 150 to 250 nm thick, at 400°C; electron-beam evaporation of aluminum, 400 to 600 nm thick; patterning; back-surface metallization; and microalloying in dry nitrogen for 20 min at 400°C (NBS Spec. Publ. 400-29, pp. 23-25).

Further work on tantalum pentoxide and anodically formed silicon dioxide dielectric films has been discontinued. Anodically formed films were found not to give reproducible results. A second lot of capacitors fabricated with tantalum pentoxide approximately 80 nm thick formed leaky capacitors similar in behavior to most of those in the first lot which were only about 35 nm thick.

(R. Y. Koyama and T. F. Leedy)

C. Process Monitoring. Although different manufacturers use different processes to fabricate thyristors, there appears to be a "basic" process which is common to the industry. Typical starting material for power thyristors is *n*-type, (111)-oriented, lapped silicon slices with resistivity in the range from 50 to 200 $\Omega \cdot \text{cm}$ and cut from a float-zoned crystal. For a given product device, the two most important requirements which the starting slices must meet are for resistivity and slice thickness. These parameters are critical to the reverse blocking voltage of the completed device.

Following appropriate chemical clean-up, the slice undergoes a closed-tube *p*-type diffusion at about 1250°C for 24 to 72 h to form

the deep junctions bounding the *n*-type region. At this stage, a *p-n-p* structure is formed, but the two junctions are shorted at the edge. As a result of this processing, the lifetime of the original *n*-type region has been degraded from several milliseconds to a few microseconds. Although the exact reason for this lifetime degradation is not known, heavy metal contamination from unknown sources is suspected. The time for this diffusion determines the final thickness of the interior *n*-type region; this thickness, along with the dopant density determines the reverse blocking characteristics of the device.

The next major processing step is the emitter diffusion, an open-tube *n*-type diffusion which forms the cathode region of the thyristor. The cathode configuration is defined photolithographically. At this point some form of lifetime control treatment is used to tailor the switching characteristic of the device. The tailoring can be completed at this stage or stopped short of completion in preparation for final adjustment to be made with electron irradiation just prior to packaging. The processed wafer is then bonded to a metal backing plate for rigidity and ease of handling in the packaging steps, and then the metallization for the gate and cathode is defined by evaporation through a transmission mask or photolithographically. The edge of the wafer-backing plate assembly is contoured to separate the junctions, and the junction edge is appropriately passivated to withstand the rated reverse blocking voltage. The resulting structure is illustrated in figure 9 together with a schematic indication of major processing stages. At this stage the switching characteristic is further adjusted, if necessary, and the packaging steps are carried out.

The most interesting points in this process for evaluation by TSM are immediately before the first diffusion, after the first diffusion, after the emitter diffusion, and after the lifetime-control step. To make TSM at these steps, appropriate test structures must be formed to provide electrical contact to the regions of interest. Prior to the first diffusion, the low-temperature MOS capacitor (see above) is the appropriate structure. Following the diffusion, there is a *p-n* junction, but the *n*-type region is not accessible unless a special test structure is used to provide the contact. This structure must provide the following:

- (1) contact to the *p*-type region;
- (2) contact to the *n*-type region;

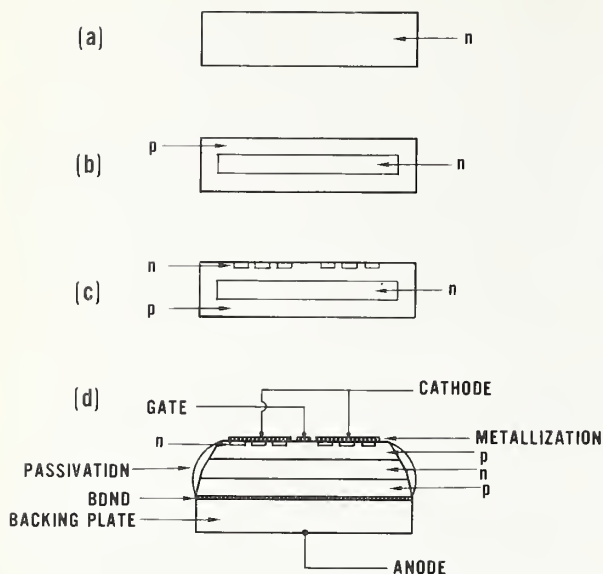


Figure 9. Typical thyristor structure. Shown schematically are (a) typical n -type slice starting material, (b) slice after p -type diffusion, (c) slice after n -type emitter diffusion, and (d) cross section of un-packaged device.

(3) definition and isolation of the $p-n$ junction, and

(4) passivation of the junction so that leakage currents are acceptably small.

Ideally, fabrication of the structure must be possible with low-temperature ($<400^\circ\text{C}$) steps. It must be possible to make the measurements in wafer form.

The structure, in its simplest form with front-surface contacts to both regions, is depicted in figure 10. The mesa diode is formed by chemical or physical etching, mechanical sawing, or a combination of techniques, and passivated with chemical-vapor-deposited silicon dioxide. It is likely that a doped-gold metallization or a lower resistivity diffused region may be required to form the contact to the high-resistivity n -type region. (R. Y. Koyama and M. G. Buehler)

3.7. Extended-Range MIS C(V) Method

Development and initial evaluation of the 25-kV system for measurements of capacitance and conductance as a function of voltage was completed. Separate reports have been prepared which describe the design and construc-

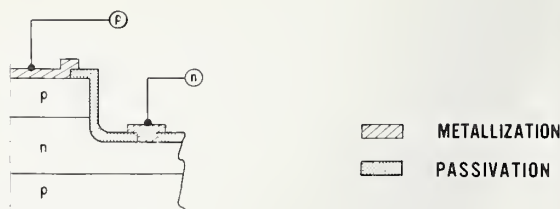


Figure 10. Cross section of mesa diode test structure.

tion details of the specimen holding system [39], the bias-protection circuit [40], and the linear-sweep, high-voltage supply [41]. This system permits application of the extended-range technique to metal-insulator-semiconductor (MIS) structures with insulator thickness in excess of 150 μm .

Among the objectives for the current phase of the work were improvement in the signal-to-noise ratio above that achievable with the initial 10-kV system and development of a guard-ring contact.

The increased signal-to-noise ratio was obtained through improvements incorporated in the new high-voltage power supply [41] and by increasing the magnitude of the 1-MHz test signal in the modified PAR 410 capacitance meter**[42] from 15 to 100 mV.^{††} These changes increased the signal-to-noise ratio by about two orders of magnitude. The improved signal-to-noise capability has been employed in all recent measurements made with the system.

A new test structure with a guarded electrode was evaluated. Guard-ring structures were defined on the free surface of the sapphire in three SOS specimens which previously had been used for measurement employing unguarded electrodes. Extended-range MIS C(V) measurements were then carried out on these specimens using the same bias-sweep conditions (range and sweep rate) as those used for the previous measurements. A comparison of some of the results is shown in table 4.

** See disclaimer, p. vi.

^{††} It is believed that a similar modification can be made to one of the other capacitance meters previously investigated (the Boonton 72B), but not to the third (the Boonton 71A).

MATERIALS CHARACTERIZATION BY ELECTRICAL METHODS

Table 4 - Capacitance Measurements on SOS Specimens Obtained with Guarded and Unguarded Electrodes

Specimen	Electrode Configuration	Insulator Capacitance, pF	Silicon Film		Interfacial Charge Density	
			Conductivity Type	Dopant Density, cm ⁻³	At Flat Band, cm ⁻²	At Weak Inversion Threshold, cm ⁻²
2463E	Unguarded	25.45	<i>n</i>	4.85×10^{15}	-6.5×10^{11}	-0.5×10^{11}
	Guarded	23.90	<i>n</i>	3.85×10^{15}	-6.2×10^{11}	-0.3×10^{11}
2523A	Unguarded	29.20	<i>p</i>	6.30×10^{15}	9.9×10^{11}	4.6×10^{11}
	Guarded	27.30	<i>p</i>	4.55×10^{15}	9.4×10^{11}	4.7×10^{11}
2523D	Unguarded	26.9	<i>p</i>	6.15×10^{15}	8.0×10^{11}	3.1×10^{11}
	Guarded	25.15	<i>p</i>	4.45×10^{15}	7.7×10^{11}	3.2×10^{11}

It is seen that the measured value of the insulator capacitance, C_I , is larger for the unguarded-electrode measurement, resulting in an overestimate of the dopant density of the silicon film for this measurement. The effect on the interfacial charge densities at flat-band, N_{FB} , and at the weak inversion threshold, N_{WI} , is relatively small and non-systematic. Qualitatively, the curves of $\Delta C(V)$ are slightly less "smeared out" when the guarded-electrode configuration is used, but the differences are not large.

(A. M. Goodman^{§§})

The extended-range MIS C(V) measurement technique has been used to study the dependence of the charge density at the silicon-sapphire interface of silicon on sapphire (SOS) as a function of (1) irradiation dose and (2) applied electric field in the sapphire. Results to date show that the radiation-induced

charge is always positive for either zero or positive voltage on the metal-gate electrode. Negative voltage applied to the metal-gate electrode ($E \gtrsim 2 \times 10^3$ V/cm) resulted in a negative radiation-induced charge. The functional dependences of the radiation-induced charge upon applied electric field are different for the positive and negative applied voltages. The observed behavior is not as yet understood [43].

(A. M. Goodman^{§§} and A. G. Kokkas^{¶¶})

The technique is also being used to study the effects of various sapphire substrate preparation techniques on the silicon-sapphire interfaces of SOS layers. Initial measurements indicate that the effects are (1) measurable and (2) likely to have a profound effect upon devices fabricated in these layers. This application will provide a valuable adjunct to the development of an optical test for the surface quality of sapphire (see sec. 4.5.).

(A. M. Goodman^{§§} and C. E. Weitzel^{§§})

^{§§}Work performed at RCA Laboratories under NBS Contract No. 5-35912. NBS contact for additional information: R. Y. Koyama.

^{¶¶}Work performed at RCA Laboratories under Contract No. F19628-76-C-0183, Rome Air Development Center, Deputy for Electronic Technology, Hanscom AFB, MA 01731.

4. MATERIALS CHARACTERIZATION BY PHYSICAL ANALYSIS METHODS

4.1. Calibration Standards for Ion Microprobe Mass Analysis

This task was undertaken to develop methods for preparation of standard specimens for empirically calibrating an ion microprobe mass analyzer (IMMA) so that quantitative measurements can be made of selected impurities in silicon and silicon dioxide regions of semiconductor devices. Implicit in this objective is the evaluation of the applicability of the IMMA for this type of analysis and the determination of the instrumental parameters best suited for these analyses. Ion implantation was chosen as the most appropriate method for preparation of the specimens (NBS Spec. Publ. 400-19, pp. 20-22) because of the inherent ability of this method to implant specific impurities at specific depths at selected concentrations. The standard specimens thereby simulate actual device structural layers and exploit the in-depth profiling capability of the IMMA. The versatility of ion implantation impurity selection makes it possible (dependent on the ion implantation equipment) to produce standard specimens for virtually every element in the periodic table.

Analysis of the silicon specimens implanted with phosphorus has been completed. These specimens were implanted with 80-keV ^{31}P to nominal doses of 10^{13} , 10^{14} , 10^{15} , or 10^{16} cm^{-2} or with 60- or 100-keV ^{31}P to a nominal dose of 10^{16} cm^{-2} . The specimens were analyzed using neutron activation analysis and then were in-depth profiled using the IMMA. The reproducibility of both the sputter rate and the calibration coefficient was examined in some detail.

Neutron Activation Analysis — Implant doses were determined by neutron activation analysis using the unpatterned half of the implanted wafer. The half wafers as received from microvolume fabrication were loaded into a high-purity quartz dish with an inside diameter of 2-1/8 in. (54 mm). High-resistivity boron-doped silicon wafers were used as spacers between each half wafer and on the top and bottom of the stack. These spacers completely fill the inside diameter of the dish. They are routinely cleaned and etched before each irradiation. The same spacers have been used for more than four years in over 50 irradiations; they do not appear to be a source of contamination. Three separately weighed phosphorus monitors, each sealed in its own high-purity quartz ampoule, were also placed

in the dish. A quartz top was attached using pressure-sensitive tape, and the dish was sealed in an aluminum can for the irradiation which was carried out for 14 h at a nominal neutron flux of $1 \times 10^{13} \text{ cm}^{-2} \cdot \text{s}^{-1}$ in the Texas A&M reactor.

After irradiation, the aluminum can was opened and discarded. The half wafers were removed from the quartz dish and cleaned three times in a mixture of hydrochloric acid and methanol, rinsed in acetone, and dried in air. The wafers were then placed on x-ray film to check the dopant uniformity by autoradiography.

Using the autoradiogram as a guide, a uniformly implanted region was scribed from each wafer and this specimen mounted in an aluminum planchet [44] for beta counting. Normally, the specimen consisted of the entire half wafer except for those portions of the corners that would not fit into the planchet. Prior to scribing, the mass of each wafer to be counted was determined with an analytical balance, and the wafer thickness was measured with a micrometer. A surface area was calculated using 2.32 g/cm^3 as the density of silicon.

The planchets containing the half wafers were loaded into holders for counting. The counting sequence included three background specimens (filter paper on planchets) at the beginning, end, and middle, as well as nine monitor specimens (aliquots of monitors carried by filter paper on planchets) evenly distributed among the half-wafer specimens. All specimens were counted for the shorter of 50 min or 2×10^4 preset counts with the beta plateau adjusted for ^{32}P . The counter was operated in the net mode with a discriminator set for elimination of electronic noise. The background count rate averaged $4.34 \pm 0.58 \text{ cpm}$, where the uncertainty is 1.96 standard deviations from the mean for multiple determinations of 50 min each.

Two different chemical compounds were tested as phosphorus monitors, ammonium phosphate (26.927-percent phosphorus) and diammonium phosphate (23.455-percent phosphorus). A matrix of three weighings of each compound was packed, irradiated, and processed following the standard procedure for monitors. No difference between these compounds in either the specific activity or the standard deviation from the mean specific activity was observed

in a comparison test. The compound diammonium phosphate was chosen for routine work because of the ease in handling its small crystals for determinations of mass. No mass loss was observed for this compound after 6 h in a vacuum oven at 100°C.

The ampoules containing monitors were cleaned in aqua regia and deionized water. They were then cracked in clean beakers, and the monitor was dissolved in deionized water. For each monitor, the solution and three subsequent rinses were transferred to a 10-mL volumetric flask and deionized water added to bring the flask contents to volume. Three aliquots (typically 100 µL) were taken from each flask and mounted in planchets on filter paper. The mounting procedure is designed to approximate the counting geometry of the silicon wafers as closely as possible. Tests in which phosphorus in silicon dioxide was counted in wafer form and then as a solution indicated that there is no measurable mismatch in counting geometry. Reproducibility in pipetting monitors was checked by beta counting aliquots of the monitor solution. Reproducibility between 1 and 2 percent at the 95-percent confidence level was generally achieved.

Specimens were allowed to decay for 10 to 12 days after irradiation before beta counting. Thereafter, they were counted at 60- to 72-h intervals over a period of 20 or more days. The elapsed time for each counting of a set of specimens (backgrounds, monitors, and half wafers) was typically 8 h and rarely exceeded 12 h, even after long decay periods.

Phosphorus counts from both the monitors and wafers were corrected for background and decay ($t_{\frac{1}{2}} = 14.4$ days), and the total number of phosphorus atoms in each wafer was calculated directly using the specific activity of the monitors. The constancy of the total number of atoms for a wafer as a function of decay time is confirmation that the correct half-life value is being used, since this value is proportional to the ratio of beta activity from the monitors and a wafer. A long-lived component in some low-dose implants was identified as ^{51}Cr by half-life measurements and gamma-ray spectroscopy. Phosphorus results were determined for these wafers when the decay curve could be resolved graphically into components of 27.7 days and 14.4 days.

Investigations of sources of error were aimed principally at determining reproducibility of a determination from a single irradiation; reproducibility between irradiations was not in-

vestigated. In summary, all factors considered proved to be small compared to the standard deviations for the mean number of atoms per wafer (typically less than 1 percent) and the mean specific activity determined from the monitors (typically 3 to 5 percent). The uncertainty of the determination of implant doses was estimated by summing the variances from these two means.

Sputtering Rate — The sputtering rate in an ion microprobe is a critical parameter both during calibration and during subsequent application as an analytical tool. In work reported here, it was assumed that the sputtering rate remained constant during each analysis. The question of reproducibility between analyses was examined for the case where the IMMA was operated with a nominal raster size of 125 µm by 100 µm, a beam current between 18 and 30 nA, inclusive, and a 19.4-keV O_2^+ beam. Since the specimens were held at a potential of +1.5 kV, the energy per incident oxygen atom in this case was approximately 9 keV. The implanted silicon slices were sputtered for long times to obtain in-depth profiles of counts per sputtering interval (channel) vs. channel number. Crater depth, crater area, beam current, and sputtering time were measured, and both the actual sputtering rate and the sputtering rate normalized to unit current density were calculated. The results are given in table 5. It is estimated that the crater depth can be determined (with the microscope) to ± 10 percent and the crater area (also with the microscope) to ± 20 percent. The beam current was read to the nearest nanoampere. As can be seen from the data in table 5, the relative sample standard deviation (coefficient of variation) of the measured crater area was 7.7 percent; the relative sample standard deviation of the normalized sputtering rate was 11 percent.

Calibration Coefficient — Two data analysis techniques can conveniently be used to obtain calibration curves of phosphorus density as a function of signal. In one method, the signal is taken as the ratio of the phosphorus counts in one channel of the profile to the silicon counts in the same channel; in the present work only the peak channel was used. In the second method, the signal is taken as the ratio of the sum of the phosphorus counts over a substantial fraction of the profile to the sum of the silicon counts over the same region of the profile. Although the silicon signal is typically flat over the region of integration, normalization of the phosphorus to the silicon counts is intended

MATERIALS CHARACTERIZATION BY PHYSICAL ANALYSIS METHODS

Table 5 - Normalized Sputtering Rate of an Ion Microprobe Mass Analyzer Operated with a 19.4-keV O₂⁺ Beam and a Nominal Raster Size of 125 μm by 100 μm

Specimen	Sputtering Time, s	Crater Depth, nm	Sputtering Rate, nm/s	Beam Current, nA	Crater Area, μm ²	Normalized Sputtering Rate, nm·μm ² /nA·s
1	2640	532	0.20	29	15730	109
2	2816	602	0.21	29	13030	96
3	2442	465	0.19	28	14200	97
4	2684	461	0.17	30	12800	73
5	2684	567	0.21	30	11370	80
6	2442	314	0.13	18	13890	99
7	2420	368	0.15	21	11810	85
8	2794	324	0.12	18	13890	89
9	2794	355	0.13	18	13310	94
10	2024	290	0.14	18	13310	106
11	2420	273	0.11	19	13310	79
12	3498	426	0.12	19	13530	87
13	3366	450	0.13	20	13390	90
14	3498	465	0.13	20	13900	92
Mean			0.15		13390	91
Sample Std. Dev.			0.04		1040	10
Coef. of Var.			23%		7.7%	11%

to circumvent variations in sputter-detection efficiency which can be caused by fluctuations in a myriad of machine and sample parameters. The second, or integral ratio, method was used to obtain the results discussed below.

The shape of the in-depth phosphorus distribution for the ion implantations was observed to be approximately Gaussian. Consequently, a pseudo-Gaussian approximation was employed in mathematical modeling; the assumption that the profile shape can be approximated by a Gaussian makes it possible to select limits of integration for both the number of atoms and the signal (counts) which encompass a known fraction of the area under the curve. For a Gaussian, the standard deviation, σ , is related to the full width at half maximum (FWHM):

$$\sigma = \text{FWHM}/2.35.$$

The center of the profile was taken as the center point of the FWHM. To minimize round-off errors which arise because of the repre-

sentation of the profile as a histogram, the integration was carried out over 90 percent of the pseudo-Gaussian ($\pm 1.68\sigma$). Thus, the contents of the "limit channels" were usually small compared to the sum. Round-off in selecting the limit channels had a small impact on the resultant integral. The ratio between sputtering rate and multiscaling dwell time has a sharp impact on the precision of this method; errors in integration are enhanced when too few channels define a peak. The trade-off between a sufficient number of points to define a profile shape and the statistical significance of each point is a familiar problem in nuclear spectroscopy.

The background under the profile peak can cause problems in analysis when the signal-to-background ratio is low. The origin of tailing on the "deep side" of the profile is complex. Possible contributing factors include neutral beam sputtering of a high phosphorus concentration outside the raster area, channeling during implantation, contributions from the crater wall during sputtering, traces of water in the vacuum system near

MATERIALS CHARACTERIZATION BY PHYSICAL ANALYSIS METHODS

Table 6 - Calibration Data for Ion Microprobe Mass Analysis of Phosphorus-Doped Silicon Based on Integral Ratio Method

Specimen ^a	Implanted Phosphorus Dose, cm^{-2}	Beam Current, nA	IMMA Signal	Number of Channels	Average Phosphorus Density, cm^{-3}	Calibration Coefficient, cm^{-3}
80-16	1.23×10^{16}	30	0.021	34	6.8×10^{20}	3.24×10^{22}
		28	0.026	35	7.1×10^{20}	2.73×10^{22}
		30	0.038	35	6.6×10^{20}	1.74×10^{22}
		30	0.043	34	6.8×10^{20}	1.58×10^{22}
		30	0.029	35	6.6×10^{20}	2.28×10^{22}
80-15	1.27×10^{15}	30	0.0032	40	0.59×10^{20}	1.84×10^{22}
		34	0.0033	35	0.60×10^{20}	1.82×10^{22}
		32	0.0029	40	0.56×10^{20}	1.93×10^{22}
		32	0.0030	39	0.57×10^{20}	1.90×10^{22}
		32	0.0027	40	0.56×10^{20}	2.07×10^{22}
100-16	1.17×10^{16}	32	0.021	47	0.44×10^{20}	2.10×10^{22}
		32	0.021	49	0.42×10^{20}	2.00×10^{22}
		30	0.020	52	0.42×10^{20}	2.10×10^{22}
		30	0.023	49	0.45×10^{20}	1.96×10^{22}
60-16	1.17×10^{16}	24	0.030	26	10.5×10^{20}	3.50×10^{22}
		22	0.032	31	9.6×10^{20}	3.00×10^{22}
		24	0.033	29	9.5×10^{20}	2.88×10^{22}
		19	0.034	37	9.4×10^{20}	2.76×10^{22}

^aThe left-hand number in the specimen designation represents the implantation energy in kilovolts; the right-hand number represents the order of the nominal implant dose.

the specimen, knock-on during sputtering or implantation or both, and SiH^+ (mass 31) background. For implantation doses of 10^{15} or 10^{16} cm^{-2} the background was small enough to be ignored over the integration range of $\pm 1.68\sigma$; data on specimens with lower implantation doses were not included in the present analysis. Results of 18 profile measurements made on four slices are summarized in table 6. All analyses were performed on 760- μm by 760- μm microvolumes (NBS Spec. Publ. 400-19, pp. 20-22) with a nominal raster size of 125 μm by 100 μm ; similar results were obtained on "infinite" planes. The specimens analyzed are identified in column 1 of the table. The implanted phosphorus dose, as determined by neutron activation analysis, is given in column 2. The beam current is given in column 3; variations in beam current over the range employed were not expected to affect the re-

sults. The signal, S, given in column 4 is the ratio of the sum of the phosphorus counts to the sum of the silicon counts from the number of channels, indicated in column 5, over which the profile was integrated. The sputtering time, in seconds, was 22 times the number of channels. The average phosphorus density, given in column 6, was obtained by dividing 90 percent of the implanted dose (column 2) by the crater depth which was found from the mean normalized sputtering rate (table 5), the beam current (column 3), the nominal raster area, and the sputtering time. The calibration coefficient, the ratio of the average phosphorus density to the signal, is given in column 7; this coefficient is expected to be constant if a linear relationship exists between the signal and the phosphorus density.

The deviations from the mean were shown to be random by an analysis of residuals. The relative sample standard deviation of the calibration coefficient for these 18 analyses made over a period of several months was 25 percent; this is a measure of the long-term reproducibility of the IMMA when measuring phosphorus in silicon.

Other Impurities — Specimens of phosphorus implanted in silicon dioxide and arsenic, sodium, antimony, and gold in both silicon and silicon dioxide have been prepared and both neutron activation and ion microprobe mass analyses are underway.

(R. Dobrott^{*} and G. B. Larrabee^{*})

4.2. Electron Spectroscopy Techniques

Ion-Beam Rastering — In order to achieve a large ion current density ($>40 \mu\text{A}/\text{cm}^2$) uniform to better than 0.5 percent over a square of edge 250 μm (the size of the scanned electron beam), it is necessary to raster the ion beam which is employed to sputter-etch the crater in carrying out depth profiling measurements with Auger electron spectroscopy (AES). The unrastered beam has an FWHM of about 3 mm. With typical rastering, this is broadened by a factor of from 1.2 to 2.5. The beam maximum may, however, undergo a shift in position on rastering if the beam is initially asymmetric, because the beam raster is of the same order as the beam dimensions. In addition, the voltages applied to the deflection plates must be strictly of triangular waveshape. If the waveform is at all rounded, more time is spent in some regions than others, and it is possible with large scans to obtain craters which are deeper at the edges than at the center. Measurements of these effects were made, and an alignment technique was developed to avoid the effects of beam asymmetry.

The alignment technique consists of the following procedure:

(1) Allow the ion gun to come to thermal equilibrium at the emission current to be used by running it in the absence of both argon and beam voltage for at least 30 min prior to beginning profiling. In addition, run the gun for 15 min under operating conditions while the ion current density is measured using a Faraday cup.

(2) Position the Faraday cup at the focal point of the analyzer and focus and deflect the unrastered ion beam for a maximum current into the cup.

(3) Measure the profile of the rastered beam in two directions, one parallel to the axis of the cylindrical mirror analyzer (CMA) and the other perpendicular to this axis, taking current readings as a function of micrometer setting. If the distribution is not centered, adjust the deflection to center the distribution at the analyzer focal point. The ion gun controls and electron gun deflection controls are then held constant for a series of comparative profiles. Before and after these profiles are made, the ion-beam current density is checked by bringing the Faraday cup to the focal point of the analyzer using the scanning sample positioner and the 2000-eV elastic peak. The former positions the aperture on the axis of the analyzer; the positioning adjustment along the CMA axis can be made with the aid of the latter.

(W. E. Spicer[†], N. J. Taylor[§], and Y. E. Strausser[§])

Ion-Stimulated Auger Transitions — Measurements of ion-stimulated Auger (ISA) emission (NBS Spec. Publ. 400-25, p. 17) have been completed to the point of defining the possible interferences which this process might produce in profiling work. ISA emission has a very strong primary ion energy dependence which leads to problems with 3-keV argon-ion bombardment of either aluminum or silicon but produces negligible interferences at a primary ion energy of 1 keV. Fortunately, it has been found on other grounds that the use of ion energies near 1 keV produces the best depth resolution in the SiO_x/Si system (NBS Spec. Publ. 400-25, pp. 16-17).

The ISA electrons are produced in $\text{L}_{2,3}^{\text{VV}}$ transitions in silicon and aluminum. There are no ISA KLL transitions in either silicon or aluminum; therefore, these transitions give good profiling data even at 3-keV ion energy. ISA emission has also been observed from silicon dioxide and alumina, although

^{*}Work performed at the Central Research Laboratories of Texas Instruments Incorporated under NBS Contract No. 5-35917. NBS contact for additional information: K. F. Galloway.

[†]Work performed at Stanford Electronics Laboratories of Stanford University under NBS Contract No. 5-35944. NBS contact for additional information: K. F. Galloway.

[§]Work performed at the Surface Analysis Laboratory of Varian Vacuum Division under subcontract to Stanford University.

the yield is greatly reduced from that in the spectra of pure silicon and aluminum. The characteristics of the ISA spectra, such as line shapes, lead to the speculation that the ISA electrons originate from single ions or small clusters leaving the specimen surface.

(W. E. Spicer[†],

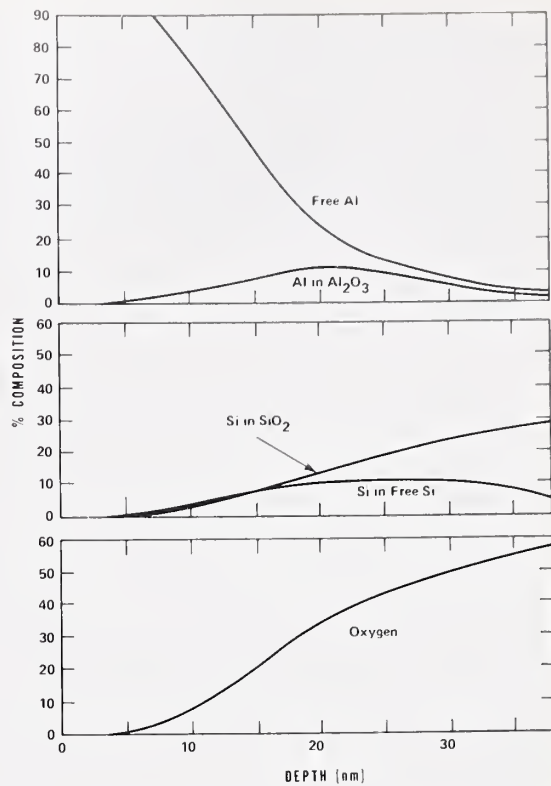
N. J. Taylor[§], and Y. E. Strausser[§])

Profiling of Metal-Silicon Dioxide Interfaces — Preliminary AES measurements have been made on interfaces between sputtered pure or doped aluminum metal films and thermally grown silicon dioxide. In the case of pure aluminum, the primary interest was in the solid-state reactions which might occur with the aluminum reducing the silicon dioxide to form alumina and silicon. This reaction did occur; a typical profile measurement, illustrated in figure 11a, exhibited a surprisingly broad interface. Measurements on such films following post-deposition annealing showed results similar to those of measurements on films without post-deposition annealing.

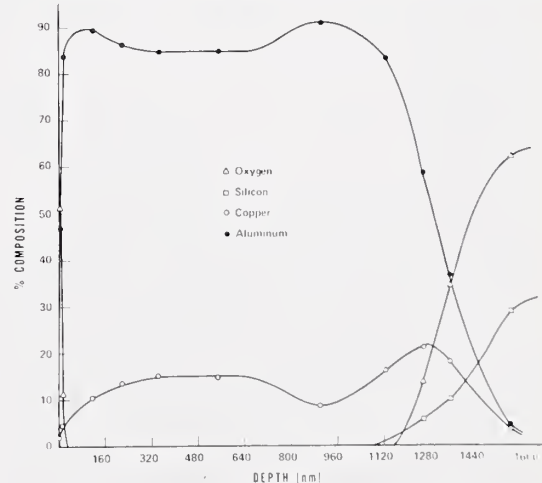
In the measurement of sputter-deposited aluminum films doped with 6-percent copper, the interesting result is the distribution of the copper through the film; a typical result is shown in figure 11b. This double peaking with the majority of the copper sitting near the silicon dioxide has been measured in films produced at different times and in measurements with significant differences in the profiling conditions, but at present there is no explanation for the observed segregation effects.

(Y. E. Strausser[§],
P. E. Luscher[§], and J. S. Johannessen^{†¶})

Limitations on Interface Width Resolution in Auger-Sputter Profiling — Although numerous effects that cause broadening of an interface during Auger-sputter profiling can be reduced to negligible levels by selecting appropriate measurement conditions [45], two broadening effects inherent in the technique remain:



- a. Profile through interfacial region between aluminum and silicon dioxide films.



- b. Profile through copper-doped aluminum film on silicon dioxide. A 200-nm thick portion of the film was doped with 4-percent copper and 2-percent silicon; the remainder of the film was doped with 6-percent copper.

Figure 11. Composition profiles of metal-silicon dioxide interfaces by Auger-sputter techniques.

[†]Work performed at Stanford Electronics Laboratories of Stanford University under NBS Contract No. 5-35944. NBS contact for additional information: K. F. Galloway.

[§]Work performed at the Surface Analysis Laboratory of Varian Vacuum Division under subcontract to Stanford University.

[¶]Partially supported by Electronics Research Laboratory, University of Trondheim and the Royal Norwegian Council for Scientific and Industrial Research.

electron escape depth and ion knock-on mixing. Initial efforts have been concentrated on the electron escape-depth problem.

Consider an interface profile given by a function, $f(x)$; at a distance, d , away from the interface, the emission strength of a transition is given by the convolution of $f(x)$ with the escape-depth function:

$$\frac{1}{L} \int_0^{\infty} e^{-x'/L} f(x'-d) dx' = \frac{e^{-d/L}}{L} \int_{-d}^{\infty} e^{-x/L} f(x) dx . \quad (26)$$

As an example, consider the case where

$$f(x) = 0 \text{ for } x < 0, \text{ and}$$

$$f(x) = 1 \text{ for } x > 0,$$

shown in figure 12 as the solid curve. For $d > 0$, the interface [which is defined as the point a , where $f(a) = 0.5$] has not yet been reached, and eq (26) reduces to

$$\frac{e^{-d/L}}{L} \int_0^{\infty} e^{-x/L} dx = e^{-d/L} . \quad (26a)$$

For $d < 0$ the interface has been passed, and eq (26) reduces to

$$\frac{e^{-d/L}}{L} \int_{-d}^{\infty} e^{-x/L} dx = 1 . \quad (26b)$$

The measured interface profile, as given by eqs (26a) and (26b) is shown in figure 12 as the dashed curve. The measured interface position is given by $d = L \ln 2 = 0.7 L$ closer to the surface than the actual interface, so that for transitions of different escape depth the measured interface position is not identical. If the measured interface width, W_M , is defined as that thickness for which the signal strength rises from 10 to 90 percent of its maximum value, W_M can be found from eq (26a):

$$W_M = L \{ \ln 10 - \ln 1.11 \} = 2.2L . \quad (27)$$

In the case of silicon and oxygen, the escape depths have been estimated to be 0.5 nm for the silicon LVV transition, 1 nm for the oxygen KLL transition, and 3 nm for the silicon KLL transition. For the silicon LVV transition, the minimum broadening of a step

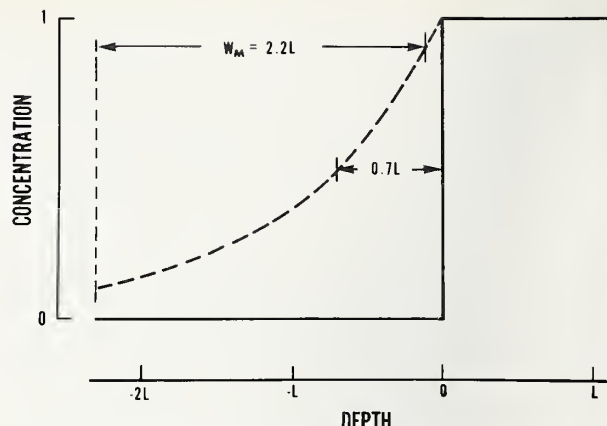


Figure 12. Broadening of a step interface resulting from the effects of electron escape depth.

interface is 1.1 nm. Since the measured interface width is a convolution of the escape depth with the actual profile, the broadening of an interface with finite real width is not additive but behaves more nearly as an rms average. For example, an interface 1.0 nm wide would appear to be about 1.5 nm wide when measured with the silicon LVV transition.

The calculated shift in the interface position due to escape depth as indicated in eq (27) provides a means for determining the actual interface position. In this analysis, however, the effects of sputter knock-on mixing have been neglected. This process alters the actual interface profile, so that $f(x)$ is a more complex function with dependence on the argon ion range and the distance between the surface and the interface. A quantitative formulation similar to eq (26) which includes both the effects of electron escape depth and ion knock-on mixing is under development. Ideally, this will allow a deconvolution of the real interface profile from the measured one.

(C. R. Helms[†] and W. E. Spicer[†])

Auger-Sputter Profiling of MOS Oxides — Work has been undertaken to investigate the relationships between the microscopic properties (such as width and stoichiometry) of silicon-silicon dioxide interfaces, the electrical characteristics of the interfaces, and the methods of preparing oxide films. Initial efforts are being concentrated on measuring the

[†]Work performed at Stanford Electronics Laboratories of Stanford University under NBS Contract No. 5-35944. NBS contact for additional information: K. F. Galloway.

Table 7 - Preliminary Results of Auger-Sputter Profiling Measurements on CVD and Dry Thermal Oxides

Specimen	Interface Width, nm				Sputtering Rate, nm·cm ² /min·μA
	From Oxygen KLL Transition		From Silicon LVV Transition		
	Measured	Corrected	Measured	Corrected	
Average dry thermal oxide	3.3 ± 0.3	2.5 ± 0.5	2.5 ± 0.3	2.25 ± 0.35	0.11 ± 0.005
CVD oxide without anneal	5.5	5.0	4.1	4.0	0.145
CVD oxide with anneal	5.35	4.9	4.5	4.4	0.121

microscopic properties of silicon-silicon dioxide interfaces with interface state density (as determined by capacitance-voltage measurements [46]) in the range from 10^{10} to 10^{12} cm⁻². Oxides prepared in four ways are being investigated: dry thermal oxidation, steam thermal oxidation, chemical vapor deposition (CVD), and vacuum evaporation. Growth or deposition time and temperature are being varied in the study, but post-growth processing is being held to a minimum in order to avoid additional complications from other processing steps.

Preliminary results on oxides prepared[#] by CVD are compared in table 7 with the properties of oxides thermally grown[#] in dry oxygen. The interface width was measured between the 10-percent and 90-percent values of the Auger signal. A correction for electron escape depth was applied as discussed above to obtain the corrected width. The values for the "average dry thermal oxide" were obtained by averaging runs for a number of different specimens. These results indicate that the CVD oxide-silicon interfaces are 2 to 2.5 nm wider than the interface in a "good" thermal oxide. The bulk of these oxides also appears to have higher density as can be seen from the higher sputtering rates obtained for them. Following the anneal, the interface state density of the CVD oxide was approximately one order of magnitude higher than that of a good thermal oxide. A meaningful value of surface state density could not be obtained for the CVD oxide without anneal because the C-V curve was very broad, indicative of the much poorer electrical characteristics of this oxide.

(C. R. Helms[†] and W. E. Spicer[†])

4.3. Techniques for Chemical Diagnostics in Semiconductor Processing

This task was undertaken to evaluate the application of x-ray photoelectron spectroscopy (XPS)^x to diagnostic measurements in semiconductor device processing and to establish and document appropriate methods for specimen preparation and data collection, analysis, and interpretation. The work is being carried out at the Surface Analysis Facility of the Jet Propulsion Laboratory [46]. This facility has been organized to provide as broad a spectrum of surface data as could be integrated into one experimental system. Although the emphasis is on XPS, the facility also includes instrumentation for Auger electron spectroscopy (AES), a scanning low-energy electron probe (SLEEP), secondary ion mass spectroscopy (SIMS), and ion scattering spectroscopy (ISS), and various chambers for specimen preparation, wet chemistry, plasma cleaning, and *in situ* oxidation.

The electron methods chamber is based on a modified HP 5950A ESCA spectrometer[†] with a

[#]These oxide films were grown and electrically characterized by Dr. Noble Johnson at Xerox Palo Alto Research Laboratories who also performed the ellipsometric measurements from which the sputtering rates were determined.

[†]Work performed at Stanford Electronics Laboratories of Stanford University under NBS Contract No. 5-35944. NBS contact for additional information: K. F. Galloway.

^xAlso known as Electron Spectroscopy for Chemical Analysis (ESCA).

[†]See disclaimer, p. vi.

monochromatic aluminum K α x-ray source. The electron kinetic energy analyzer is a fixed-energy 180-deg hemispherical electron monochromator with a retarding-potential lens system for scanning the electron energy spectrum. The detector system uses a channel-plate electron multiplier with phosphor and a vidicon for data readout. The use of the monochromatic source and high-resolution spectrometer results in narrower line widths and consequently more chemical information. However, the enhanced signal-to-background ratio for the monochromatic system (400 to 800:1) as compared to the standard source (7 to 10:1) is even more important for the study of low-level impurities in the silicon-silicon dioxide system. For application to the study of the silicon-silicon dioxide interface, it was necessary to determine the escape depth of photoelectrons in silicon dioxide. This escape depth for silicon 2p photoelectrons was determined to be about 4.2 nm; therefore, XPS can be used to study interfaces under 4 to 10 nm of silicon dioxide.

Determination of Binding Energies — The interaction of electrons, ions, and photons with the silicon-silicon dioxide system was studied, and both electron- and ion-stimulated decomposition were observed. Serious difficulties were encountered because of charging effects. Silicon dioxide specimens tended to build up large positive charges on the surface after x-irradiation. This resulted in a binding energy uncertainty greater than or equal to the chemical shift. In order to stabilize these measurements, an interactive SLEEP system for referencing spectra to the vacuum level was developed to permit direct measurement of surface potentials and therefore make possible a series of bias-controlled experiments. These experiments demonstrated the existence of several chemical states of sodium which are involved in trapping at the silicon-silicon dioxide interface [48]. The importance of surface potential control was also demonstrated in differential charging experiments. Several specimens were prepared with a thin surface oxide covering a highly conductive layered substrate. Peaks in the XPS spectrum were observed from the oxide region as well as the substrate. The oxide peaks showed a strong charging shift to high binding energy, which was a function of the electron flux density to the surface. The substrate peaks showed no such effect. Consequently, the recorded spectrum varied markedly as a function of secondary electron flux. Such physical charge differences could be misinterpreted as chemical shift variations. To improve the

capability of determining binding energies in terms of a known potential, considerable effort was directed toward decreasing the size of the interrogating electron spot in the SLEEP experiment. The original implementation of this system employed an electron gun from a commercial vidicon, the gun being electrostatically focused and deflected. This gun was modified in two ways: 1) a 100- μ m diameter aperture was substituted for the 1-mm diameter aperture in the original gun, and 2) a ground-plane extension tube was fabricated onto the end of the gun to bring the ground plane as close as possible to the specimen surface. The first modification resulted in smaller beam diameters and lower current densities, both of which are desirable in the present application. The second modification seems to have significantly reduced surface patch effects on the irradiated portion of the insulator.

Preliminary results with the modified gun indicate that 1) peak positions can be stabilized to ± 0.2 eV with little difficulty, 2) line widths of observed peaks (for insulators) can be reduced significantly by minimizing the surface potential distribution over the specimen, and 3) the surface of an insulator charges to a limiting value and then discharges in a time scale of milliseconds. This last behavior seems to be related to patch effects on the surface and results in a 2- to 4-eV peak-to-peak contribution to the line shape.

Interface Studies — Studies of the silicon-silicon dioxide interface involve two fundamentally different experimental procedures: 1) grow oxides thicker than 10 nm and etch back (by ion milling or wet chemistry) to the interface while studying changes in silicon and oxygen chemistry or silicon-oxygen ratios, or 2) grow very thin oxides (1 to 10 nm thick) and follow chemical changes as a function of increasing thickness. The object of both of these approaches is to determine the chemical structure of the interface and boundary oxide. This understanding, together with a study of how contaminants affect the interface region, is a key prerequisite for the control of electrical characteristics of MOS devices.

It has been observed previously that cleaning procedures used in silicon wafer processing do not remove organic surface contamination [49]. To study the effect of residual carbon on the interface state density, pairs of silicon wafers were cleaned by a variety of procedures and, without removing them from the analysis facility, oxidized in dry oxygen

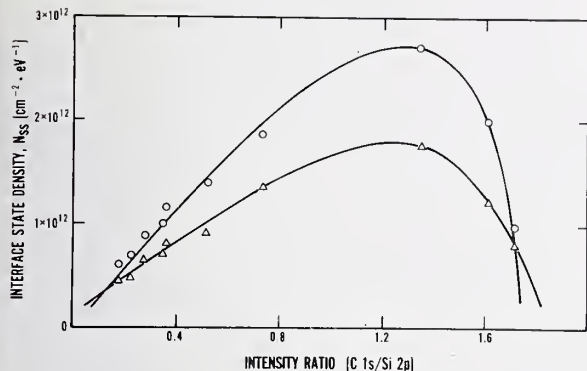


Figure 13. Interface state density, N_{ss} , as a function of carbon concentration at the interface. (The carbon concentration is expressed as the intensity ratio of the 1s photopeak of carbon at 0.7 eV (O) or 0.55 eV (Δ) to the 2p photopeak of silicon.)

at 800°C to produce a 6-nm thick oxide. On one wafer from each pair the intensity of the carbon 1s XPS peak was measured. The other wafer of each pair was metallized with aluminum by a shadow-mask procedure, and the interface state density was determined by means of capacitance-voltage measurements. Several pairs of wafers were held in a nitrogen-filled dry box until XPS could detect no species other than silicon. One of these pairs was directly oxidized and measured; several others were intentionally contaminated with controlled amounts of well-defined organic chemicals before oxidation. Six pairs were cleaned using six different cleaning recipes just prior to oxidation. These cleaning procedures resulted in differing amounts of carbon contamination at the interface, as determined by the carbon 1s photoelectron peak intensities.

The relationship between interface state density and the carbon 1s intensity (normalized to the silicon 2p intensity) is shown in figure 13. There are three regions of behavior. The initial region shows a rise in interface state density with increasing carbon 1s intensity. This is followed by a region over which interface state density is not strongly dependent on carbon 1s intensity. At still higher values of carbon 1s intensity, the interface state density decreases sharply. The carbon signal strength was also measured for these specimens before oxidation. There was no correlation of interface state density with the carbon intensities before oxidation.

In addition, several wafers were coated with the same thickness of organic compound (1 nm), and the carbon intensity was monitored as a function of final oxide film thickness. Initially, a rapid change in the carbon spectrum was interpreted as evidence of both oxidized and reduced species. There was a 10- to 20-percent loss of carbon at the beginning. No further change was observed in amount of carbon after formation of a silicon dioxide film 1.5 to 2.0 nm thick. The ratio of oxidized to reduced carbon stabilized after approximately 6 nm of silicon dioxide had been grown.

From these results, it is tentatively concluded that different chemical forms of carbon added at the silicon surface show different retention ratios after oxidation. The final amount and chemical state of carbon at the interface significantly affect the interface state density. Additional experiments designed to establish the mechanism of the effect are now under way.

Data Reduction Procedures — A significant part of the work was devoted to examination of data-reduction algorithms. Approximately 40 different methods have been described in various elements of the periodical literature. These methods have all been reduced to algorithms and implemented in a computer program. This program was used to study the effects of methods of noise removal and deconvolution on simulated test spectra with signal and noise characteristics virtually identical to those observed in XPS and AES. These spectra consisted of 2:1 intensity-ratio Lorentzian doublets which have a peak splitting larger than the natural line width and which are convolved with an asymmetric Gaussian instrument function. Asymmetry was introduced because of the severe complications this adds to the problem and because instrument functions in electron optics are asymmetric. For example, a 2:1 doublet with a full width at half maximum of 0.1 eV, split by 0.6 eV closely approximates the natural 2p photoelectron spectrum of silicon. A typical instrument function width was chosen as 0.6 eV. A series of test spectra was prepared with signal-to-noise ratios varying from 1000:1 to 0.001:1. Two types of noise were employed: Gaussian and experimental; the latter was stripped from a large sample of XPS spectra and included a significant 1/f component.

In order to evaluate the methods, two criteria were chosen: 1) magnitude of the residuals and 2) mean square error. All the meth-

ods were reduced by means of linear algebra into a common form and it was determined that all deconvolution methods could be reduced to two variations. It was observed that the differences between published algorithms are generally manifested in the way the noise terms are manipulated. Virtually all iterative deconvolution routines employ a minimization of residuals as a criterion for convergence. Large changes were observed among the various methods in the magnitude of the final residuals but there was little observable effect on the magnitude of the mean square error.

A publication is being prepared [50] in which existing methods are evaluated and a number of algorithms are developed which give varying degrees of recovery of original information. Similar algorithms are being developed to treat the problem of recovering signal from noise with explicit recognition of the implications of the compromises made.

A major difficulty in applying such methods is that of characterizing the instrument function, the basic signal, and the noise component. In the course of this research a number of algorithms have been developed; these results and the methods used to obtain them will be the subject of a later publication.

(F. J. Grunthaner^{**})

4.4. Nuclear-Track Technique

Neutron activation analysis [44,51] is a useful technique for determining total densities at trace levels of most impurities in silicon. However, boron cannot be detected by conventional neutron activation analysis. Therefore, alternative methods are necessary for measurement of total boron density. The nuclear-track technique had previously been used to detect trace concentrations of boron in glass [52]. Work was begun to evaluate the applicability of this method to the determination of boron density in silicon slices.

The analysis for boron in silicon by the nuclear-track technique is based on the number of radiation-damaged areas produced in a dielectric material in contact with the silicon. These radiation-damaged areas are a result of the predominantly 1.44-MeV alpha particles that are produced during thermal neutron bombardment of the boron by the reaction $^{10}\text{B}(n,\alpha)^7\text{Li}$. The latent radiation-damaged areas or tracks are made visible in the di-

electric detecting material by chemically etching the detecting material. The number of tracks per unit area in the detector is proportional to the boron density in the silicon. The path length of the 1.44-MeV alpha particle in silicon is 2.5 μm , and the product of this length and the area yields the volume sampled.

Specimens for analysis were obtained from boron-doped silicon crystals grown by the Czochralski process with a [111] growth axis. Some of the specimens were prepared from polished slices supplied by commercial vendors and others from slices cut and polished in-house. Prior to scribing or cutting the slices into sections for analysis, four-probe resistivity measurements were made on the back surface of each slice in accordance with the standard procedure [1]. For most of the slices, the uniformity of the resistivity across the slice was measured, or had been previously measured on a companion slice cut from the same crystal, by one of the following measurements: four-probe measurements at 100-mil (2.5-mm) increments along two perpendicular diameters, four-probe measurements at center and half-radius positions, or spreading resistance measurements at 25- μm increments along a diameter. All slices had radial resistivity variations of less than 5 percent between center and half-radius positions and no fine structure was observed in the spreading resistance.

In the analysis procedure, a specimen, typically square (7.5 mm on a side) and 0.3 mm thick, was sandwiched between two pieces of cellulose acetate butyrate plastic, vacuum-heat-sealed in polyethylene, and irradiated in the NBS reactor. The irradiation time and location in the reactor were dependent on the anticipated boron density. Time in the reactor ranged from 1 s to 10 min for a typical neutron flux density of $1.33 \times 10^{13} \text{ cm}^{-2}\cdot\text{s}^{-1}$. Following irradiation, the detectors were separated from the silicon specimens, chemically etched in 6.5-normal sodium hydroxide for 5 min at 72°C, and rinsed with distilled water. After drying in air, the detectors were mounted on microscope slides, and the alpha particle tracks were counted with the aid of an optical transmission light microscope. The counting area was 1500 μm^2 ; usually several such areas on the detector were counted and averaged to arrive at a value for each

^{**} Work performed at Jet Propulsion Laboratory under NBS Order No. 611377. NBS contact for additional information: K. F. Galloway.

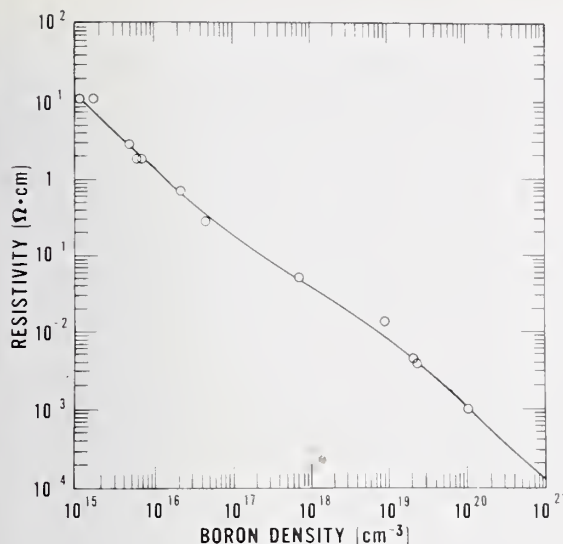


Figure 14. Resistivity of *p*-type silicon as a function of boron density as determined by the nuclear-track technique. (Experimental data shown as open circles; the solid curve is from Wagner [21].)

specimen. Standard Reference Materials, SRM 619 Trace Element Glass Standards, containing known densities of boron in glass [52], were irradiated simultaneously with the silicon specimens. The boron density in the silicon was obtained by comparing the track count from the silicon with that from the boron-in-glass standards with a correction to account for the difference between the range of the alpha particles in silicon and that in glass. In later irradiations, a silicon specimen, previously analyzed with respect to the SRMs, was used as a reference.

Initial results, plotted in figure 14 together with Wagner's empirical relationship between resistivity and boron density, are quite encouraging. Agreement between the nuclear-track data and Wagner's curve is generally better than 10 percent, although a few data points agree much less well. Repeated nuclear-track measurements on the same specimen generally agreed to within a factor of 1.5, but again data on a few slices show wider variation. At this stage in the investigation it is not clear whether the large variations are due to nonuniformity of the boron distribution in an individual slice, to a variability in the nuclear-track measurement, or to some combinations of these conditions. The error associated with track-counting statistics did not exceed 3.5 percent. In some cases, however, the boron den-

sity within a single counting area was observed to vary as much as ± 10 percent; this variability is indicative of the boron distribution only within a $2.5\text{-}\mu\text{m}$ depth from the surface.

The most reproducible nuclear-track determination occurred on a slice with a boron density of $2.26 \times 10^{16} \text{ cm}^{-3}$. The total variability, based on three separate irradiations and counts, was $1 \times 10^{14} \text{ cm}^{-3}$. Electrical measurements of net carrier density and resistivity were made on a companion wafer on which test pattern NBS-3 [28] had been fabricated. The net carrier density (equal to the boron density less the compensating donor impurity density) was found to be $2.22 \pm 0.05 \times 10^{16} \text{ cm}^{-3}$ from junction C-V measurements on five diodes. A value of about $2.1 \times 10^{16} \text{ cm}^{-3}$ was obtained from MOS C-V measurements on a single capacitor. A resistivity of $0.72 \Omega \cdot \text{cm}$ was measured by means of the four-probe collector resistor [53] in the region of interest on the fabricated wafer compared to $0.73 \Omega \cdot \text{cm}$ for the specimen used for the track technique measurements. Additional measurements are being carried out to determine whether this excellent agreement is characteristic of the method.

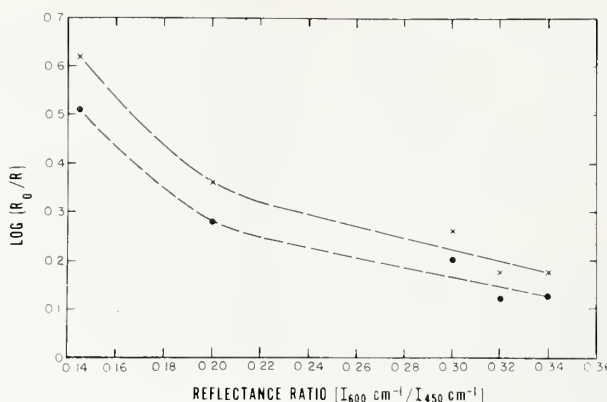
The lower limit of detectability is governed by the background count level. For the present geometry the level is about $5 \times 10^{14} \text{ cm}^{-3}$; thus, a boron density of about 10^{15} cm^{-3} appears to be a lower limit for routine measurements by the nuclear-track technique.

(W. R. Thurber, B. S. Carpenter^{††}, R. L. Mattis, and D. R. Ricks)

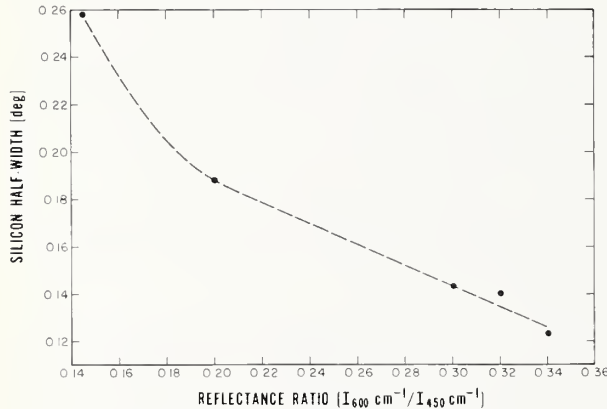
4.5. Optical Test for Surface Quality of Sapphire Substrates

Much of the cost of sapphire substrates for silicon-on-sapphire devices is incurred in the polishing operation. Up to now there has been no quantitative measure of surface quality; both the substrates and the silicon films epitaxially grown on them are passed to subsequent processing steps on the basis of qualitative visual inspections. As a result, sapphire substrates are polished until evidence of surface damage is no longer visible. If devices with satisfactory electrical properties could be produced on substrates with an intermediate degree of polishing, substantial cost savings could result.

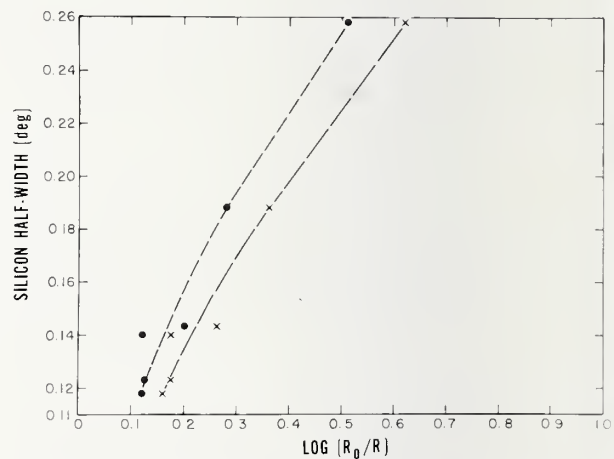
^{††}NBS Activation Analysis Section, Analytical Chemistry Division.



- a. Ultraviolet reflectance ratio at $\lambda = 240 \text{ nm}$ (x) or $\lambda = 280 \text{ nm}$ (●) for epitaxial silicon films as a function of the infrared reflectance ratio of the corresponding sapphire substrate.



- b. Half-width of the x-ray diffraction peak of epitaxial silicon films as a function of the infrared reflectance ratio of the corresponding sapphire substrate.



- c. Half-width of the x-ray diffraction peak of epitaxial silicon films as a function of the ultraviolet reflectance ratio at $\lambda = 240 \text{ nm}$ (x) or $\lambda = 280 \text{ nm}$ (●).

Figure 15. Correlations between optical and x-ray determinations of the quality of a sapphire surface and the corresponding deposited silicon film.

This task was undertaken to develop rapid, nondestructive, quantitative, optical tests for the surface quality of sapphire substrates and for the quality of epitaxial silicon films on sapphire and to establish correlations between the results of these tests and the electrical properties of devices fabricated in the silicon films.

Specimen sapphire substrates were variously polished with diamond grit (of different particle sizes), Linde A^{§§}, and silica sol [54] to introduce different amounts of damage in the different substrates. Infrared multiple-

reflectance spectra were then obtained from the substrates to determine surface character. The quality of each surface was expressed as the ratio of the reflected intensity at wavenumber 600 cm^{-1} to that of wavenumber 450 cm^{-1} (NBS Spec. Publ. 400-25, pp. 20-23) [55]. The higher the value of this ratio, the better is the surface quality. Epitaxial silicon was grown on all substrates simultaneously, and ultraviolet reflectance measurements performed on each silicon film

^{§§} See disclaimer, p. vi.

MATERIALS CHARACTERIZATION BY PHYSICAL ANALYSIS METHODS

to determine the quantity $\log(R_o/R)$ at the wavelengths 240 and 280 nm (NBS Spec. Publ. 400-29, pp. 29-31). The lower the value of this term, the better is the quality of the epitaxial film. The results, which are plotted as $\log(R_o/R)$ as a function of infrared reflectance ratio in figure 15a, indicate that there is a good correlation between the surface quality of the substrate and the epitaxial film characteristics as determined optically.

The epitaxial silicon films were then analyzed by x-ray diffractometry to determine crystalline quality. Figure 15b shows a plot of diffraction peak half-width ($\theta:2\theta$ scan, (400) diffraction plane) for the various silicon films as a function of the infrared reflectance ratio for the corresponding substrates. The larger the value of the diffraction peak half-width, the poorer is the film quality. There is also a good correlation between film character as determined by x-ray diffractometry and the initial substrate character as determined by infrared reflectance. The shape of the curve in fig-

ure 15b is very similar to those in figure 15a, suggesting a correlation between the ultraviolet reflectance and x-ray measurements. This correlation is confirmed by the nearly straight-line plots of figure 15c, in which the x-ray data are plotted as a function of the ultraviolet reflectance data. It has also been observed that when silicon film quality is adversely affected by growth conditions, this condition can be detected by optical reflectance measurements in the ultraviolet. Thus, ultraviolet measurements conveniently can be used to monitor the crystalline character of films independently of whether this character is influenced by substrate character or by growth conditions.

The sensitivity required to ensure satisfactory device operation has not yet been established, but some clarification of this point can be expected from the performance of devices which are being fabricated using the SOS/LSI test pattern (NBS Spec. Publs. 400-19, p. 47, and 400-25, pp. 44-45).

(M. T. Duffy^{¶¶},
P. J. Zanzucchi^{¶¶}, and G. W. Cullen^{¶¶})

^{¶¶}Work performed at RCA Laboratories under NBS Contract No. 5-35915. NBS contact for additional technical information: K. F. Galloway.

5. MATERIALS AND PROCEDURES FOR WAFER PROCESSING

5.1. Ion Implantation Parameters

This task is concerned with the identification of critical parameters associated with ion implantation and with the development of methods for the measurement and control of these parameters. A study [56] was conducted to investigate how the control of depth distributions in silicon depends on the control of the angle between the ion beam and the crystallographic axis of the wafer being implanted. In implantation of low-velocity ions (high atomic number, Z, or low energy, E, or both), a critical angle for channeling, ψ'_c [57], which is proportional to $(Z/E)^{1/4}$ (approximately inversely proportional to the square root of the ion velocity), can approach the commonly employed randomization angle, ψ_{RE} . This situation would seem to imply that channeling should be difficult to prevent for intended random implants of low-velocity ions, or at least that large channeling tails should exist. This hypothesis was tested by measuring and comparing the depth distributions of electrical activity of random and accurately channeled ion implantations and studying the sensitivity of the depth distributions to angular control. For the cases studied, which are representative of most current laboratory implantations, ψ'_c varied from 2 to 7 deg. Learning how implantation distributions change when ψ'_c was comparable to the practical laboratory value of 7 or 8 deg for ψ_{RE} was of particular interest. Another important consideration was the accuracy with which the angle must be controlled to guarantee a particular quality of channeled distribution.

The technique used in this investigation was to implant ions at various angles away from the accurately channeled alignment and toward the direction of random equivalent (RE) orientation up to the RE angle of about 7 deg, and to record the changes in depth distribution of electrical activity measured by differential C-V profiling (NBS Spec. Publs. 400-25, pp. 31-32, and 400-29, p. 40). The implantation dose was $1.5 \times 10^{12} \text{ cm}^{-2}$ and the implants were annealed at 800°C for 20 or 30 min in a dry nitrogen atmosphere. This anneal was shown to fully activate these low dose implants. The implantation angle, ψ , was controlled to less than 0.1 deg for small angles away from axial alignment by a combi-

nation of Rutherford backscattering of protons [58] and a goniometer capable of controlling the angle to about 0.02 deg. From 3 deg to ψ_{RE} the implantation angle was obtained by tilting a standard target mount. This degree of angle control was considered adequate for the larger, and hence likely to be less sensitive, angles. Boron and arsenic ions were implanted at 300, 75, and 20 keV and indium and aluminum ions were implanted at a few selected energies to fill in the range of ψ'_c from 2 to 7 deg. In addition, the analysis of a detailed set of published profiles for phosphorus implanted at 450 keV [59] was included in the study.

It was necessary to devise a method to characterize the change in implanted profile with angle. The technique selected was to measure the differential integrals of the areas between the various depth distributions as illustrated in figure 16. From these one can obtain:

1. the fraction, ξ , of dechanneled ions that are not within the channeled distribution of a perfectly aligned implant, and
2. the fraction, ζ , of ions in a random implant that are deeper than the calculated amorphous distribution which, in accordance with common practice, was computed as a Gaussian approximation using published range and straggle data [60]. Although it is recognized that a more complete theory for describing the implanted profile may attribute some of the tail deviation to other mechanisms, the fraction ζ was taken in this work as the measure of the magnitude of the channeling tail.

Two important results of the study are summarized in figure 17. There is an approximately quadratic dependence of the channeling tail on ψ'_c , as shown in figure 17a. This plot provides a means to estimate the magnitude of channeling for any given implant into bare crystalline silicon performed in the random equivalent orientation at a dose below the onset of amorphization.

The fractions of implanted ions not in channeled distributions are plotted against ψ'_c , in figure 17b. These plots show that the fraction of ions dechanneled increases rapidly as ψ'_c decreases and increases approxi-

MATERIALS AND PROCEDURES FOR WAFER PROCESSING

mately linearly as the implantation angle deviates from the normal to the crystal plane. Accurately channeled distributions can only be achieved at low ψ'_c with a high degree of angular control, whereas as ψ'_c approaches ψ_{RE} , much less control is required.

(R. G. Wilson^{*} and D. M. Jamba^{*})

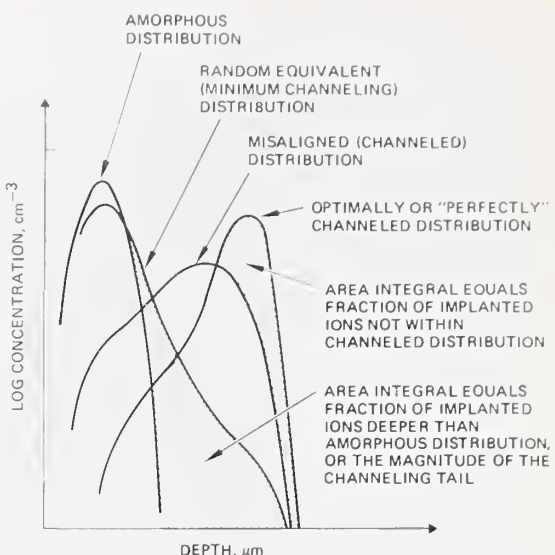
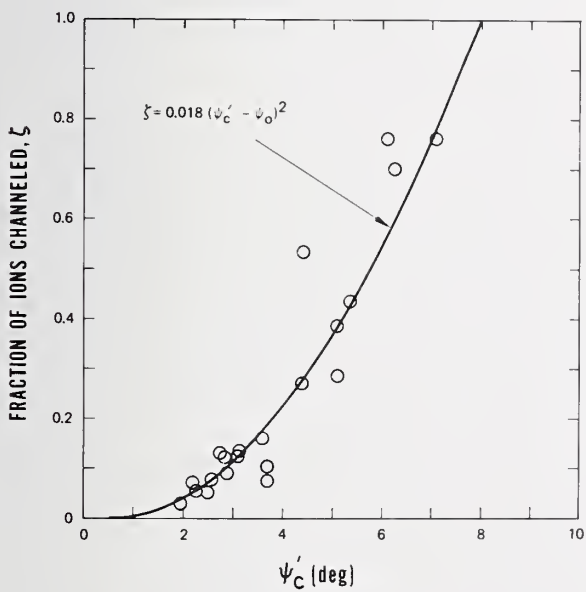
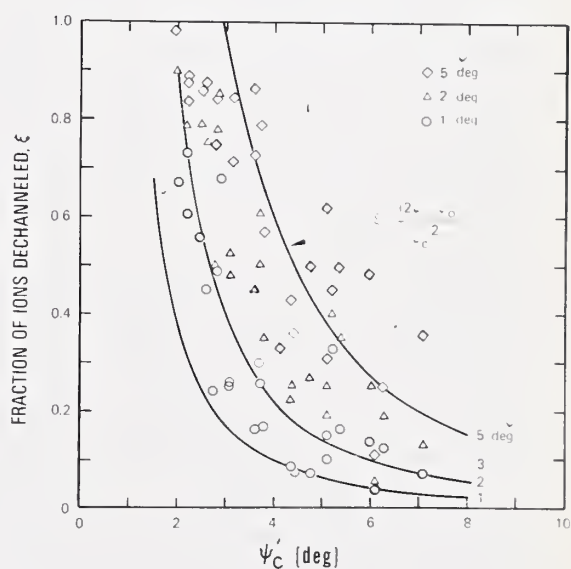


Figure 16. Illustration of implanted random-equivalent and channeled depth distributions and comparisons with ideal amorphous and perfectly channeled distributions, respectively.

^{*}Work performed at Hughes Research Laboratories under NBS Contract No. 5-35891. NBS contact for additional information: K. F. Galloway.



- a. Fraction, ξ , of ions channelled in a random equivalent distribution, 7 deg off the crystallographic axis. The solid line represents the empirical relation: $\xi = 0.018 (\psi'_c - \psi_0)^2$, where ψ_0 is an empirical constant.



- b. Fraction, ξ , of ions dechanneled in a channeled distribution misaligned by an angle ψ from the crystallographic axis for $\psi = 1$ (○), 2 (△), and 5 (◊) deg. The solid lines represent the empirical relation: $\xi = (2\psi - \psi_0)/\psi'^2$.

Figure 17. Fraction of implanted ions outside ideal distributions as a function of the critical angle for channeling, ψ'_c .

6. PHOTOLITHOGRAPHY

6.1. Optical Imaging for Photomask Metrology

Additional investigations of the effects of the operating conditions of an optical microscope on line-width measurements in transmitted illumination were completed [61]. In particular, the effects of non-zero transmittance of the opaque background and of spherical aberration and defocus, not included in the previously reported work (NBS Spec. Publ. 400-29, pp. 50-52), were studied.

It was found that the 25-percent transmittance criterion for edge location in a microscope with diffraction-limited optics and numerical apertures of 0.60 for the condenser lens and 0.90 for the objective lens is appropriate for clear lines as narrow as 0.5 μm in a completely opaque background. If the background has finite transmittance, T_0 , the transmittance, T_c , which corresponds to the true edge location, is given by

$$T_c = 0.25 (1 + \sqrt{T_0})^2 . \quad (28)$$

As an example of this correction, consider a black chromium photomask with $T_0 = 0.004$; the transmittance at the true edge location would be 0.36 rather than 0.25. If the measurement were made with an objective lens with a numerical aperture of 0.90, and if the 25-percent transmittance criterion were used, the line would appear to be 0.08 μm wider than its actual width. This error would increase with the presence of either defocus or spherical aberration.

The focus setting, or the resulting amount of defocus, in an optical microscope is known to significantly affect the line image. Another optical aberration, which is similar to defocus, is spherical aberration. This aberration is usually present to some degree in most microscopes and can be partially compensated by the focus setting. Figure 18 shows the calculated image profiles of a 10- μm wide clear line for a microscope with constant 2λ of spherical aberration and defocus varying in steps of $\lambda/4$ from 0 to -2λ . The numerical aperture is 0.22 for the condenser and 0.65 for the objective. The choice of 2λ of spherical aberration corresponds to using an incorrect tube length between the objective and eyepiece (i.e., 160 mm instead of 220 mm) or using a sample cover glass whose thickness does not match the thickness for which the objective was designed (i.e., 0.12 mm instead of 0.17 mm). The curve for $-\lambda$ of de-

focus has the steepest slope, whereas the curve with $-\lambda/2$ of defocus has the maximum contrast between the edge and the first dark band (ringing). Since the optimum focus setting is usually selected on the basis of the image profile exhibiting the steepest slope or the maximum ringing, a focus setting between those corresponding to $-\lambda/2$ and $-\lambda$ of defocus would correspond to optimum focus. For any of these settings, the true edge location corresponds to the 25-percent transmittance if the background is assumed to be completely opaque.

The effect of making the measurement with white light rather than quasi-monochromatic light was also considered. If white light rather than monochromatic illumination is used in an optical microscope, additional measurement errors may be introduced. Figure 19 shows typical experimental profiles of one edge of a nominally 10- μm wide clear line for white light and filtered light at 560 nm. The significant differences between the edge profiles are due to both chromatic aberrations and variation in image magnification with illumination wavelength. All of the microscope objectives examined exhibited this difference to a varying degree indicating the presence of varying amounts of longitudinal chromatic aberration and chromatic difference of magnification.

Based on the present results, it appears that recommended equipment for accurate measurement of the width of photomask lines as narrow as 0.5 μm with an optical microscope using transmitted light will include the following: 1) the ratio of the numerical aperture of the condenser lens to the numerical aperture of the objective lens should be less than 1.0 (a reasonable choice is 0.60/0.90.); 2) the sample illumination should be filtered to give monochromatic light peaked at the best response of the optical system; 3) the focus mechanism should be adjustable to within a tolerance of $\lambda/4$ (corresponding to $\pm 0.35 \mu\text{m}$ for an objective lens with a numerical aperture of 0.90 and illumination wavelength of 560 nm); and 4) a transmittance of 25 percent corrected for the finite transmittance of the opaque area of the photomask should be used as the criterion for line-edge location. The only presently known method of determining the 25-percent threshold value on the image profile is from a photometric scan of the image. The NBS optical-microscope system can presently measure line widths to within an uncertainty of

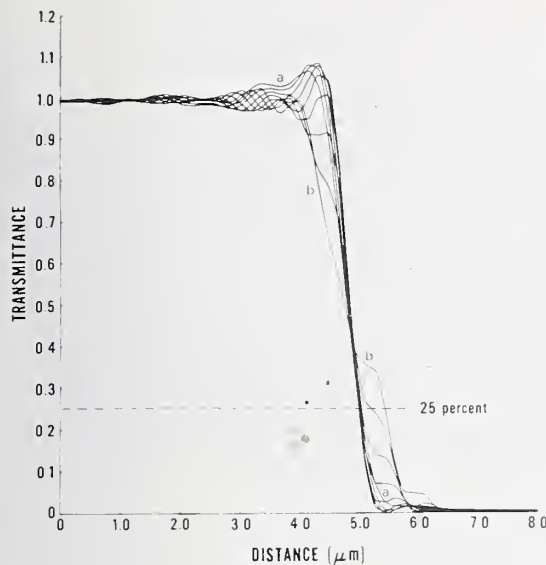


Figure 18. Calculated image profiles of a 10- μm wide clear line for an optical microscope with a constant 2λ of spherical aberration and defocus varying in steps of $\lambda/4$ from 0 (a) to -2λ (b), 0.22 NA condenser and 0.65 NA objective, illumination wavelength of 560 nm, and 0.13- μm wide scanning slit.

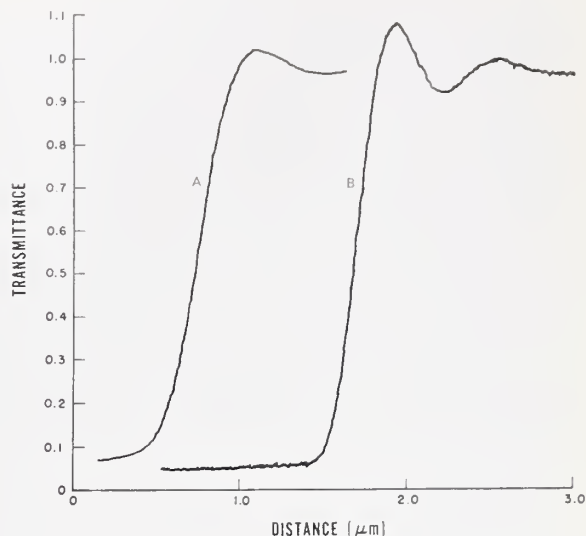
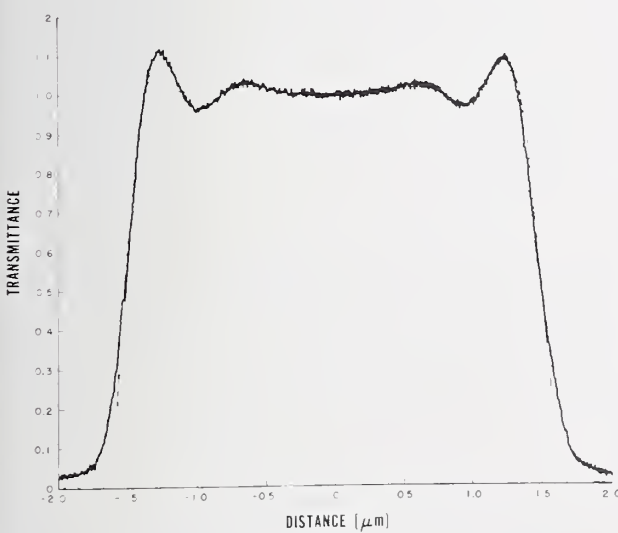
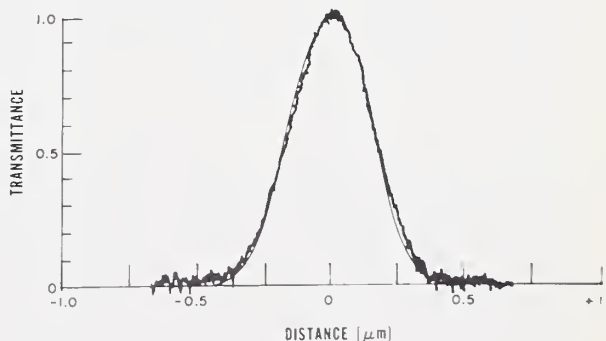


Figure 19. Experimental image profiles of one edge of a nominally 10- μm wide clear line for an optical microscope with white light (A) and filtered light at 560 nm (B), 0.60 NA condenser and 0.90 NA objective, and 0.13- μm wide scanning slit.



a. Line width: 3.15 μm .



b. Line width: 0.5 μm .

Figure 20. Comparison of theoretical and experimental image profiles (wave trace and smooth line, respectively) of clear lines for an optical microscope with 0.60 NA condenser and 0.90 NA objective, illumination wavelength of 560 nm, and 0.13- μm wide scanning slit.

PHOTOLITHOGRAPHY

$\pm 0.2 \mu\text{m}$. If the scan is repeated at the same position on the line, the uncertainty is less than $\pm 0.05 \mu\text{m}$.

The remaining source of error is the edge quality of the photomask. The test specimens used were the best obtainable with less than $0.1-\mu\text{m}$ variations barely observable optically at high magnification. However, variations in the edge response were observed. Some indication of the variation may be found in comparison of the right and left edges of the typical experimental profiles given in figure 20, although these profiles have been selected for edge sharpness in order to get the best possible correspondence with theory. It appears that the edge quality may be the

limiting factor in the accuracy and repeatability of line-width measurements below $10 \mu\text{m}$.

The largest contributions to variations in the measurement appear to be due to 1) non-repeatability of focus at high numerical apertures with conventional fine-focus adjustments found on microscopes; 2) variation in edge quality, which has a noticeable effect for state-of-the-art photomasks; and 3) the effect of chromatic aberrations in the microscope when white light is employed. These sources of error will affect measurements made with filar and shearing eyepieces as well as photometric image scans, although they may be masked because of larger variations contributed by visual factors.

(D. Nyssonen*)

* NBS Optical Physics Division.

7. TEST PATTERNS

7.1. Cross-Bridge Sheet Resistor

The sheet resistance of a conducting layer is usually measured with a four-terminal conducting sheet in the shape of a bridge [62] or a van der Pauw [62,63] test structure. Since the sheet resistance as measured with the bridge structure depends on the length-to-width ratio of the bridge while that as measured with the van der Pauw structure does not, it is possible to determine the width of the bridge structure as well as the sheet resistance by combining electrical measurements from these two structures provided the actual sheet resistances of both structures are identical (NBS Spec. Publ. 400-17, pp. 22-24) [28].

A new structure has been designed which incorporates both bridge and van der Pauw elements. This structure requires six probe pads instead of the eight required by separate structures. The greater compactness of the new structure assures that the sheet resistance of the van der Pauw element is more nearly equal to the sheet resistance of the bridge element than would be the case for separate structures. In designing the van der Pauw part of the new test structure, the cross design (NBS Spec. Publ. 400-29, pp. 64-65) [64] was used; hence, the name: cross-bridge sheet resistor.

The new structure, shown in figure 21, was designed to be compatible with the NBS 2 by N probe pad array, where N is an arbitrary integer (NBS Spec. Publ. 400-25, pp. 41-43). The sheet resistance, R_s , is calculated from measurements on the cross part of the resistor:

$$R_s = (V/I)(\pi/\ln 2) , \quad (29)$$

where the potential difference, V, is $V_1 - V_2$ for a current, I, passed into I_1 and out of I_2 . The effective width of the current-carrying channel, W_e , is calculated from measurements on the bridge part of the sheet resistor:

$$W_e = R_s L (I^*/V^*)(1 - E) ,$$

where the potential, V^* , is $V_{1^*} - V_{2^*}$ for a current, I^* , passed into I_{1^*} and out of I_{2^*} ; L_m is the distance, determined from the photomask, between the voltage taps of the bridge; and E is a correction term which takes into account the error due to the perturbation of

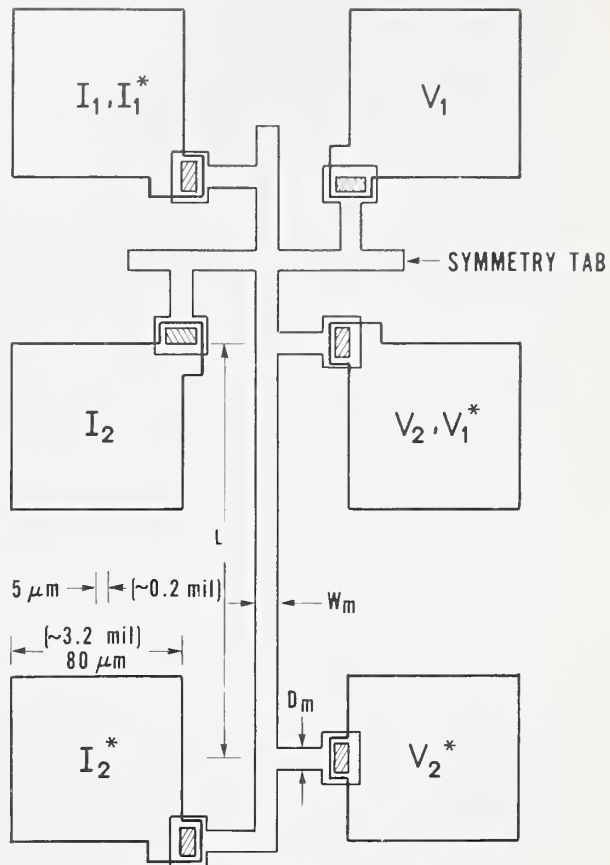


Figure 21. Schematic diagram of the cross-bridge sheet resistor. (Metallized contact to a diffused sheet resistor is shown by the cross-hatched areas. For a metal sheet resistor, the entire structure is metallized.)

the voltage taps. If the test structure is a diffused layer, the effective width, as shown in figure 22, is given by:

$$W_e = W_m + \alpha X_j + W_{oe} ,$$

where W_m is the width of the line on the photomask, W_{oe} accounts for the over-etching, X_j is the junction depth, and α is the lateral diffusion factor [65]. If the test structure is a metallized layer, the effective width is given by:

$$W_e = W_m - W_{oe} .$$

The cross part of the sheet resistor was designed to permit the sheet resistance to be

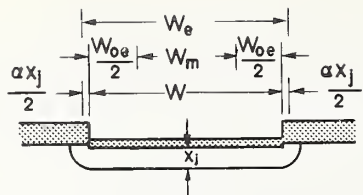


Figure 22. Cross-sectional view of a diffused region showing various dimensions.

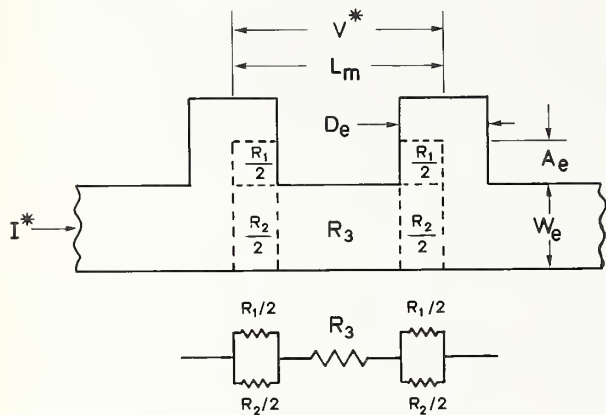


Figure 23. A simple equivalent circuit model for the bridge sheet resistor. (The current lines penetrate the side arms at a distance A_e .)

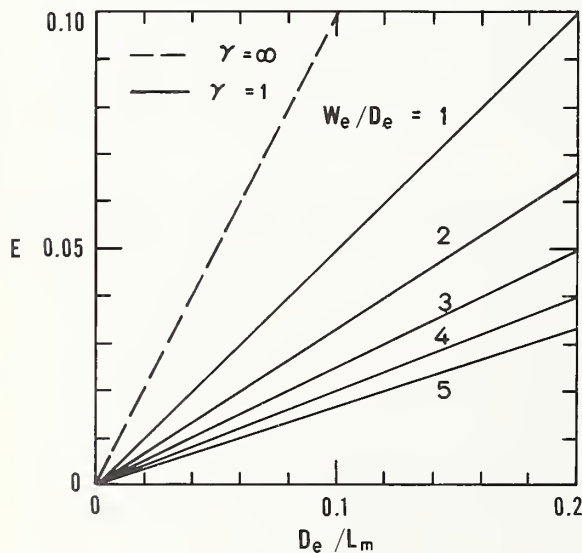


Figure 24. Normalized width error, E , anticipated from measurements on a bridge test structure. ($\gamma = A_e/D_e$.)

calculated from eq (29) without requiring additional correction factors for contact shorting or asymmetry. Previous analysis has shown that the contact-shorting error for a Greek cross is less than 0.1 percent if the length of the arm is greater than the width of the arm (NBS Spec. Publ. 400-29, pp. 64-65) [64]; therefore, this structure was designed so that the length of each arm of the cross is much greater than the width of the arm. Symmetry tabs were introduced at the ends of the three arms denoted I_1 , I_2 , and V_1 in order to compensate for the effect of the bridge structure which is extended from the arm denoted V_2 .

Because this structure is expected to be suitable for making measurements on minimum line-width geometries, the effect of the contact arms on the bridge structure must be considered. It can be shown, with the aid of the simple equivalent circuit model in figure 23, that

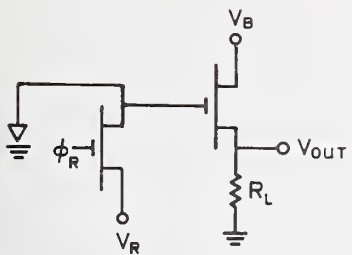
$$E = \frac{D_e}{L_m} \left(1 + \frac{W_e/D_e}{A_e/D_e} \right)^{-1}, \quad (30)$$

where the symbols represent dimensions given in the figure. The value for $\gamma \equiv A_e/D_e$ is not known. The worst case, where the contact arms effectively short the current flow so that $R_1 = R_2 = 0$, is represented by $\gamma = \infty$. A more realistic, but still conservative, case is the case in which $\gamma = 1$. An evaluation of the error as a function of D_e/L_m is given in figure 24 for these two values of γ . For the minimum line-width case, D_e is equal to W_e ; if $\gamma = 1$ and $D_e/L_m = 0.05$ (as is the case for the structure illustrated in fig. 21), E is equal to or less than 2.5 percent. A more detailed analysis, either experimental or mathematical, is needed to establish better estimates for γ , and hence E , but a width error correction of this magnitude is of little concern in many applications. (M. G. Buehler)

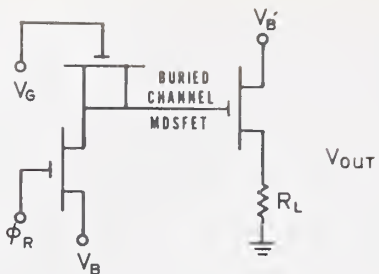
7.2. Advanced Planar Silicon Test Structures

This task was undertaken to determine the operational limitations and potential applications of integral electrometer amplifiers used as test devices in specialized circuits. The use of an electrometer amplifier in a sampling circuit configuration allows for the measurement of small currents. It is an ideal high-impedance device that can be interfaced with an active circuit element such as

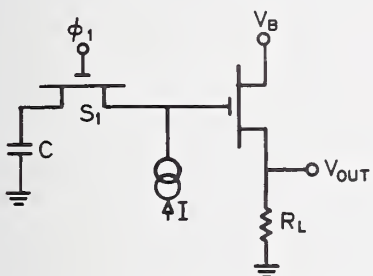
TEST PATTERNS



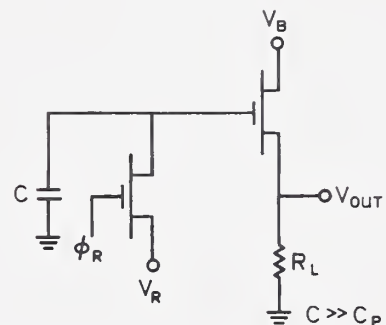
- a. Gated diode sampling circuit with electrometer for measurement of junction leakage current, bulk lifetime under diffused region, and surface recombination velocity.



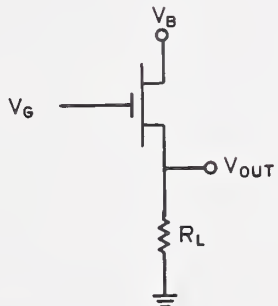
- b. Buried channel MOSFET circuit with electrometer for measurement of bulk lifetime and surface recombination velocity.



- c. MOS capacitor with electrometer for dc measurements of oxide (insulator film) thickness.



- d. MOS capacitor with electrometer for transient measurements of lifetime under gate oxides and surface state studies.



- e. Basic electrometer circuit.

Figure 25. Schematic diagrams of advanced test structures.

a diode or capacitor to measure small charge fluctuations. It is intended to perform and evaluate both ac and dc measurements.

A number of quantities which relate to parameters that must be controlled in various phases of silicon device and integrated circuit manufacturing are very small in magnitude and require exacting time-consuming measurements with sensitive apparatus. With an appropriately calibrated electrometer amplifier very small currents can be sampled and measured with high-speed testers to provide data rapidly and in sufficient quantity for statistically significant results.

The different electrometer output configurations being considered are illustrated in figure 25. A test pattern array is being designed, using the 2 by N modular concept, so that each of these can be evaluated and that the results obtained can be compared with those from more conventional test structures. (D. McCarthy^{*}, B. Godwin^{*}, M. L. Lonky^{*}, and D. S. Herman^{*})

7.3. Test Pattern Design and Analysis for SOS/LSI

This comprehensive test pattern is being developed to provide a means for characterizing and monitoring a large-scale integration (LSI), silicon-on-sapphire (SOS) process and other mask compatible processes (NBS Spec. Publ. 400-25, pp. 44-45). The mask set has been designed and produced, and a number of

test wafers have been fabricated. During this period, the principal emphasis has been on development of test programs for selected structures and measurement of the characteristics of individual structures of types I and II which are intended to test design and process parameters and spatial variations, respectively (NBS Spec. Publ. 400-19, p. 47).

A result of general interest was obtained in connection with the measurements on the cross-shaped van der Pauw sheet resistor (NBS Spec. Publ. 400-29, pp. x, 64-65). This essential structure is present in a number of devices in the type I pattern. Analysis of this structure [64] indicated that the geometrical error introduced should be much less than could be observed by the measurement system. Measurements of structure I-53 (p^+ poly) indicated that at a current level of 1.00 mA, the applied voltage of about 142 mV produced a measured signal of about 17 mV for a ratio of about 12 percent and a sheet resistance of $75.8 \Omega/\square$. On conventional bridge-shaped structure I-63 a nominal value of $76.8 \Omega/\square$ was measured; in this structure a current level of 1.00 mA produced a measured signal of about 45 mV, or approximately three times that of the van der Pauw device. The agreement between the two measurements is well within the uncertainties of the geometry of the bridge-shaped specimen. It is therefore quite clear that the cross-shaped van der Pauw structure has no serious design or theoretical problem. This structure allows a very fine spatial resolution of resistivity.

(W. E. Ham[†])

^{*}Work performed at Westinghouse Defense and Electronic System Center under NBS Contract No. 6-35766. NBS contact for additional information: M. G. Buehler.

[†]Work performed at RCA Laboratories under NBS Contract No. 5-35916. NBS contact for additional information: M. G. Buehler.

8. ASSEMBLY AND PACKAGING

8.1. Correlation of Moisture Infusion, Leak Size, and Device Reliability

Of crucial importance to the examination of moisture infusion as a function of leak size is the accuracy of the dew-point measurement method intended for the determination of the amount of moisture present in the test packages. Previously, the precision of this method was evaluated through exposure of the dew-point sensors directly to controlled macroenvironments of an environmental chamber (NBS Spec. Publ. 400-25, p. 56). Environments ranged in dew-point value from about -10°C to 30°C, which covers the range from 0.25- to about 4.3-percent water vapor. Dispersion in the dew-point measurements appeared to be about 5°C, with most of the error related to the techniques involved in calibrating a microsensor in a macroenvironment.

Two procedures were selected for evaluation of the dew-point method as applied to package interiors, where ionic content and sorption kinetics can be expected to affect the measurements. One procedure was to seal test packages containing atmospheres of known water-vapor content introduced through a miniature valve and then to determine this content with the dew-point measurement. The second procedure was to include a miniature aluminum oxide dielectric moisture sensor, now in the developmental stage [66], into the test package for use as a transfer reference. A special series of 27 hybrid test packages was fabricated for the evaluation. Each 24-pin dual-in-line metal package was equipped with one or two miniature valves, a temperature sensor, and a dew-point sensor, as pictured in figure 26. Seven of the packages were also equipped with an oxide sensor [67].

For the calibration of the oxide sensors, one package was delidded, the valve stems were removed from the others, and PTF tubing was inserted into the valve stem guides. Test air was introduced at a slight positive pressure and of known moisture content as obtained with a two-pressure generator [68]. When the sensor outputs steadied, readings were made. Calibration was performed over the range from 100 to 12 000 ppm water vapor by volume at room temperature (25°C) and at 85°C. Moisture points were generated in increasing and decreasing sequences to provide a test for hysteresis. Moisture content of the test air was known to an accuracy of ± 3 percent for the range from 100 to 250 ppm and to ± 0.5 percent for the range from 250

to 12 000 ppm. Typical results are given in figure 27.

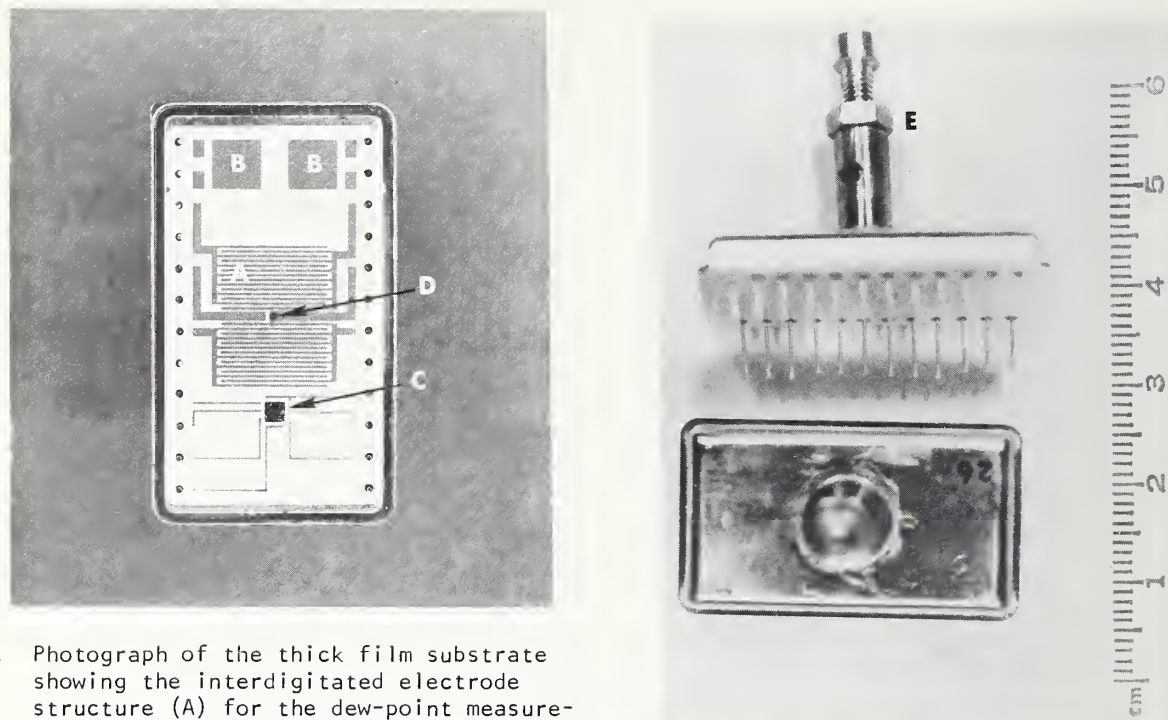
The packages were then divided into sets with an electric hygrometer sensor in each set. Moist air was flushed into the packages as before until steady-state conditions were reached. Valve stems were replaced and the packages were sealed while in the moisture generator. The packages contained 96.2, 442, 994, 6263, or 12 020 ppm water vapor by volume as obtained with the two-pressure generator.

Dew-point measurements were made by chilling the test package while monitoring both the internal temperature and the leakage current between the interdigitated electrodes of the dew-point sensor. A sample result, taken with a bias of 10 V, is shown in figure 28. The dew point was taken as the temperature at which the leakage current indicated a 20-percent change from the baseline leakage of the circuit (NBS Spec. Publ. 400-25, p. 56). In the case illustrated, the measured dew point was about 4°C, which corresponds to about 10 000 ppm water vapor by volume. The reason for the maximum at about -7°C and the decrease in leakage current at lower temperatures is not yet understood.

The effect of bias voltage on the measured dew point was also examined. A 20-percent deviation occurred at 10°C (12 000 ppm) with 50 V applied and at 13°C (15 000 ppm) with 100 V applied. The 50- and 100-V biases saturated the amplifier so that peak values could not be obtained. The results obtained on all the packages measured are summarized in table 8. It can be seen that these results are not very complete or consistent. It is hoped that suitable agreement between the oxide sensor and the dew-point sensor may follow from suitable choice of dew-point sensor bias voltage and point of deviation from baseline current.

(R. Sulouff^{*} and S. Ruthberg)

^{*}Work performed at Martin Marietta Aerospace, Orlando Division, under NBS Contract No. 5-35880.



- a. Photograph of the thick film substrate showing the interdigitated electrode structure (A) for the dew-point measurement, bonding pads (B) for the oxide moisture sensor mounted in selected packages, and the bonding pad and interconnect system (C) for the 741 operational amplifier to be used in subsequent tests to monitor effect of moisture on circuit operation. A temperature sensing diode is mounted at point D.

- b. Photograph of exterior of test package showing miniature valve (E).

Figure 26. Hybrid test packages for use in the moisture infusion study.

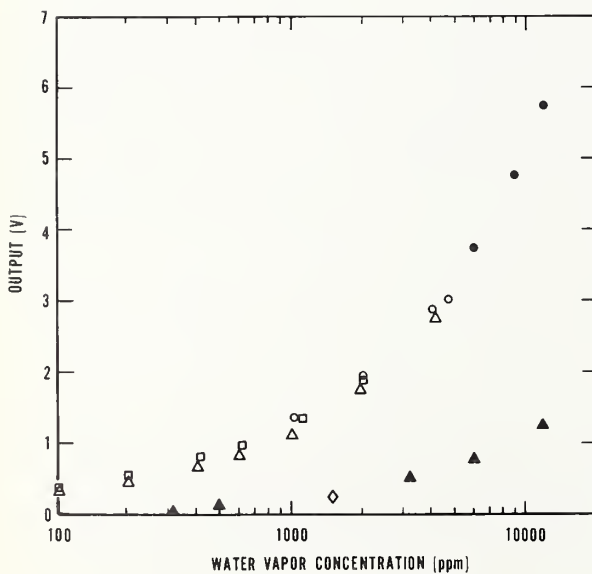


Figure 27. Typical calibration data for oxide moisture sensor. (Sequence of tests: At 25°C: ●, increasing moisture level; ○, increasing; □, decreasing; △, increasing. At 85°C: ▲, decreasing; ◇, increasing.)

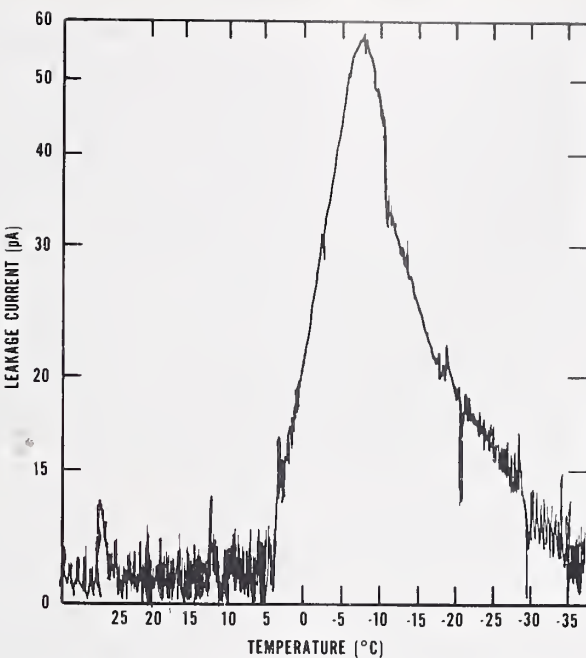


Figure 28. Typical dew-point sensor response curve of leakage current as a function of substrate temperature. (Applied voltage: 10 V.)

Table 8 — Oxide Sensor and Dew-Point Determination of Moisture Content of Sealed-Off Test Packages

Test Package ^a	Sealed-In ^b	Water Vapor Concentration, ppm		
		Oxide Sensor	Dew Point Sensor Peak	20% Deviation
5	96.2	c	d	d
6	994	6 200	d	d
7	6 263	6 200	3 300	10 050
8	12 020	12 300	10 000	20 000
9	422	3 500	c	c
22	6 263	e	17 000	22 000
27	96.2	e	330	1 050
28	12 020	e	6 000	18 000

^a Sixteen other packages without oxide sensors which had sealed-in water vapor concentrations in the range from 96.2 to 12 020 ppm gave no change in leakage of the dew-point sensor as the temperature was lowered.

^b Measured with an electric hygrometer sensor.

c Electrical failure; no result obtained.

d No change in leakage of the dew-point sensor observed.

e Package did not contain an oxide sensor.

8.2. Loose-Particle Detection[†]

Additional studies were completed on selected aspects of a draft procedure for the particle impact noise detection (PIND) test which is being considered for inclusion in MIL-STD-883, Test Methods for Microcircuits, as Method 2020/20xx. In previously reported work (NBS Spec. Publ. 400-29, pp. 75-76) it was shown that each of the three recommended couplants was satisfactory for transmitting the exciting mechanical vibrations to the microcircuit. In addition, the impact frequencies of metal spheres (of representative sizes and materials) with an elastic wall were calculated and shown to be considerably higher than the frequency of maximum response of the PIND test system, which ranges from about 130 to 170 kHz. Nevertheless, it was concluded that particle impacts should be able to shock and excite the ultrasonic detection transducer, thus producing a measurable output.

During the present period, the effectiveness of the couplants for transmitting high-frequency vibrations was investigated in detail. In the PIND test, the high-frequency (acoustic emission) signals which are generated when a particle vibrated at a low frequency hits the wall of the package must be transmitted through the package wall, through the couplant, and into the ultrasonic transducer in order to be detected. The transmissibility of the couplant therefore has a considerable influence on the effectiveness of the PIND test in detecting the presence of small loose particles in the package.

In these tests, the amplitude frequency-response characteristics of three acoustic emission transducers (A, B, and C) of the same type were determined when they were driven through the couplant by a wide-band acoustic emission transducer, and swept over a frequency range from 5 to 500 kHz in about 30 s. The wide-band (5 kHz to 2 MHz) transducer was mounted in a fixture with its sensing surface facing up and in the horizontal plane. The test transducer with its sensing surface down was placed on the driver. A single layer of tape couplant, typically 0.4 mm thick for tape K and 0.1 mm thick for tape L, or a 0.1-mm thick layer of viscous liquid couplant M bonded the two surfaces together. The wide-band transducer was driven electrically by a low-impedance, constant-voltage function generator at an output of 5.0 ± 0.1 V rms.

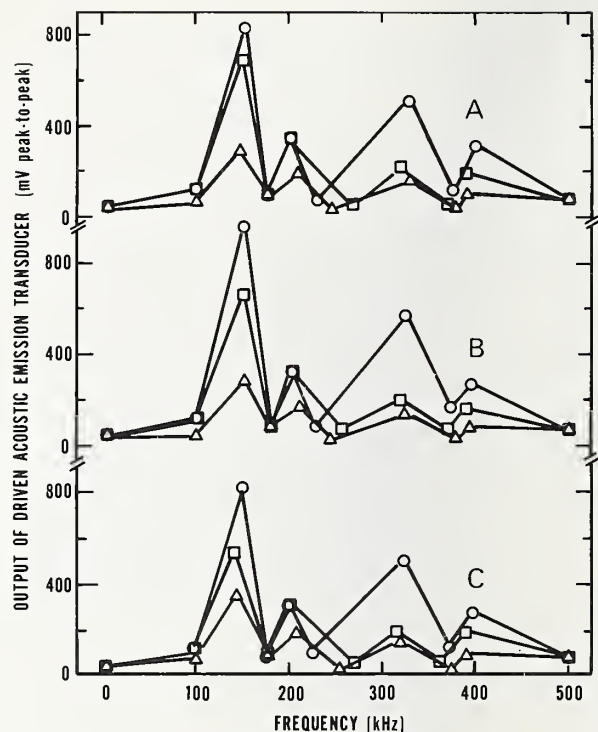


Figure 29. Average response of three driven acoustic emission transducers A, B, and C attached to driving acoustic emission transducer by couplant K (Δ), L (\square), or M (\circ), as a function of driving frequency.

Five runs were performed for each couplant with each test transducer, and the averaged results are shown in figure 29. Since the frequency response of the driving transducer is reported by its manufacturer as being smoothly rising about 10 dB from about 10 kHz to 2 MHz, it is likely that the peaks in the response shown in the figure are those of the test transducers. These peaks occurred roughly at 150, 200, 325, and 400 kHz. The maximum response for all test transducers and couplants occurred at about 150 kHz.

It should be noted that the response with the viscous couplant was larger than that obtained using the tape couplants for all three test transducers. At about 150 kHz output amplitudes for all transducers averaged 863 mV with this couplant, 627 mV for

[†]Principally funded by SAMSO with additional funding from the NBS Nondestructive Evaluation Program.

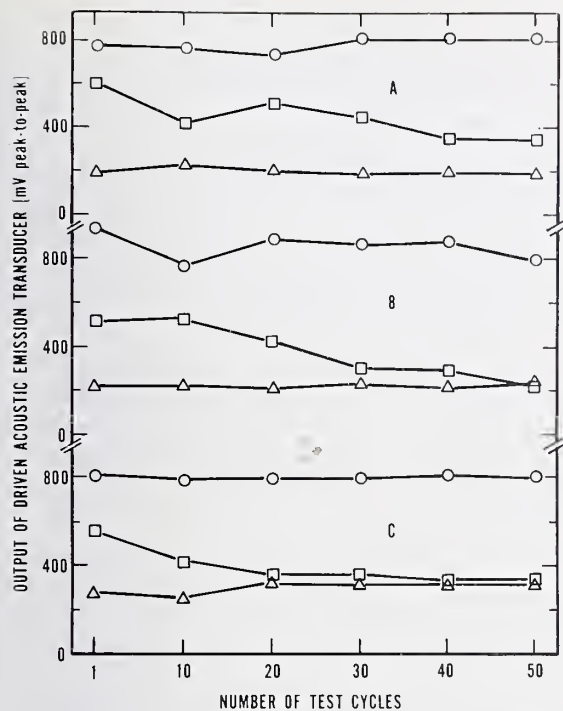


Figure 30. Response of three acoustic emission transducers A, B, and C attached to driving acoustic emission transducer by couplant K (Δ), L (\square), or M (\circ) and driven at 150 kHz, as a function of number of removal and remounting cycles.

tape L, and 292 mV for tape K. Differences between the couplants at 325 kHz were more pronounced than those at 150 kHz; again the viscous couplant resulted in the largest output.

One application of couplant is expected to be used to test a number of microcircuit packages. In the case of tape K, for example, the proposed test method specifies replacement of the couplant at least once for each 50 parts tested.

The amplitude-frequency responses of transducers A, B, and C were determined as above after the test transducer was first mounted using a fresh application of couplant, and after the transducer had been removed and remounted 10, 20, 30, 40, and 50 times, respectively. In this case, one run was made using each of the three couplants with each of the three transducers. The output signal amplitude at 150 kHz is plotted in figure 30 as a function of the number of remounts. The results show a decided decrease in this signal amplitude when using tape couplant L;

Table 9 — Response of Test Transducers at 150 kHz Obtained Using Viscous Liquid Couplant M

Transducer	Average of 5 Runs, mV	Relative Sample Standard Deviation, ^a %
A	777	4.7
B	858	7.3
C	803	10.2
Grand Average	812	5.1

^a The variability includes the couplant in all cases.

the amplitudes after 50 remounts were 57, 43, and 61 percent of the initial amplitudes for transducers A, B, and C, respectively. Tests with tape couplant K showed a change of less than 10 percent in output during the 50 mountings and removals, and viscous liquid couplant M less than 15 percent, for all three transducers. It should also be noted that the output with viscous liquid couplant M at the end of the test was 2 to 4 times that of the tape couplants in all cases.

The above data can be used to compare the performance of the three test transducers. Since viscous liquid couplant M produced the most repeatable results, test results from its use were analyzed. The results at 150 kHz, summarized in table 9, suggest that the three test transducers have very similar performances as far as sensitivities and resonances are concerned. However, the sample is too small for these results to be regarded as indicative of the characteristics of all transducers of this type.

At this stage of the investigation it appears that the viscous liquid couplant M is more effective in transmitting acoustic emission signals than the two tape couplants. In addition, couplant M appears to give more repeatable results during the testing procedure.

(P. S. Lederer[§], J. S. Hilten[§], and C. F. Vezzetti[§])

[§]NBS Components and Applications Section, Electronic Technology Division.

9. DEVICE INSPECTION AND TEST

9.1. Scanning Acoustic Microscopy

During this period, efforts on the development of the scanning acoustic microscope for application to examination of semiconductor devices and integrated circuits have been directed primarily toward examination of a variety of test specimens and study of the images in order to begin to acquire a greater understanding of the information which can be obtained by this technique [69,70].

Stanford Project — In this part of the work, the microscope has been used in both the transmission mode and the reflection mode. Thinned wafers have been used as specimens in connection with the transmission mode of operation. Although these wafers do not correspond to production items, they permit comparison of the image in transmission with the image in reflection. The ability to make this comparison proves to be of value in interpreting the results for the reflection mode.

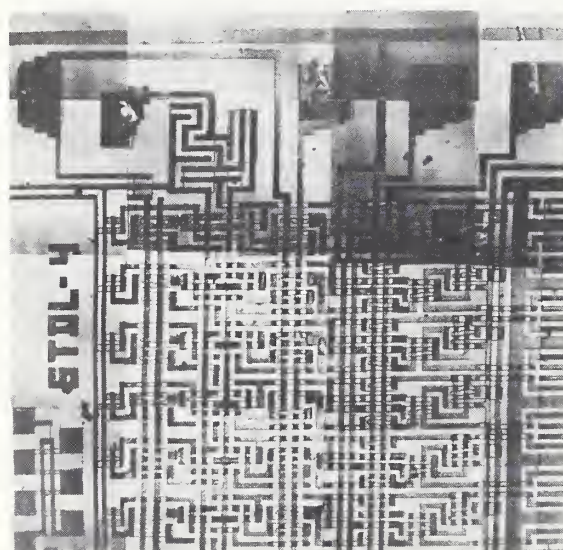
With the reflection mode, short pulses some 4 ns in length at a frequency near 850 MHz are being used. The images obtained are improved over those reported previously (NBS

Spec. Publ. 400-29, pp. 80-83), because the signal-to-noise ratio has been improved by increasing the amplitude of the pulse at the input transducer. With the transmission mode, both the change in amplitude and the change in phase through the thinned wafer have been monitored. It is now evident that there is much more information available in the "phase-only" images in those regions where the amplitude remains nearly constant.

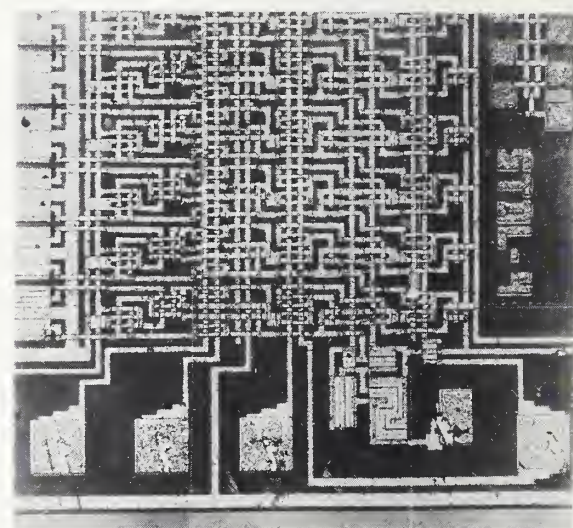
In this work, time gating techniques have been used to delineate different levels in the specimen. It has been found possible to focus on both the front and back surfaces of a wafer thinned by mechanical polishing to about 6 μm .

Figure 31 provides a comparison between acoustic images (fig. 31a) and an optical photomicrograph taken with interference contrast (fig. 31b). The specimen* is a portion of a C-MOS-on-sapphire integrated circuit. The lines on this circuit are about 5 μm wide. These images illustrate the resolution now

* Supplied by P. Hagon, Autonetics Division of North American Rockwell.



a. Scanning acoustic micrograph. Magnification: $\sim 300x$. Note the edge definition, contrast changes at crossovers, and resolution of the metallization lines which are about 5 μm wide.



b. Optical photomicrograph taken with interference contrast. Magnification: $\sim 250x$.

Figure 31. Scanning acoustic and optical photomicrographs of a portion of a C-MOS-on-sapphire integrated circuit.

available with the acoustic microscope. The differences in contrast at the crossovers of various elements in the acoustic image are noteworthy.

(C. F. Quate[†])

Hughes Project — In this part of the work, the microscope is operated at a frequency of about 400 MHz; operation in both the cw and pulsed reflection modes (NBS Spec. Publ. 400-29, pp. 79-81) is possible. From study of an Ealing 22-8635 High Resolution Test Target,[§] photolithographically replicated with gold metallization, 300 nm thick, on silicon-on-sapphire wafers, it was concluded that the resolution capability of the microscope operated at 370 MHz in the pulsed reflection mode can approach 1.5 μm at 10-percent contrast [71]. The resolution at 50-percent contrast is 2.8 μm . The acoustic wavelength in water is 4.0 μm at 370 MHz; thus it appears that the resolution capability of the microscope is about one-third of the acoustic wavelength in water. If linear extrapolation remains valid, a decrease of lens radius to 0.1 mm and an increase of operating frequency to 1500 MHz, both reasonable values, would be expected to increase the resolution of the system by a factor of 4, or to about 0.3 or 0.4 μm .

Since the completion of the pulsed reflection system, many integrated circuits and other specimens have been examined. The images of the integrated circuits and other planar specimens have shown surprising detail that results from the greater-than-expected line resolution capability of the instrument, noted above. In all of these imaging experiments another interesting behavior of the acoustic system has come to light. This behavior appears in all types of specimens examined and is, therefore, thought to be characteristic of the acoustic lens system itself. Repeated intensity maxima and minima are observed as the specimen is moved through the lens focal plane parallel to and toward the lens, as illustrated schematically in figure 32. These intensity extremes are manifested as contrast inversions as the distance between the lens and the specimen is changed. These contrast inversions are illustrated in figure 33, which shows the image of a 300-nm thick gold mesh on silicon obtained with the pulsed re-

flection mode at the various lens-to-specimen positions between 0 and -4 as indicated in figure 32. As can be seen, the greatest resolution occurs at the -2 position; this is the position used in the resolution studies described above.

Based on experience with the scanning acoustic microscope to date, it is believed that the instrument, when fully developed, will be capable of detecting two distinctly different kinds of structural features. One such feature constitutes a local defect, such as a void beneath a metallization as shown in figure 34. In this figure, a portion of a 0.5- μm aluminum surface metallization makes no contact with the layered structure beneath it. The complex reflection coefficient (only the magnitude is shown) changes abruptly as the acoustic beam crosses the buried void, resulting in distinct image intensity changes which can be readily resolved by the microscope.

The second and equally important diagnostic measurement which the microscope is in principle able to make quantitatively is of the thickness of the layered regions of an integrated circuit, consisting of many overlay processing steps. It is envisioned that a map of an integrated circuit can be constructed in which the image is a complex number (amplitude and phase) that represents the sum of all layered regions. At any point on the circuit the image information therefore contains the expected complex reflection coefficient, computed from known material properties (density, velocity, and layer thickness) occurring locally. A stable microscope, on the other hand, yields a two-dimensional description (map) of the actual total complex reflection coefficient of the integrated circuit being diagnosed. If, for example, an error in metallization thickness has been inadvertently made in the fabrication process, this error would be, in principle, readily detectable when the actual and computed maps are superimposed.

The following general and specific observations can be made at this time as a result of experience gained operating the scanning acoustic microscope:

(1) The instrument is easy to operate, and a new specimen can be examined in a matter of a few minutes. Operation is more comparable to that of an optical microscope than to that of a scanning electron microscope. The indications are that, independent of whether unique observations can al-

[†]Work performed at Microwave Laboratory, Stanford University, under NBS Contract No. 5-35899. NBS contact for additional information: R. I. Scace.

[§]See disclaimer, p. vi.

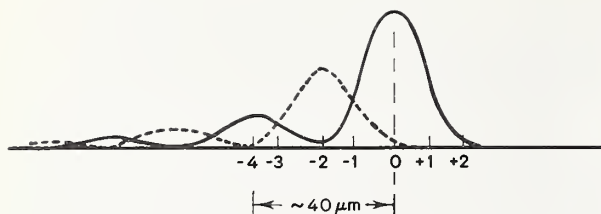
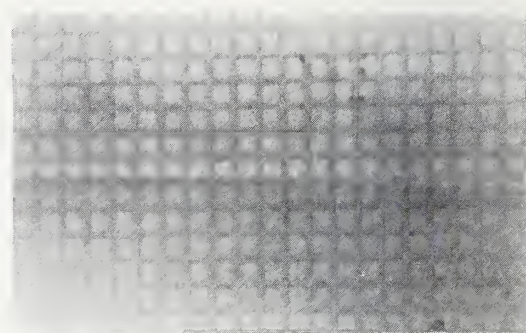
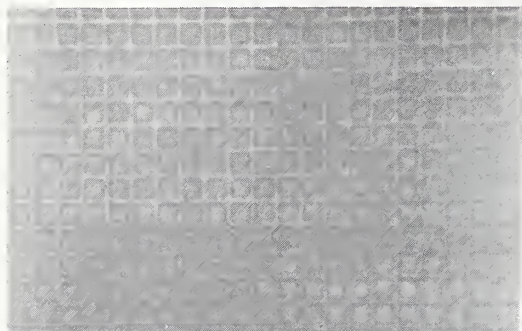


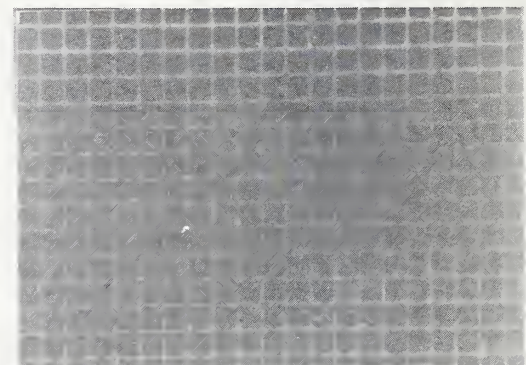
Figure 32. Variations in intensity of reflected pulsed acoustic signal as the lens-to-specimen spacing is changed. (When surface contrast exists, the reflected signal intensity varies over the surface; the dashed curve depicts the intensity variations (with spacing) of a region of opposite contrast to that of the solid curve. The lens-to-specimen spacing increases to the right.)



a. Position 0; focal point of lens at specimen surface; maximum signal obtained.



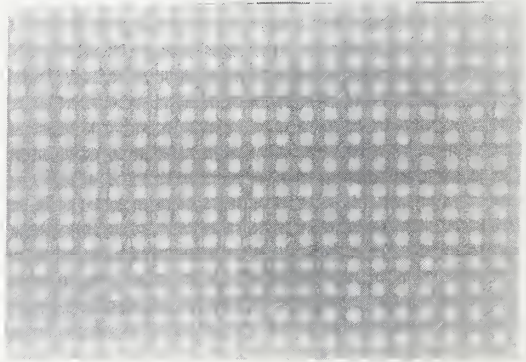
b. Position -1.



c. Position -2; note contrast inversion and increased sharpness of image.



d. Position -3.



e. Position -4; focal point of lens inside silicon; contrast same as in position 0.

Figure 33. Scanning acoustic micrographs of a 300-nm thick gold film grid pattern on silicon at various lens-to-specimen distances. (The elements are 2.5 μm wide on 25- μm centers.)

REFLECTED
INTENSITY 69% 99%

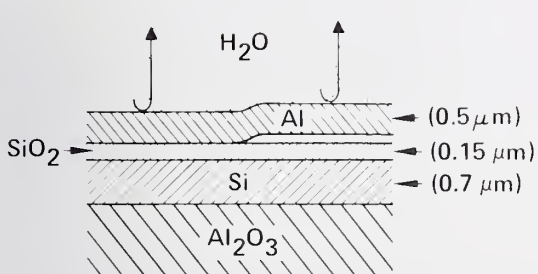


Figure 34. Effect of sub-surface void on intensity of acoustic signal reflected from an aluminum film on silicon dioxide.

ways be made, the instrument is suitable for in-line operation in a processing or circuit manufacturing line. Its simple controls and lack of a vacuum system render it more convenient to operate and maintain than a scanning electron microscope or an ion implantation system.

(2) The instrument is superior to the scanning electron microscope for nondestructive examination of insulating substrates or integrated circuits with (a) isolated regions or (b) large areas of insulating material, for example SOS integrated circuits, because charge does not accumulate on the surface.

(3) Scanning acoustic images appear to show edges (especially shallow steps) in materials and material differences better than images from either optical or scanning electron microscopes.

(4) The instrument has been shown to be capable of differentiating the various levels of processing in an integrated circuit (in a series of micrographs) through the simple operation of making small changes in the lens-to-specimen spacing.

(5) The instrument has been demonstrated to exhibit better-than-expected resolution capability.

The scanning acoustic microscope has also been successfully utilized to view gallium arsenide field-effect and transferred-electron devices, aluminum fuse links, and clad and unclad optical fibers. It appears to offer interesting possibilities for examining these structures in addition to conventional and SOS integrated circuits.

(R. G. Wilson[#] and R. D. Weglein[#])

9.2. Thermal Properties of Transistors[#]

The predictions of a physical model which has been proposed to explain the relationship between thermal instability and second breakdown [72] were confirmed experimentally. As shown in figure 35, there are two intersecting loci in the collector current (I_C), collector emitter voltage (V_{CE}) plane that define limits on the operation of forward-biased power transistors. One locus defines the limit of thermal instability and the other the limit of second breakdown. For currents greater than I^* , stable hot spots exist in the region between the two limits. For currents below I^* , the two limits nearly coincide, but thermal instability was found always to precede second breakdown.

Based upon the premise that the extremely high junction temperatures reached in the stable hot-spot region (usually greater than 200°C, often greater than 300°C) make operation in that region unsafe, it is proposed that the limit of thermal instability should be used as the safe-operating-area (SOA) limit for power transistors. A measurement method to determine the locus of thermal instability quickly and accurately and a non-destructive test for second breakdown have been developed.

The model predicts that thermal instability will occur when the temperature difference between the device chip and the outside case reaches some critical value. When an instability occurs, the current begins to constrict to a smaller and smaller area of the device. For values of I_C greater than I^* , the current stabilizes in some small finite area, but for values of I_C less than I^* , the current continues to constrict until second breakdown occurs.

Experiments have been performed to estimate how rapidly the current constricts and to determine how closely in time the measured increase in junction temperature coincides with the constriction. The estimates of the time variation of the current-carrying area

[#]Work performed at Hughes Research Laboratories under NBS Contract No. 35898. NBS contact for additional information: R. I. Scace.

[#]Funded through the NBS Electronic Technology Program.

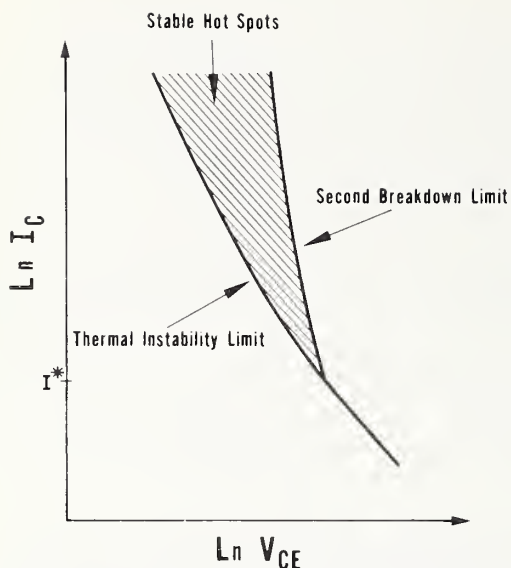
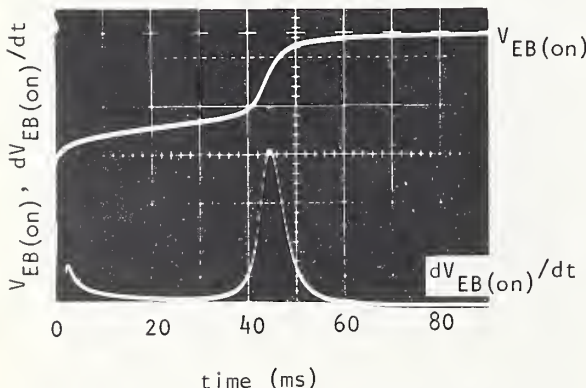


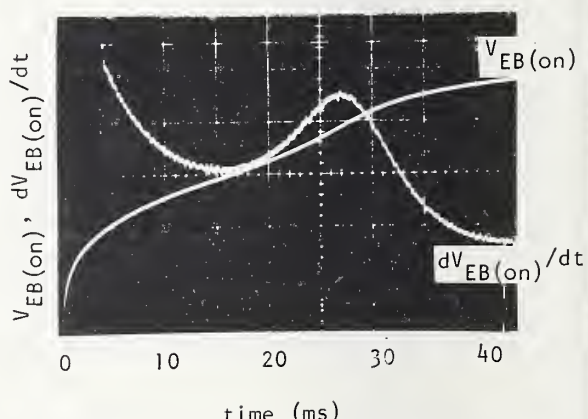
Figure 35. A schematic representation of the thermal instability and second breakdown limits of safe power transistor operation in the forward-biased region. (Below I^* , the two limits nearly coincide, but second breakdown always occurs after the onset of thermal instability.)

were made using the cooling-curve technique previously described [73]. Although this technique is strictly applicable only for cooling from steady-state conditions, the slight errors introduced into the calculated area by transient heating effects do not affect the validity of the observations reported here. The temperature was measured using a technique analogous to the standard method for measuring steady-state thermal resistance [74].

In each instance, it was observed that the current-carrying area begins to decrease before any significant change in heating rate is noticed, and that the rate of heating continues to be quite high even after the current has effectively stabilized to a small area. The characteristic shape of the rate of temperature increase is exploited in the technique developed to detect the onset of thermal instability. The on-state, emitter-base voltage, $V_{EB(on)}$, is used as the temperature monitor. Frequently, the change in $V_{EB(on)}$ when instability occurs is very small; to permit easy observation of the change in these cases, the time derivative of $V_{EB(on)}$ is monitored. Curves of $V_{EB(on)}$ and its time derivative are illustrated for two actual cases in figure 36. In the case illustrated in figure 36b, the onset of instability is difficult to discern in the $V_{EB(on)}$ curve, but it can be seen clearly in the derivative curve.



a. Onset of instability clearly evident in both curves.



b. Onset of instability barely evident in $V_{EB(on)}$ curve.

Figure 36. Curves of emitter-base voltage and its time derivative as a function of time following removal of power. (In these curves, the emitter-base voltage is negative and decreases in magnitude as time increases.)

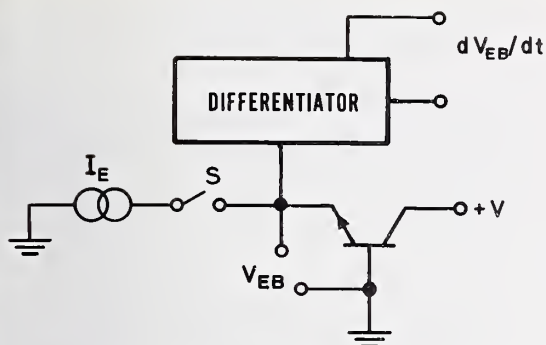


Figure 37. Simplified schematic of circuit for measuring time derivative of emitter-base voltage.

A schematic of the circuit for this measurement is shown in figure 37. The circuit is very similar to that used for making thermal resistance measurements [75]. The differentiator uses an operational amplifier as its active element. The pulse applied to the transistor under test is typically varied from 1 to 150 ms for measurements. It was established that the limits determined for pulses of 100 ms or longer were identical; thus, as far as thermal instability is concerned, 100-ms pulses are the equivalent of dc power.

The reason that pulses of 100 ms or longer are equivalent to dc is that the instability is related to the temperature difference between the case and the junction. For pulses longer than 100 ms or so, the base begins to heat, but the temperature difference between it and the junction does not increase significantly. Therefore, to generate even the dc SOA using the onset of thermal instability as the limit, no heat sinking would be required, and only pulses of 100 ms or shorter are required.

Since thermal instability always precedes second breakdown, this circuit can be used to develop the region of the curve for values of I_C less than I^* where the limit is governed by the onset of second breakdown. By triggering a turn-off circuit on the rising slope of the derivative curve, the device can be

turned off before damage from second breakdown can occur [75].

(D. L. Blackburn and S. Rubin)

9.3. Integrated Circuit Die-Attachment Evaluation

Work has resumed on the investigation of methods for using the temperature response of a substrate diode for determining the integrity of the die attachment of integrated circuits. For the first stage of this work, integrated circuit chips, nominally 0.050 in. (1.25 mm) square, were obtained. These chips are transistor arrays normally used for display drivers. By means of eutectic bonds one group of chips was attached to headers that each had a 0.038-in. (1.0-mm) diameter void ultrasonically machined into the surface [76]. Another group was bonded to headers with a 0.025-in. (0.6-mm) void, and a third group was bonded with no voids. The void area, expressed as a percentage of the total bonded area, was 45 percent for the large void and 20 percent for the small void.

Initial temperature measurements were made by applying a square wave to the device under test. For one-half of the cycle the transistors in the circuit were dissipating 1 W of power, and for the other half, the transistors were off and the substrate diode was forward biased so that the voltage drop across this junction could be measured. A precision rectifier circuit was used to measure the average dc voltage developed across the substrate diode during the forward-biased portion of the cycle. A repetition rate of 1 kHz was found not to allow much change in the temperature between the heating and measuring parts of the cycle. The results obtained to date have shown that the change in temperature produced in the chips bonded to the headers with the large void is 5 to 10 percent greater than that produced in the chips bonded to headers with no intentional void. This result suggests that a more sensitive technique would be desirable. New pulse heating and time delay measuring techniques are being developed in an attempt to find a more sensitive method.

(D. W. Berning and D. L. Blackburn)

10. REFERENCES

1. Standard Method for Measuring Resistivity of Silicon Slices with a Collinear Four-Probe Array, ASTM Designation F 84, *Annual Book of ASTM Standards*, Part 43 (November 1977).
2. Bullis, W. M., Brewer, F. H., Kolstad, C. D., and Swartzendruber, L. J., Temperature Coefficient of Resistivity of Silicon and Germanium near Room Temperature, *Solid-State Electronics* 11, 639-646 (1968).
3. Valdes, L. B., Resistivity Measurements on Germanium for Transistors, *Proc. IRE* 42, 420-427 (1954).
4. Swartzendruber, L. J., Correction Factor Tables for Four-Point Probe Resistivity Measurements on Thin Circular Semiconductor Samples, NBS Tech. Note 199 (April 15, 1964) AD 683 408.
5. Smits, F. M., Measurement of Sheet Resistivities with the Four-Point Probe, *Bell System Tech. J.* 37, 711-718 (1958).
6. Keenan, W. A., Schumann, P. A., Tong, A. H., and Phillips, R. P., A Model for the Metal-Semiconductor Contact in the Spreading Resistance Probe, *Ohmic Contacts to Semiconductors*, B. Schwarz, Ed., pp. 263-273 (Electrochemical Society, Princeton, N.J., 1969).
7. Kramer, P., and van Ruyven, L. J., The Influence of Temperature on Spreading Resistance Measurement, *Solid-State Electronics* 15, 757-766 (1972).
8. Ehrstein, J. R., Effect of Specimen Preparation on the Calibration and Interpretation of Spreading Resistance Measurements, *Semiconductor Silicon/1977*, H. R. Huff and E. Sirtl, Eds, pp. 377-386 (Electrochemical Society, Princeton, N.J., 1977).
9. Dickey, D. H., and Ehrstein, J. R., *Semiconductor Measurement Technology: Spreading Resistance Analysis for Silicon Layers with Nonuniform Resistivity*, NBS Special Publication 400-48 (in preparation).
10. Donovan, R. P., and Evans, R. A., Incremental Sheet Resistance Technique for Determining Diffusion Profiles, *Silicon Device Processing*, C. P. Marsden, Ed., NBS Special Publication 337, pp. 123-133 (November 1970).
11. Dickey, D. H., Two Point Probe Correction Factors, *Semiconductor Measurement Technology: Spreading Resistance Symposium*, J. R. Ehrstein, Ed, NBS Special Publication 400-10, pp. 45-50 (December 1974).
12. Schumann, P. A., and Gardner, E. E. Application of Multilayer Potential Distribution to Spreading Resistance Correction Factors, *J. Electrochem. Soc.* 116, 87-91 (1969).
13. Tong, A. H., Gorey, E. F., Schneider, C. P., Apparatus for the Measurement of Small Angles, *Rev. Sci. Instrum.* 43, 320-325 (1972).
14. Standard Method for Test for Sheet Resistance of Silicon Epitaxial Layers Using a Collinear Four-Probe Array, ASTM Designation F 374, *Annual Book of ASTM Standards*, Part 43 (November 1977).
15. Standard Method of Test for Thickness of Epitaxial or Diffused Layers in Silicon by the Angle Lapping and Staining Technique, ASTM Designation F 110, *Annual Book of ASTM Standards*, Part 43 (November 1977).
16. Carballoy Division, General Electric Co., Detroit, MI 48232.
17. K 75, Fidelitone, Inc., 207 N. Woodwork, Pallatine, IL 60067.
18. Fluorinert Brand Electronic Liquid, FC 43, Commercial Chemical Division, 3 M Co., 3 M Center, St. Paul, MN 55101.
19. Mattis, R. L., and Buehler, M. G., A New Method for Calculating Background Dopant Density from *p-n* Capacitance-Voltage Measurements, *J. Electrochem. Soc.* 124, 1918-1923 (1977).
20. Mattis, R. L., and Buehler, M. G., *Semiconductor Measurement Technology: A BASIC Program for Calculating Dopant Density Profiles from Capacitance-Voltage Data*, NBS Special Publication 400-11 (June 1975).
21. Wagner, S., Diffusion of Boron from Shallow Ion Implants in Silicon, *J. Electrochem. Soc.* 119, 1570-1576 (1972).

REFERENCES

22. Irvin, J. C., Resistivity of Bulk Silicon and of Diffused Layers in Silicon, *Bell System Tech. J.* 41, 387-410 (1962).
23. Barber, H. D., Effective Mass and Intrinsic Concentration in Silicon, *Solid-State Electronics* 10, 1039-1051 (1967).
24. Costato, M., and Reggiani, L., Ohmic Mobility of Holes in Silicon, *Nuovo Cimento* 68B, 64-70 (1970).
25. Brooks, H., Theory of the Electrical Properties of Germanium and Silicon, *Advances in Electronics and Electron Physics*, Vol. VII, L. Marton, Ed, pp. 85-182 (Academic Press, New York, 1955).
26. Sclar, N., Neutral Impurity Scattering in Semiconductors, *Phys. Rev.* 104, 1559-1568 (1956).
27. Li, S. S., *Semiconductor Measurement Technology*: The Dopant Density and Temperature Dependence of Electron Mobility and Resistivity in *n*-Type Silicon, NBS Special Publication 400-33 (March 1977); also, Li, S. S., and Thurber, W. R., The Dopant Density and Temperature Dependence of Electron Mobility and Resistivity in *n*-Type Silicon, *Solid-State Electronics* 20, 609-616 (1977).
28. Buehler, M. G., *Semiconductor Measurement Technology*: Microelectronic Test Pattern NBS-3 for Evaluating the Resistivity-Dopant Density Relationship of Silicon, NBS Special Publication 400-22 (June 1976).
29. Sclar, N., Resistivity and Deep Impurity Levels in Silicon at 300 K, *IEEE Trans. Electron Devices* ED-24, 709-712 (1977).
30. Sclar, N., Extrinsic Silicon Detectors for 3-5 and 8-14 μm , *Infrared Physics* 16, 435-448 (1976).
31. Levinstein, H., and Mudar, J., Infrared Detectors in Remote Sensing, *Proc. IEEE* 63, 6-14 (1975).
32. Miller, B., Mosaic Technique for IR Sensors Pushed, *Aviation Week and Space Technology* 104, No. 18, 71-83 (1976).
33. Anon., New Satellite Warning System Studies Begin, *Aviation Week and Space Technology* 104, No. 18, 26 (1976).
34. Hudson, R. D., Jr., and Hudson, J. W., The Military Applications of Remote Sensing by Infrared, *Proc. IEEE* 63, 104-128 (1975).
35. Marsh, O. J., Extrinsic Silicon Detector Array, Final Technical Report, Contract DAAK02-75-C-0079 (Hughes Research Laboratories, Malibu, California, April, 1976).
36. Buehler, M. G., and Phillips, W. E., A Study of the Gold Acceptor in a Silicon p^+ n Junction and an *n*-Type MOS Capacitor by Thermally Stimulated Current and Capacitance Measurements, *Solid-State Electronics* 19, 777-788 (1976).
37. Buehler, M. G., Impurity Centers in *p-n* Junctions Determined from Shifts in the Thermally Stimulated Current and Capacitance Response with Heating Rate, *Solid-State Electronics* 15, 69-79 (1972).
38. Sah, C. T., Forbes, L., Rosier, L. L., Tasch, A. F., Jr., and Tole, A. B., Thermal Emission Rates of Carriers at Gold Centers in Silicon, *Appl. Phys. Letters* 15, 145-148 (1969).
39. Goodman, A. M., *Semiconductor Measurement Technology*: Suppression of Premature Dielectric Breakdown for High-Voltage Capacitance Measurements, NBS Special Publication 400-37 (July 1977).
40. Goodman, A. M., *Semiconductor Measurement Technology*: A 25-kV Bias-Isolation Unit for 1-MHz Capacitance and Conductance Measurements, NBS Special Publication 400-40 (September 1977).
41. Kuczer, P., Hook, H. O., and Goodman, A. M., *Semiconductor Measurement Technology*: A Versatile High-Voltage Bias Supply for Extended Range MIS C(V) and G(V) Measurements, NBS Special Publication 400-41 (December 1977).
42. Goodman, A. M., *Semiconductor Measurement Technology*: The Safe Operation of Capacitance Meters Using High Applied Bias Voltage, NBS Special Publication 400-34 (December 1976).
43. Kokkas, A. G., Silicon/Sapphire Interface Radiation Study, RAD-C-TR-77-138 (April 5, 1977).
44. Kant, A., Cali, J. P., and Thompson, H. D., Determination of Impurities in Sili-

REFERENCES

- con by Neutron Activation Analysis, *Anal. Chem.* 28, 1867-1871 (1956).
45. Johannessen, J. S., Spicer, W. E., and Strausser, Y. E., An Auger Analysis of the SiO₂-Si Interface, *J. Appl. Phys.* 47, 3028-3037 (1976).
46. Kuhn, M., A Quasi-Static Technique for MOS C-V and Surface State Measurements, *Solid-State Electronics* 13, 873-885 (1970).
47. Grunthaner, F. J., and Lewis, B. F., Measurement of Energy Level References in X-ray Photoelectron Spectroscopy, *JPL New Technology Transmittal* 3457 (February 1976).
48. Grunthaner, F. J., and Maserjian, J., Sodium Ions at Defect Sites at SiO₂/Si Interfaces as Determined by X-ray Photoelectron Spectroscopy, *13th Annual Proceedings, Reliability Physics 1975*, Las Vegas, Nevada, April 1-3, 1975, pp. 15-25.
49. Grunthaner, F. J., Lewis, B. F., and Maserjian, J., Effect of Residual Organic Contamination on MOS Devices at SiO₂/Si Interfaces, Presented at IEEE Nonvolatile Semiconductor Memory Workshop, Vail, Colorado, August 1976. (Unpublished)
50. Grunthaner, F. J., Klein, J., and Barton, J. J., Resolution Enhancement, Deconvolution and Noise Removal in X-ray Photoelectron Spectroscopy (XPS) (in preparation).
51. Heinen, K. G., and Larrabee, G. B., Analysis of Silicon by Conventional Carrier Separations and by Computer Reduction of Gamma Spectra, *Anal. Chem.* 38, 1853-1857 (1966); also, Larrabee, G. B., and Carlson, H. G., Activation Analysis in Silicon Device Processing, *Silicon Device Processing*, C. P. Marsden, Ed, NBS Special Publication 337, pp. 375-383 (November 1970).
52. Carpenter, B. S., Determination of Trace Concentration of Boron and Uranium in Glass by the Nuclear Track Technique, *Anal. Chem.* 44, 600-602 (1972).
53. Buehler, M. G., and Thurber, W. R., A Planar Four-Probe Test Structure for Measuring Bulk Resistivity, *IEEE Trans. Electron Devices* ED-23, 968-974 (1976).
54. La Chapelle, R., Composition for Polish-Crystalline Silicon and Germanium and Process, U.S. Patent 3,429,080, February 25, 1969.
55. Duffy, M. T., Zanzucchi, P. J., and Cullen, G. W., Method to Determine the Quality of Sapphire, Report No. 2, NBS-GCR-76-61 (September 1976). (Available from the National Technical Information Service, Springfield, VA 22161.)
56. Wilson, R. G., Dunlap, H. L., and Jamba, D. M., Angular Sensitivity of Controlled Implanted Doping Profiles, *Semiconductor Silicon/1977*, H. R. Huff and E. Sirtl, Eds, pp. 1023-1034 (Electrochemical Society, Princeton, New Jersey, 1977).
57. Lindhard, J., Influence of Crystal Lattice on Motion of Energetic Charged Particles, *Mat. Fys. Medd. Dan. Vid. Selsk.* 34, No. 14 (1965).
58. Andersen, J. U., Davies, J. A., Nielsen, K. O., and Andersen, S. L., An Experimental Study of the Orientation Dependence of (p,γ) Yields in Monocrystalline Aluminum, *Nucl. Instrum. Methods* 38, 210-215 (1965).
59. Reddi, V. G. K., and Sansbury, J. D., Channeling and Dechanneling of Ion-Implanted Phosphorus in Silicon, *J. Appl. Phys.* 44, 2951-2963 (1973).
60. Brice, D. K., Ion Implantation Depth Distributions: Energy Deposited in Atomic Processes and Ion Location, *Appl. Phys. Letters* 16, 103-106 (1970); also, Brice, D. K., Spatial Distributions of Ions Incident on a Solid Target as a Function of Instantaneous Energy, Sandia Laboratories Report SC-RR-71-0599 (1971).
61. Nyssonnen, D., Linewidth Measurement with an Optical Microscope: The Effect of Operating Conditions on the Image Profile, *Appl. Optics* 16, 2223-2230 (1977).
62. Standard Method for Measuring Hall Mobility and Hall Coefficient in Extrinsic Semiconductor Single Crystals, ASTM Designation F 76, *Annual Book of ASTM Standards*, Part 43 (November 1977).
63. van der Pauw, L. S., A Method of Measuring the Resistivity and Hall Coef-

REFERENCES

- ficients on Lamella of Arbitrary Shape, *Philips Res. Rep.* 13, 1-9 (1958).
64. David, J. M., and Buehler, M. G., A Numerical Analysis of Various Cross Sheet Resistor Test Structures, *Solid-State Electronics* 20, 539-543 (1977).
65. Penney, W. M., and Lau, L., Eds, *MOS Integrated Circuits*, pp. 113-116 (van Nostrand, Reinhold Company, New York, 1972).
66. Schafft, H. A., Ed, *Semiconductor Measurement Technology*: ARPA/NBS Workshop II. Hermeticity Testing for Integrated Circuits, NBS Special Publication 400-9, p. 9 (December 1974).
67. Manufactured by Thunder Scientific Corporation, Albuquerque, New Mexico. (See disclaimer, p. vi.)
68. Hasegawa, S., and Little, J. W., The NBS Two-Pressure Humidity Generator, Mark 2, *J. Res. Nat. Bur. Stand.* 81A, 81-88 (1977).
69. Quate, C. F., A Scanning Acoustic Microscope, *Semiconductor Silicon/1977*, H. R. Huff and E. Sirtl, Eds, pp. 422-430 (Electrochemical Society, Princeton, New Jersey, 1977).
70. Wilson, R. G., Weglein, R. D., and Bonnell, D. M., Scanning Acoustic Microscopy for Integrated Circuit Diagnostics, *Semiconductor Silicon/1977*, H. R. Huff and E. Sirtl, Eds, pp. 431-440 (Electrochemical Society, Princeton, New Jersey, 1977).
71. Weglein, R. D., Wilson, R. G., and Bonnell, D. M., Scanning Acoustic Microscopy - Application to Fault Detection, *15th Annual Proceedings, Reliability Physics 1977*, Las Vegas, Nevada, April 12-14, 1977, pp. 37-43.
72. Hower, P. L., Blackburn, D. L., Oettinger, F. F., and Rubin, S., Stable Hot Spots and Second Breakdown in Power Transistors, *PESC '76 Record*, IEEE Power Electronics Specialists Conference 1976, Cleveland, Ohio, June 8-10, 1976, pp. 234-246.
73. Blackburn, D. L., and Oettinger, F. F., Transient Thermal Response Measurements of Power Transistors, *PESC '74 Record*, IEEE Power Electronics Specialists Conference, Murray Hill, New Jersey, June 10-12, 1974, pp. 140-148.
74. Thermal Resistance Measurements of Conduction Cooled Power Transistors, EIA Recommended Standard RS-313-B (Revision of RS-313-A), October 1975.
75. Rubin, S., and Blackburn, D. L., A Test Unit for the Nondestructive Determination of the Forward-Biased Safe-Operating-Area Limits for Power Transistors, *Conference Record*, IEEE IAS Annual Meeting, Los Angeles, California, October 3-6, 1977, pp. 666-673.
76. Oettinger, F. F., and Gladhill, R. L., Thermal Response Measurements for Semiconductor Device Die Attachment Evaluation, *Technical Digest, 1973 Int. Electron Devices Meeting*, Washington, D. C., December 3-5, 1973, pp. 47-50.

APPENDIX A

SEMICONDUCTOR TECHNOLOGY PROGRAM STAFF

(on September 30, 1976)

Significant changes in assigned organizational units and telephone numbers have occurred between the end of the reporting period and the issue date of this report. Call the Electron Devices Division, (301) 921-3786, for current information.

Electronic Technology Division

(301) 921-3357

J. C. French, Chief
Miss B. S. Hope*
J. F. Mayo-Wells

Dr. W. M. Bullis, Asst. Chief for
Semiconductor Technology

F. F. Oettinger, Acting Asst. Chief
for Operations

Mrs. M. L. Stream*

R. L. Raybold

Mrs. E. J. Walters*†

Mrs. T. J. Talbott

Mrs. E. Y. Trager*

Semiconductor Characterization Section

(301) 921-3625

F. H. Brewer

Dr. J. R. Ehrstein

Mrs. B. A. Oravec*†

Dr. W. M. Bullis, Chief

Dr. K. F. Galloway

Miss D. R. Ricks

Mrs. F. C. Hoewing*

W. J. Keery

R. I. Scace

Mrs. C. A. Cannon

Dr. R. D. Larrabee

H. A. Schafft

Mrs. E. C. Cohen†

Mrs. K. O. Leedy

L. R. Williams

Dr. S. Mayo

Semiconductor Processing Section

(301) 921-3541

Dr. M. G. Buehler, Chief

Dr. R. Y. Koyama

D. A. Maxwell

R. L. Frisch

J. Krawczyk

Dr. W. E. Phillips

Mrs. A. D. Glover*

T. F. Leedy

Dr. T. J. Russell

S. D. Grant§

Dr. S. S. Li

Dr. D. E. Sawyer

Miss D. L. Hines*

Y. M. Liu

W. R. Thurber

R. L. Mattis

Electron Devices Section

(301) 921-3621

Dr. J. H. Albers

Mrs. K. E. Dodson*

Dr. D. B. Novotny

D. W. Berning

H. E. Dyson

F. F. Oettinger, Chief

D. L. Blackburn

G. G. Harman

G. J. Rogers

G. W. Burdette†

H. K. Kessler

S. Rubin

W. A. Cullins

M. D. Nelligan†

S. Ruthberg

* Secretary

† Part Time

§ Summer

APPENDIX B

SEMICONDUCTOR TECHNOLOGY PROGRAM PUBLICATIONS

B.1. Prior Reports

A review of the early work leading to this Program is given in Bullis, W. M., Measurement Methods for the Semiconductor Device Industry — A Review of NBS Activity, NBS Tech. Note 511 (December 1969).

Progress reports covering the period July 1, 1968, through June 30, 1973, were published as NBS Technical Notes with the title, Methods of Measurement for Semiconductor Materials, Process Control, and Devices:

Quarter Ending	NBS Tech. Note	Date Issued	NTIS Accession No.
September 30, 1968	472	December 1968	AD 681330
December 31, 1968	475	February 1969	AD 683808
March 31, 1969	488	July 1969	AD 692232
June 30, 1969	495	September 1969	AD 695820
September 30, 1969	520	March 1970	AD 702833
December 31, 1969	527	May 1970	AD 710906
March 31, 1970	555	September 1970	AD 718534
June 30, 1970	560	November 1970	AD 719976
September 30, 1970	571	April 1971	AD 723671
December 31, 1970	592	August 1971	AD 728611
March 31, 1971	598	October 1971	AD 732553
June 30, 1971	702	November 1971	AD 734427
September 30, 1971	717	April 1972	AD 740674
December 31, 1971	727	June 1972	AD 744946
March 31, 1972	733	September 1972	AD 748640
June 30, 1972	743	December 1972	AD 753642
September 30, 1972	754	March 1973	AD 757244
December 31, 1972	773	May 1973	AD 762840
March 31, 1973	788	August 1973	AD 766918
June 30, 1973	806	November 1973	AD 771018

After July 1, 1973, progress reports were issued in the NBS Special Publication 400 sub-series with the title, Semiconductor Measurement Technology:

Quarter Ending	NBS Spec. Publ.	Date Issued	NTIS Accession No.
September 30, 1973	400-1	March 1974	AD 775919
December 31, 1973	400-4	November 1974	COM 74-51222
March 31, 1974	400-8	February 1975	AD/A 005669
June 30, 1974	400-12	May 1975	AD/A 011121
September 30, 1974	400-17	November 1975	AD/A 017523
December 31, 1974	400-19	April 1976	PB 251844
March 31, 1975	400-25	October 1976	PB 258555
June 30, 1975	400-29	April 1977	AD/A 040011
September 30, 1975			
December 31, 1975			
March 31, 1976			
June 30, 1976			

B.2. Current Publications

As various phases of the work are completed, publications are prepared to summarize the results or to describe the work in greater detail. Publications of this kind which have appeared between February and September 1977 are listed below:

Jerde, J. M., Hartman, A. W., Nyssonen, D., Rosberry, F. W., Swing, R. E., Swyt, D. A., and Young, R. D., Accurate Linewidth Measurements at the National Bureau of Standards, *Proc. Microelectronics Seminar - Interface '76*, Monterey, California, October 3-5, 1976, pp. 51-59.

Leedy, K. O., A Bibliography on the Electron Beam Induced Current Analysis of Semiconductor Devices, *Solid State Technology* 20, (2), 45-48 (February 1977).

Sawyer, D. E., and Berning, D. W., *Semiconductor Measurement Technology: A Laser Scanner for Semiconductor Devices*, NBS Special Publication 400-24 (February 1977).

Buehler, M. G., and Sawyer, D. E., Microelectronic Test Patterns Aid Production of Custom ICs, *Circuits Manufacturing* 17 (2), 46-56 (February 1977).

French, J. C., The Measurement Challenge in Electronic Technology, *Dimensions/NBS* 61 (2), 12-15 (February 1977).

Li, S. S., and Thurber, W. R., *Semiconductor Measurement Technology: The Dopant Density and Temperature Dependence of Electron Mobility and Resistivity in n-Type Silicon*, NBS Special Publication 400-33 (March 1977).

Bullis, W. M., Ed, *Semiconductor Measurement Technology, Progress Report, January 1 to June 30, 1976*, NBS Special Publication 400-29 (April 1977).

Devaney, J. R., Leedy, K. O., and Keery, W. J., *Semiconductor Measurement Technology: Notes on SEM Examination of Microelectronic Devices*, NBS Special Publication 400-35 (April 1977).

Buehler, M. G., and Thurber, W. R., Measurement of the Resistivity of a Thin Square Sample with a Square Four-Probe Array, *Solid-State Electronics* 20, 403-406 (May 1977).

Blackburn, D. L., Koyama, R. Y., Oettinger, F. F., and Rogers, G. J., Measurement Techniques for High Power Semiconductor Materials and Devices: Annual Report, January 1 to December 31, 1976, NBSIR 77-1249 (May 1977). [Also published as ERDA Report CONS/3800-2 (May 1977).]

Mayo, S., and Evans, W. H., Development of Sodium Contamination in Semiconductor Oxidation Atmospheres at 1000°C, *J. Electrochem. Soc.* 124, 780-785 (May 1977).

Bullis, W. M., and Vieweg-Gutberlet, F. G., Current Trends in Silicon Characterization Techniques, *Semiconductor Silicon/1977*, H. R. Huff and L. Sirtl, Eds, pp. 360-366 (Electrochemical Society, Princeton, New Jersey, May 1977).

Ehrstein, J. R., Effect of Specimen Preparation on the Calibration and Interpretation of Spreading Resistance Measurements, *Semiconductor Silicon/1977*, H. R. Huff and L. Sirtl, Eds, pp. 377-386 (Electrochemical Society, Princeton, New Jersey, May 1977).

Jerde, J. M., Hartman, A. W., Nyssonen, D., Swing, R. E., Young, R. D., and Keery, W. J., Comparison of Linewidth Measurements on an SEM/Interferometer System and an Optical Linewidth-Measuring Microscope, SPIE, Vol. 100, *Semiconductor Microlithography II*, 37-45 (June 1977).

Leedy, K. O., Measurement of Transistor Collector-Emitter Saturation Voltage, NBSIR 77-1231 (June 1977).

Ruthberg, S., Hermetic Test Procedures and Standards for Semiconductor Electronics, *Nondestructive Testing Standards - A Review*, ASTM STP 624, H. Berger, Ed, pp. 246-259 (American Society for Testing and Materials, Philadelphia, Pennsylvania, June 1977).

APPENDIX B

Ruthberg, S., Gas Infusion into Doubled Hermetic Enclosures, *IEEE Trans. Parts, Hybrids, and Packaging* PHP-13, 110-116 (June 1977).

Harman, G. G., The Use of Acoustic Emission in a Test for Beam-Lead, TAB, and Hybrid Chip Capacitor Bond Integrity, *IEEE Trans. Parts, Hybrids, and Packaging* PHP-13, 116-127 (June 1977).

Sawyer, D. E., Berning, D. W., and Lewis, D. C., Laser Scanning of Active Integrated Circuits and Discrete Semiconductor Devices, *Solid State Technology* 20 (6), 37-41 & 48 (June 1977).

David, J. M., and Buehler, M. G., A Numerical Analysis of Various Cross Sheet Resistor Test Structures, *Solid-State Electronics* 20, 539-543 (June 1977).

Nyyssonen, D., Optical Linewidth Measurements on Silicon and Iron-Oxide Photomasks, SPIE, Vol. 100, *Semiconductor Microlithography II*, 127-134 (June 1977).

Scire, F. E., New "Piezo-Flex" Micropositioning Stage Permits Smooth Control of Displacements in Microscope Systems, *Dimensions/NBS* 61 (7), 26 (July 1977).

Young, R. D., Length Calibrations in the Micrometer and Sub-Micrometer Range, *Ann. CIRP* 25, 245-250 (July 1977).

Li, S. S., and Thurber, W. R., The Dopant Density and Temperature Dependence of Electron Mobility and Resistivity in n-Type Silicon, *Solid-State Electronics* 20, 609-616 (July 1977).

Schafft, H. A., Ed, *Semiconductor Measurement Technology: Reliability Technology for Cardiac Pacemakers II - A Workshop Report*, NBS Special Publication 400-42 (August 1977).

Nyyssonen, D., Linewidth Measurement with an Optical Microscope: The Effect of Operating Conditions on the Image Profile, *Appl. Optics* 16, 2223-2230 (August 1977).

Swyt, D. A., and Rosberry, F. W., A Comparison of Some Optical Microscope Measurements of Photomask Linewidths, *Solid State Technology* 20 (8), 70-75 (August 1977).

Blackburn, D. L., *Semiconductor Measurement Technology: Safe Operating Area Limits for Power Transistors - Videotape Script*, NBS Special Publication 400-44 (September 1977).

B.3. Contractor Reports and Publications

Work carried on under contract to NBS is reported in both NBS publications and in the open literature as various phases are completed. Recent publications and reports of this kind are listed below:

Soulhoff, R. E., and Zatz, S., A Study of Leak Rates and Moisture Transport as Related to Reliability, *Proc. 1976 Internat. Microelectronics Symp.*, Vancouver, B. C., October 11-13, 1976, p. 337.

Goodman, A. M., Safe Operation of Capacitance Meters Using High Applied-Bias Voltage, *RCA Rev.* 37, 491-514 (December 1976).

Kern, W., and Comizzoli, R. B., New Methods for Detecting Structural Defects in Glass Passivation Films, *J. Vac. Sci. Tech.* 14, 32-39 (January/February 1977).

Kern, W., and Comizzoli, R. B., *Semiconductor Measurement Technology: Techniques for Measuring the Integrity of Passivation Overcoats on Integrated Circuits*, NBS Special Publication 400-31 (March 1977).

APPENDIX B

Dobrott, R. D., Keenan, J. A., and Larrabee, G. B., Ion Microprobe Analysis of Integrated Circuit Structures, *15th Annual Proceedings, Reliability Physics 1977*, Las Vegas, Nevada, April 12-14, 1977. pp. 54-60.

Weglein, R. D., Wilson, R. G., and Bonnell, D. M., Scanning Acoustic Microscopy — Application to Fault Detection, *15th Annual Proceedings, Reliability Physics 1977*, Las Vegas, Nevada, April 12-14, 1977, pp. 37-43.

Quate, C. F., A Scanning Acoustic Microscope, *Semiconductor Silicon/1977*, H. R. Huff and E. Sirtl, Eds, pp. 422-430 (Electrochemical Society, Princeton, New Jersey, May 1977).

Wilson, R. G., Weglein, R. D., and Bonnell, D. M., Scanning Acoustic Microscopy for Integrated Circuit Diagnostics, *Semiconductor Silicon/1977*, H. R. Huff and E. Sirtl, Eds, pp. 431-440 (Electrochemical Society, Princeton, New Jersey, May 1977).

Wilson, R. G., Dunlap, H. L., and Jamba, D. M., Angular Sensitivity of Controlled Implanted Doping Profiles, *Semiconductor Silicon/1977*, H. R. Huff and E. Sirtl, Eds, pp. 1023-1034 (Electrochemical Society, Princeton, New Jersey, May 1977).

Johannessen, J. S., Helms, C. R., Spicer, W. E., and Strausser, Y. E., Auger Depth Profiling of MNOS Structures by Ion Sputtering, *IEEE Trans. Electron Devices ED-24*, 547-551 (May 1977).

Goodman, A. M., *Semiconductor Measurement Technology: Suppression of Premature Dielectric Breakdown for High-Voltage Capacitance Measurements*, NBS Special Publication 400-37 (July 1977).

Jamba, D. M., *Semiconductor Measurement Technology: Some Aspects of Dose Measurement for Accurate Ion Implantation*, NBS Special Publication 400-39 (July 1977).

Goodman, A. M., and Weitzel, C. E., The Effect of Electron Beam Aluminization on the Si-Sapphire Interface, *Appl. Phys. Letters* 31, 114-117 (July 1977).

Comizzoli, R. B., Nondestructive, Reverse Decoration of Defects in IC Passivation Overcoats, *J. Electrochem. Soc.* 124, 1087-1095 (July 1977).

Helms, C. R., Garner, C. M., Miller, J., Lindau, I., Schwarz, S., and Spicer, W. E., Studies of Si/SiO₂ Interfaces by Auger Sputter Profiling and Photoelectron Spectroscopy Using Synchrotron Radiation, *Proc. 7th Intern. Vac. Congr. & 3rd Intern. Conf. Solid Surfaces*, Vienna, September 1977, pp. 2241-2243.

Goodman, A. M., *Semiconductor Measurement Technology: A 25-kV Bias-Isolation Unit for 1-MHz Capacitance and Conductance Measurements*, NBS Special Publication 400-40 (September 1977).

B.4. Videotapes

Color videotape cassette presentations on improvements in semiconductor measurement technology are being prepared for the purpose of more effectively disseminating the results of the work to the semiconductor industry. These videotapes are available for distribution on loan without charge on request to Mrs. E. C. Cohen, Room A327, Technology Building, National Bureau of Standards, Washington, D. C. 20234. Copies of these videotapes may be made and retained by requestors. As an added feature, arrangements can be made for the authors to be available for a telephone conference call to answer questions and provide more detailed information, following a prearranged showing of any of the videotapes.

The following videotapes are available for distribution:

1. Defects in PN Junctions and MOS Capacitors
Observed Using Thermally Stimulated Current and
Capacitance Measurements

M. G. Buehler

August 1974

APPENDIX B

2. Laser Scanning of Active Semiconductor Devices	D. E. Sawyer and D. W. Berning	October 1975
3. Safe Operating Area Limits for Power Transistors	D. L. Blackburn	September 1977

B.5. Availability of Publications and Videotapes

In most cases reprints of articles in technical journals may be obtained on request to the author. Current information regarding availability of all publications and videotapes issued by the Program is provided in the latest edition of NBS List of Publications No. 72 which can be obtained on request to Mrs. E. C. Cohen, Room A327, Technology Building, National Bureau of Standards, Washington, D. C. 20234.

APPENDIX C

SOLID-STATE TECHNOLOGY & FABRICATION SERVICES

Technical services in areas of competence are provided to other NBS activities and other government agencies as they are requested. Usually these are short-term, specialized services that cannot be obtained through normal commercial channels. Such services provided during this and the previous reporting period, which are listed below, indicate the kinds of technology available to the program.

C.1. Semiconductor Device Fabrication (T. F. Leedy and J. Krawczyk)

Silicon samples were prepared for the Naval Surface Weapons Center for use in studies of radio-frequency burnout.

MOS devices were prepared for the Harry Diamond Laboratories for use in studies of the optical stimulation of charge carriers.

Further special silicon samples were prepared for the NBS Mechanics Division for use in metal-vacuum-metal experiments designed to provide direct observation of tunneling phenomena between metals and to measure properties of Fermi surfaces. The fabrication of these samples included thermal and chemical vapor preparation of silicon oxide layers, chemical vapor deposition of polycrystalline silicon layers, evaporation of chromium pattern using photomask techniques, evaporation of aluminum and copper films, and use of preferential plasma etching, scribing, and mounting chips onto headers.

Oxide-coated silicon wafers were prepared for the NBS Polymers Division for studies of the attachment of lipid structures to well characterized surfaces in connection with surgical implantation.

C.2. Metal Evaporation (T. F. Leedy)

Special emulsion reticles were fabricated for the NBS Physical Chemistry Division for use in a photogrammetric apparatus.

C.3. Micromechanical Work (T. F. Leedy)

A special high-frequency, high-impedance, low-capacitance probe previously fabricated for the NBS Product Engineering Division was repaired at the request of that Division.

INDEX

- Auger electron spectroscopy (AES) 30-34
binding-energy measurements 34
boron density 18-19; 36-37
capacitance-voltage methods 18-19; 24-25
carbon concentration 34-35
channeling 40-41
chemical diagnostic methods 33-36
complex reflection coefficient 55-57
contrast inversion, scanning acoustic microscope 55-57
couplant, loose-particle detection 52-53
cross-bridge sheet resistor 45-46
cylindrical mirror analyzer (CMA) 30
defocus, optical microscope 42-44
defocus, scanning acoustic microscope 54-57
depth-profile measurements 10-17; 30-33
dew-point measurements 49-51
dragging-stylus probe 16-17

electrometer circuits 46-48
electron spectroscopy techniques 30-36
extrinsic silicon detectors 19-20

four-probe method 7

gold donor 20-22

hermeticity 49-51
hole emission probability 20-22
hole mobility 18-19

indium-doped silicon 19-20
integrated circuit die attachment 59
interface studies 31-35
ion implantation 40-41
ion microprobe mass analysis 26-30
ion-beam rastering 30
ion-scattering spectroscopy (ISS) 33
ion-stimulated Auger transitions 30-31
Irvin curve 18-19
isothermal capacitance transient response 20-22

KLL transitions 30-31

large-scale integration (LSI) 48
line-width measurements 42-44
local-slope algorithm 12-15; 17
loose-particle detection 52-53
low-temperature processing 23

mesa diode test structure 23-24
metal-insulator semiconductor (MIS) 24-25
metal-oxide semiconductor (MOS) capacitors 20-23; 37; 46-48
metal-oxide semiconductor (MOS) electrometer circuits 46-48

modular test structures 45-48
moisture infusion 49-51

neutron activation analysis 26-27
nuclear-track technique 36-37
numerical aperture, optical microscope 42-44

optical image profiles 42-44
optical microscope focus 42-44
optical test for surface quality 37-39
oxide hygrometer sensor 49-51

particle-impact noise detection (PIND) techniques 52-53
phosphorus density 26-30
photolithography 42-44
planar silicon test structure 46-48
power-grade silicon 22-24
process monitoring 23-24; 48
pulsed reflection mode, scanning acoustic microscope 54-57

resolution, scanning acoustic microscope 55-57

safe-operating-area (SOA) limit, transistor 57-59
sapphire substrates 37-39; see also silicon on sapphire
scanning acoustic microscopy 54-57
scanning low-energy electron probe (SLEEP) 33-34
second breakdown 57-59
secondary-ion mass spectroscopy (SIMS) 33
silicon on sapphire (SOS) 24-25; 27; 37-39; 48; 54
spreading resistance methods 7-17
sputtering rate 27
stable hot spots, transistor 57-59
surface preparation, silicon 7-10

test patterns 45-48
test structures 46-48
thermal properties of transistors 57-59
thermally controlled chuck 22-23
thermally stimulated current and capacitance 20-24
thyristor 23-24
transistor thermal instability 57-59
tungsten carbide spreading resistance probes 8-10
tungsten-osmium spreading resistance probes 8-10

van der Pauw structure 45-46

wafer prober, automatic 22-23
Wagner curve 37

X-level, silicon 20
x-ray photoelectron spectroscopy (XPS) 33-36



U.S. DEPT. OF COMM. BIBLIOGRAPHIC DATA SHEET		1. PUBLICATION OR REPORT NO. NBS Spec. Publ. 400-36	2. Gov't Accession No.	3. Recipient's Accession No.
TITLE AND SUBTITLE Semiconductor Measurement Technology: Progress Report July 1 to September 30, 1976		5. Publication Date July 1978		
		6. Performing Organization Code		
AUTHOR(S) W. Murray Bullis and J. Franklin Mayo-Wells, Editors		8. Performing Organ. Report No.		
PERFORMING ORGANIZATION NAME AND ADDRESS NATIONAL BUREAU OF STANDARDS DEPARTMENT OF COMMERCE WASHINGTON, D.C. 20234		10. Project/Task/Work Unit No.		
		11. Contract/Grant No. see item 15		
. Sponsoring Organization Name and Complete Address (Street, City, State, ZIP) NBS - Washington, D.C. 20234; SSPO - Washington, D.C. 20376; DNA - Washington, D.C. 20305; ARPA - 1400 Wilson Boulevard, Arlington, VA 22209; SAMSO - P.O. Box 92960, Worldway Postal Center, Los Angeles, CA 90009; ERDA - Washington, D.C. 20545		13. Type of Report & Period Covered Interim: July 1 to Sept. 30, 1976		
		14. Sponsoring Agency Code		
. SUPPLEMENTARY NOTES ARPA Order 2397, Program Code TD10; DNA IACRO 7T-812; SSPO Order N00164-76-MP-04511; MIPR FY76 167600366; ERDA Contract E(49-1)-3300, Mod. 3.				
. ABSTRACT (A 200-word or less factual summary of most significant information. If document includes a significant bibliography or literature survey, mention it here.) This progress report describes NBS activities directed toward the development of methods of measurement for semiconductor materials, process control, and devices. Both in-house and contract efforts are included. The emphasis is on silicon device technologies. Principal accomplishments during this reporting period included (1) completion of the systematic study of the effects of surface preparation and probe material on the empirical calibration between specimen resistivity and spreading resistance of n- and p-type silicon; (2) initial evaluation of the nuclear-track technique for quantitative determination of trace amounts of boron in silicon; (3) development of procedures for using an optical research microscope to make accurate measurements of the width of a clear line as narrow as 0.5 μm in a completely or nearly opaque background; (4) design of a compact cross-bridge test structure for electrical measurement of line width and sheet resistance in minimum line-width geometries; (5) completion of the initial phase of the study of the particle-impact noise detection test for screening devices for the presence of loose particles in the package; (6) demonstration of a greater-than-expected line resolution capability for the scanning acoustic microscope; and (7) development of a nondestructive technique to measure the onset of second breakdown in forward-biased, medium-power transistors. Also reported is other ongoing work on materials characterization by electrical and physical analysis methods, materials and procedures for wafer processing, photolithography, test patterns, and device inspection and test procedures. Supplementary data concerning staff, publications, and technical services are included as appendices.				
. KEY WORDS (six to twelve entries; alphabetical order; capitalize only the first letter of the first key word unless a proper name; separated by semicolons). Auger electron spectroscopy; capacitance-voltage methods, dew-point sensing; dragging-stylus probe; electrical properties; electronics; four-probe method; hermeticity; hole mobility; infrared reflectance; ion implantation; ion microprobe mass analysis; line-width measurements; nuclear-track technique; particle-impact noise detection; photolithography; photovoltaic method; p-n junction; power-device grade silicon; resistivity; resistivity variations; resistors, sheet; safe operating area, transistor; scanning acoustic microscope; second breakdown; semiconductor materials; semiconductor process control; silicon; silicon dioxide; silicon-on-sapphire; spreading resistance; test patterns; test structures; thermally stimulated current and capacitance; thermal properties, transistor; thermal response; thyristors; transistors, power; ultraviolet reflectance; x-ray photoelectron spectroscopy.				
8. AVAILABILITY <input checked="" type="checkbox"/> Unlimited		19. SECURITY CLASS (THIS REPORT) UNCLASSIFIED	21. NO. OF PAGES 78	
<input type="checkbox"/> For Official Distribution. Do Not Release to NTIS		20. SECURITY CLASS (THIS PAGE) UNCLASSIFIED	22. Price \$2.75	
<input checked="" type="checkbox"/> Order From Sup. of Doc., U.S. Government Printing Office Washington, D.C. 20402, SD Stock No. SN003-002-				
<input checked="" type="checkbox"/> Order From National Technical Information Service (NTIS) Springfield, Virginia 22151 (Microfiche only)				

NBS TECHNICAL PUBLICATIONS

PERIODICALS

JOURNAL OF RESEARCH—The Journal of Research of the National Bureau of Standards reports NBS research and development in those disciplines of the physical and engineering sciences in which the Bureau is active. These include physics, chemistry, engineering, mathematics, and computer sciences. Papers cover a broad range of subjects, with major emphasis on measurement methodology, and the basic technology underlying standardization. Also included from time to time are survey articles on topics closely related to the Bureau's technical and scientific programs. As a special service to subscribers each issue contains complete citations to all recent NBS publications in NBS and non-NBS media. Issued six times a year. Annual subscription: domestic \$17.00; foreign \$21.25. Single copy, \$3.00 domestic; \$3.75 foreign.

Note: The Journal was formerly published in two sections: Section A "Physics and Chemistry" and Section B "Mathematical Sciences."

DIMENSIONS/NBS

This monthly magazine is published to inform scientists, engineers, businessmen, industry, teachers, students, and consumers of the latest advances in science and technology, with primary emphasis on the work at NBS. The magazine highlights and reviews such issues as energy research, fire protection, building technology, metric conversion, pollution abatement, health and safety, and consumer product performance. In addition, it reports the results of Bureau programs in measurement standards and techniques, properties of matter and materials, engineering standards and services, instrumentation, and automatic data processing.

Annual subscription: Domestic, \$12.50; Foreign \$15.65.

NONPERIODICALS

Monographs—Major contributions to the technical literature on various subjects related to the Bureau's scientific and technical activities.

Handbooks—Recommended codes of engineering and industrial practice (including safety codes) developed in cooperation with interested industries, professional organizations, and regulatory bodies.

Special Publications—Include proceedings of conferences sponsored by NBS, NBS annual reports, and other special publications appropriate to this grouping such as wall charts, pocket cards, and bibliographies.

Applied Mathematics Series—Mathematical tables, manuals, and studies of special interest to physicists, engineers, chemists, biologists, mathematicians, computer programmers, and others engaged in scientific and technical work.

National Standard Reference Data Series—Provides quantitative data on the physical and chemical properties of materials, compiled from the world's literature and critically evaluated. Developed under a world-wide program coordinated by NBS. Program under authority of National Standard Data Act (Public Law 90-396).

NOTE: At present the principal publication outlet for these data is the Journal of Physical and Chemical Reference Data (JPCRD) published quarterly for NBS by the American Chemical Society (ACS) and the American Institute of Physics (AIP). Subscriptions, reprints, and supplements available from ACS, 1155 Sixteenth St. N.W., Wash., D.C. 20056.

Building Science Series—Disseminates technical information developed at the Bureau on building materials, components, systems, and whole structures. The series presents research results, test methods, and performance criteria related to the structural and environmental functions and the durability and safety characteristics of building elements and systems.

Technical Notes—Studies or reports which are complete in themselves but restrictive in their treatment of a subject. Analogous to monographs but not so comprehensive in scope or definitive in treatment of the subject area. Often serve as a vehicle for final reports of work performed at NBS under the sponsorship of other government agencies.

Voluntary Product Standards—Developed under procedures published by the Department of Commerce in Part 10, Title 15, of the Code of Federal Regulations. The purpose of the standards is to establish nationally recognized requirements for products, and to provide all concerned interests with a basis for common understanding of the characteristics of the products. NBS administers this program as a supplement to the activities of the private sector standardizing organizations.

Consumer Information Series—Practical information, based on NBS research and experience, covering areas of interest to the consumer. Easily understandable language and illustrations provide useful background knowledge for shopping in today's technological marketplace.

Order above NBS publications from: Superintendent of Documents, Government Printing Office, Washington, D.C. 20402.

Order following NBS publications—NBSIR's and FIPS from the National Technical Information Services, Springfield, Va. 22161.

Federal Information Processing Standards Publications (FIPS PUB)—Publications in this series collectively constitute the Federal Information Processing Standards Register. Register serves as the official source of information in the Federal Government regarding standards issued by NBS pursuant to the Federal Property and Administrative Services Act of 1949 as amended, Public Law 89-306 (79 Stat. 1127), and as implemented by Executive Order 11717 (38 FR 12315, dated May 11, 1973) and Part 6 of Title 15 CFR (Code of Federal Regulations).

NBS Interagency Reports (NBSIR)—A special series of interim or final reports on work performed by NBS for outside sponsors (both government and non-government). In general, initial distribution is handled by the sponsor; public distribution is by the National Technical Information Services (Springfield, Va. 22161) in paper copy or microfiche form.

BIBLIOGRAPHIC SUBSCRIPTION SERVICES

The following current-awareness and literature-survey bibliographies are issued periodically by the Bureau:

Cryogenic Data Center Current Awareness Service. A literature survey issued biweekly. Annual subscription: Domestic, \$25.00; Foreign, \$30.00.

Liquified Natural Gas. A literature survey issued quarterly. Annual subscription: \$20.00.

Superconducting Devices and Materials. A literature survey issued quarterly. Annual subscription: \$30.00. Send subscription orders and remittances for the preceding bibliographic services to National Bureau of Standards, Cryogenic Data Center (275.02) Boulder, Colorado 80302.

U.S. DEPARTMENT OF COMMERCE
National Bureau of Standards
Washington, D.C. 20234

OFFICIAL BUSINESS

Penalty for Private Use, \$300

POSTAGE AND FEES PAID
U.S. DEPARTMENT OF COMMERCE
COM-215



SPECIAL FOURTH-CLASS RATE
BOOK

1298







